# UNIVERSIDAD POLITÉCNICA DE MADRID

ESCUELA TÉCNICA SUPERIOR DE INGENIEROS INDUSTRIALES


# Development of novel HiPIMS processes for the deposition of DLC coatings with enhanced tribomechanical performance

# TESIS DOCTORAL


José Antonio Santiago Varela

Ingeniero Industrial por la Universidad Politécnica de Madrid


2020

**DEPARTAMENTO DE INGENIERÍA ENERGÉTICA**

ESCUELA TÉCNICA SUPERIOR DE INGENIEROS INDUSTRIALES

# Development of novel HiPIMS processes for the deposition of DLC coatings with enhanced tribomechanical performance

José Antonio Santiago Varela

Licenciado en Ingeniería Industrial por la Universidad Politécnica de Madrid

Directores de Tesis:

Dra. Raquel González Arrabal

Profesor del Departamento Ingeniería Energética

Universidad Politécnica de Madrid

Dr. Miguel A. Monclús Palazón

IMDEA Materiales

2020

Tribunal nombrado por el Magnífico y Excelentísimo Sr. Rector de la Universidad Politécnica de Madrid, el día ____ de _____ de 2020.

Presidente:

Secretario:

Vocal:

Vocal:

Vocal:

Suplente:

Suplente:

Realizado el acto de defensa y lectura de la Tesis el día ___ de _____ de 2020 en la Escuela Técnica Superior de Ingenieros Industriales.

CALIFICACIÓN:

EL PRESIDENTE LOS VOCALES

EL SECRETARIO

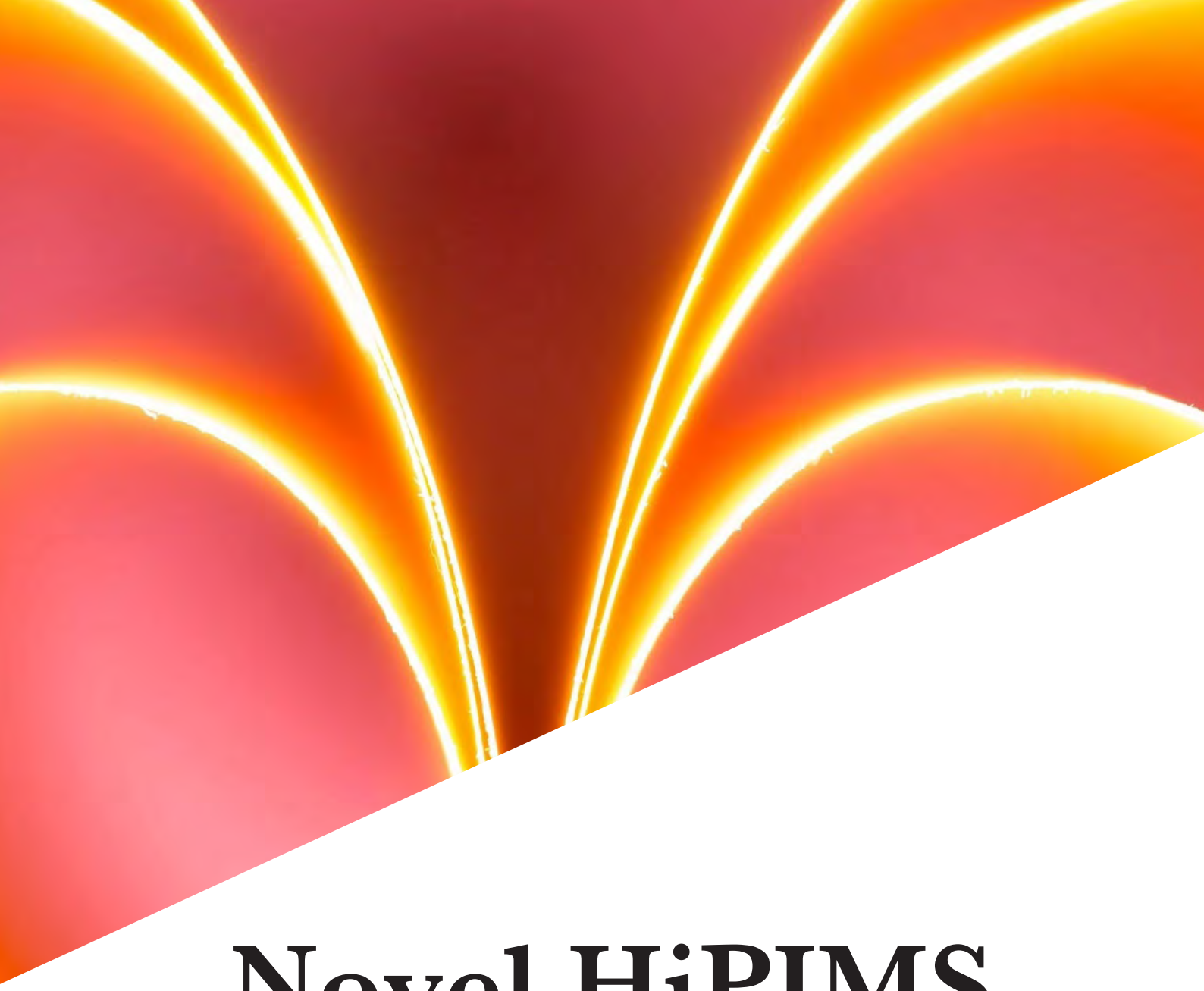

# Novel HiPIMS *processes for* DLC coatings

Development of novel **HiPIMS** processes for the deposition of **DLC coatings** with enhanced tribomechanical performance

*José Antonio Santiago Varela*

# *Acknowledgements*

I cannot pretend I am not tired after these years of thesis. But, at the end, my predominant feeling is one of gratitude. I have been given much and I have received a lot in return. I have studied all kind of diamonds and yet I could not hold a good one for me. I have traveled to exotic places, bohemian cities and human anthills. I have worked in antiquarian labs, garages, museums and in the most modern facilities. I have read papers thousands of times and found a new lesson every day. I have written, corrected, rewritten and recorrected until reaching the limit of my stubbornness, which still seems to be infinite. And above all, I have found amazing people, and that in itself has been an enormous priviledge and adventure.

I would like to express my gratitude to my supervisor Dra. Raquel González Arrabal because she gave me a first opportunity in research and that is something I will always thank. Her support has been priceless for me. I can't say enough about the cooperation of my other supervisor Dr. Miguel Monclús. He is extremely generous with me as he is with all people around him. There is no merit on admiring him: the challenge is to be at his level, to behave with people as he behaves with you.

This thesis would have not been possible without the mentorship of Dr. Ivan Fernandez. He has trained me on most of the aspects I know about PVD technology. And most importantly, he has given me the tools to fight for a work that now is also a passion. I extend my thanks to Ambiörn Wennberg and his invaluable help. His problem-solving skills and relentless support are a daily source of learning and inspiration. To all the team of Nano4Energy: Alvaro, Sandra and Diego, because it is a pleasure to work with them every day.

I extend my thanks to all the staff of IFN-GV and IMDEA Materials, especially to Dr. Antonio Rivera, Prof. JM Perlado and Dr Jon Molina for their guidance and insightful comments. Also, thanks to Dra. Cristina Rojas and Dr. Juan Carlos Sánchez López from ICMSe-CSIC because they have helped me a lot on DLC coatings characterization and I keep wonderful memories from my short stay in Sevilla. I could also enjoy another stay in CTU-Prague, where I had a fruitful time thanks to Dr. Tomas Vitu and Dr. Tomas Polcar. Particular gratitude is also extended to Dr. Tomas Kozak and Dr. Jiri Capek from West Bohemia University for their cooperation on mass spectroscopy measurements and their knowledge on HiPIMS. I cannot forget the groups of Universidad Mayor in Chile and Universidad Nacional in Cuyo (Argentina), with special thanks to Dr. Felipe Valencia, who provided me valuable numerical simulations for a deeper understanding on DLC coatings structure.

In these years, I also had the opportunity to learn about PVD technology from a more industrial perspective. In this regard, I would like to thank people from Gencoa, especially to Victor Bellido. To the people from Tekniker (especially to Oihane and Lutxi), because I always enjoy the cooperation on coatings and the funny moments in congresses. I would also like to thank Dr. Herbert Gabriel for the opportunity to develop DLC coatings in Bensheim. To all the people from PVT, for their support and help. Special thanks to Nico, the best of Kaiserslautern's fans and to Ilona and Dieter, because they are my German family.

To all the friends who have accompanied me over these years and who made the difficult moments more bearable. Special thanks to those who shared with me the experience of the PhD. To Birrabooks members, to IMDEA colleagues (especially to Eva and Cris), and special thanks to Emilio, Adrian, Pablos Diaz and Miguel. I have promised diamonds to some of them and the debt will be paid.

Ós meus pais e ás miñas irmás. Ó oído do amor sobranlle as palabras.

# Resumen

La utilización de recubrimientos convencionales de diamond-like carbon (DLC) para la protección de las superficies de herramientas y componentes en aplicaciones industriales de alta exigencia se encuentra actualmente restringida debido a limitaciones de cargas térmicas y de trabajo. Existen nuevas aplicaciones tribológicas, con temperaturas de trabajo que exceden los 300ºC, que requieren de recubrimientos con una mayor estabilidad térmica, una excelente adhesión y más dureza. Esta tesis explora el desarrollo de nuevos procesos con la tecnología high-power impulse magnetron sputtering (HiPIMS) para depositar recubrimientos de DLC con un comportamiento tribomecánico mejorado.

Inicialmente, un pretratamiento con iones metálicos de Ti o Cr ha sido optimizado mediante HiPIMS para mejorar la adhesión de recubrimientos de DLC sobre sustratos de acero rápido. El pretratmiento ha demostrado ser muy efectivo para eliminar contaminantes superficiales y generar una intercara gradual. La selección de iones de Cr sobre los de Ti aportó los mejores valores de adhesión debido a que se consiguió reducir el nivel de oxígeno en la intercara, asegurando de esta forma un óptimo contacto entre recubrimiento-sustrato y dotando a la estructura de un comportamiento más robusto que permitió prevenir en todo caso el fallo adhesivo.

Una de las principales aportaciones de la tesis fue el desarrollo de un método novedoso HiPIMS que incorpora pulsos positivos al final de la descarga convencional de HiPIMS. La aplicación de pulsos positivos permitió incrementar la energía de ionización tanto del carbono como del argón pulverizado. Las medidas de espectroscopía de masas mostraron que una mayor cantidad de iones de alta energía de carbono se generan, con energías proporcionales a la amplitud del pulso positivo. El bombardeo iónico producido por los pulsos positivos produjo recubrimientos de DLC más densos y duros.

Además, las propiedades mecánicas fueron optimizadas de acuerdo a la influencia de otros parámetros como el método de pulverización catódica, de la incorporación de hidrógeno, de la temperatura de depósito y del voltaje aplicado al sustrato. La síntesis de recubrimientos de DLC con técnicas de pulverización catódica por magnetrón pulsadas que incorporan pulsos positivos no solo resultó beneficiosa en el modo HiPIMS, sino que también lo fue en el modo DC-Pulsed. La grafitización de la estructura del carbono fue identificada como el principal factor que deteriora el recubrimiento durante la pulverización catódica. La caída en propiedades mecánicas debido a la grafitización se observó bajo un determinado rango de contenido en hidrógeno, temperatura de depósito o voltaje de sustrato. Las simulaciones numéricas de un proceso de nanoindentación también evidenciaron la importancia del contenido en $sp^3$ para limitar la plasticidad del material y de esta forma, mantener una alta dureza y módulo elástico.

En la búsqueda por recubrimientos de DLC con un comportamiento mejorado en aplicaciones tribomecánicas de alta temperatura, mediante un proceso de codepósito con HiPIMS y DC-pulsed se sintetizaron recubrimientos de DLC dopados con metales (Cr, Ti y W). Se observó que la aplicación de HiPIMS a bajas frecuencia incrementó significativamente la densidad de energía en la descarga de plasma del Cr debido a la interacción entre especies de Cr con C. El mayor bombardeo a altas energías producido cuando se trabajaba a bajas frecuencias permitió la incorporación de Cr en la estructura de DLC evitando la grafitización de la matriz de carbono. Los ensayos de nanoindentación a alta temperatura mostraron que las propiedades mecánicas a alta temperatura dependen fundamentalmente de la estructura $sp^3$-$sp^2$ de partida del carbono. Los recubrimientos DLC dopado con Cr depositados a baja frecuencia de HiPIMS permitieron preservar la estructura $sp^3$ del carbono y mostrar un comportamiento tribomecánico a alta temperatura mejorado con respecto a recubrimientos de DLC no dopados. Sin embargo, otros dopantes como el Ti o el W mostraron tendencia a desestabilizar la estructura $sp^3$ hacia $sp^2$. Dicha grafitización redujo la estabilidad térmica y la resistencia al desgaste de los recubrimientos.

Finalmente, es destacable que la novedosa tecnología de HiPIMS desarrollada en esta tesis se ha transferido a un sistema industrial, haciendo viable una nueva generación de recubrimientos de DLC para aplicaciones industriales de alta exigencia.

# Abstract

The use of traditional diamond-like carbon (DLC) coatings to protect tool and component surfaces for demanding application conditions in industry is currently restricted due to their limitations on work-loads and temperature. New tribological applications, where operating temperatures can reach over 300ºC, require coatings with high thermal stability, excellent adhesion and high hardness. This thesis deals with the development of novel high-power impulse magnetron sputtering (HiPIMS) processes for the deposition of DLC coatings with enhanced tribomechanical performance.

Initially, an optimized HiPIMS metal ion pretreatment, using either Ti or Cr, was used to improve the adhesion of DLC coatings on high speed steel substrates. The pretreatment was proven to be very effective at removing surface contaminants and providing a gradual interface. The selection of Cr over Ti ensured the best adhesion due to the reduction of the oxygen level at the interface thus ensuring an optimal coating-substrate contact and a more compliant structure, which prevents the delamination failure.

One of the main thesis' contributions was the development of a novel HiPIMS method that incorporates positive voltage pulses at the end of the conventional HiPIMS discharge. The application of positive pulses was observed to enhance the ionization of both the sputtered carbon and argon species. Mass spectroscopy measurements showed that a larger amount of high-energy $C^+$ ions are generated, with ion energies proportional to the amplitude of the overshoot voltage. The ion bombardment induced by the positive pulses led to denser and harder deposited DLC coatings.

In addition, mechanical properties were further optimized by investigating the influence of the sputtering method, hydrogen incorporation, deposition temperature and substrate bias voltage. The synthesis of DLC coatings with pulsed magnetron sputtering techniques that incorporate positive pulses not only resulted beneficial in HiPIMS but also in DC-Pulsed mode. The graphitization of the carbon structure was identified as the main factor deteriorating coatings' properties during sputtering deposition. The decay in mechanical properties due to graphitization was observed under selected ranges of hydrogen content, deposition temperature and substrate bias. Numerical simulations of a nanoindentation test showed that higher $sp^3$ contents constrained the plasticity, leading to higher hardness and elastic modulus.

In the search for DLC coatings with improved high temperature tribomechanical properties, metal-doped DLC coatings were synthesised in a codeposition process with HiPIMS (Cr, Ti and W deposition) and DC-pulsed technology (C deposition). The application of HiPIMS at low frequencies was observed to significantly enhance the energy density during the Cr plasma discharge due to the interaction of Cr with C species. The higher energy bombardment at low HiPIMS frequencies allowed the incorporation of Cr into the DLC structure avoiding the graphitization of the carbon structure. High temperature nanoindentation tests showed that the mechanical properties at high temperature mainly depend on the initial $sp^3$-$sp^2$ structure. Cr-doped DLC coatings deposited by low-frequency HiPIMS allowed preserving the $sp^3$ content, while providing enhanced tribomechanical properties at high temperature compared to undoped DLC. Other dopants such as Ti or W have an increased tendency to destabilize $sp^3$ into $sp^2$, thus reducing the thermal stability and wear resistance of the coatings.

Finally, it is worth highlighting that the novel HIPIMS technology developed in this thesis can be easily transferred to an industrial system, making a new generation of DLC coatings available for highly demanding industrial applications.

# Acronyms

**a-C** Amorphous carbon

**a-C:H** Hydrogenated amorphous carbon

**a-C:Me** Metal-doped amorphous carbon

**AFM** Atomic Force Microscopy

**BF** Bright Field

**CAE** Cathodic Arc Evaporation

**CVD** Chemical Vapor Deposition

**DCMS** Direct Current Magnetron Sputtering

**DDP** Digital Diffraction Pattern

**DF** Dark Field

**DFT** Density Functional Theory

**DLC** Diamond-like Carbon

**EDIP** Environment-Dependent Interatomic Potential

**EDX** Energy-dispersive X-ray spectroscopy

**EELS** Electron Energy Loss Spectroscopy

**EM** Electron Microscopy

**ERDA** Elastic Recoil Detection Analysis

**FCVA** Filtered Cathodic Vacuum Arc

**HAADF** High Angle Annular Dark Field

**HiPIMS** High Power Impulse Magnetron Sputtering

**HRTEM** High Resolution Transmission Electron Microscopy

**IBA** Ion Beam Analysis

**IEDF** Ion Energy Distribution Functions

**LAMMPS** Large-scale Atomic/Molecular Massively Parallel Simulator

**MS** Magnetron Sputtering

**MSIB** Mass Selected Ion Beam Deposition

**NRA** Nuclear Reaction Analysis

**OES** Optical Emission Spectroscopy

**OM** Optical Microscopy

**PECVD** Plasma Enhanced Chemical Vapor Deposition

**PIGE** Particle Induced Gamma-rays Emission

**PIXE** Particle Induced X-rays Emission

**PL** Photoluminescence

**PLD** Pulsed laser deposition

**PMS** Pulsed Magnetron Sputtering

**POD** Pin-on-disk

**PVD** Physical Vapor Deposition

**RBS** Rutherford Backscattering Spectrometry

**RFMS** Radio-Frequency Magnetron Sputtering

**SAED** Selected-Area Electron Diffraction

**SEM** Scanning Electron Microscopy

**STEM** Scanning Transmission Electron Microscopy

**Ta-C** Tetrahedral amorphous carbon

**Ta-C:H** Hydrogenated tetrahedral amorphous carbon

**TEM** Transmission Electron Microscopy

**UBM** Unbalanced Magnetron Sputtering

**XPS** X-ray Photoelectron Spectroscopy

# Contents

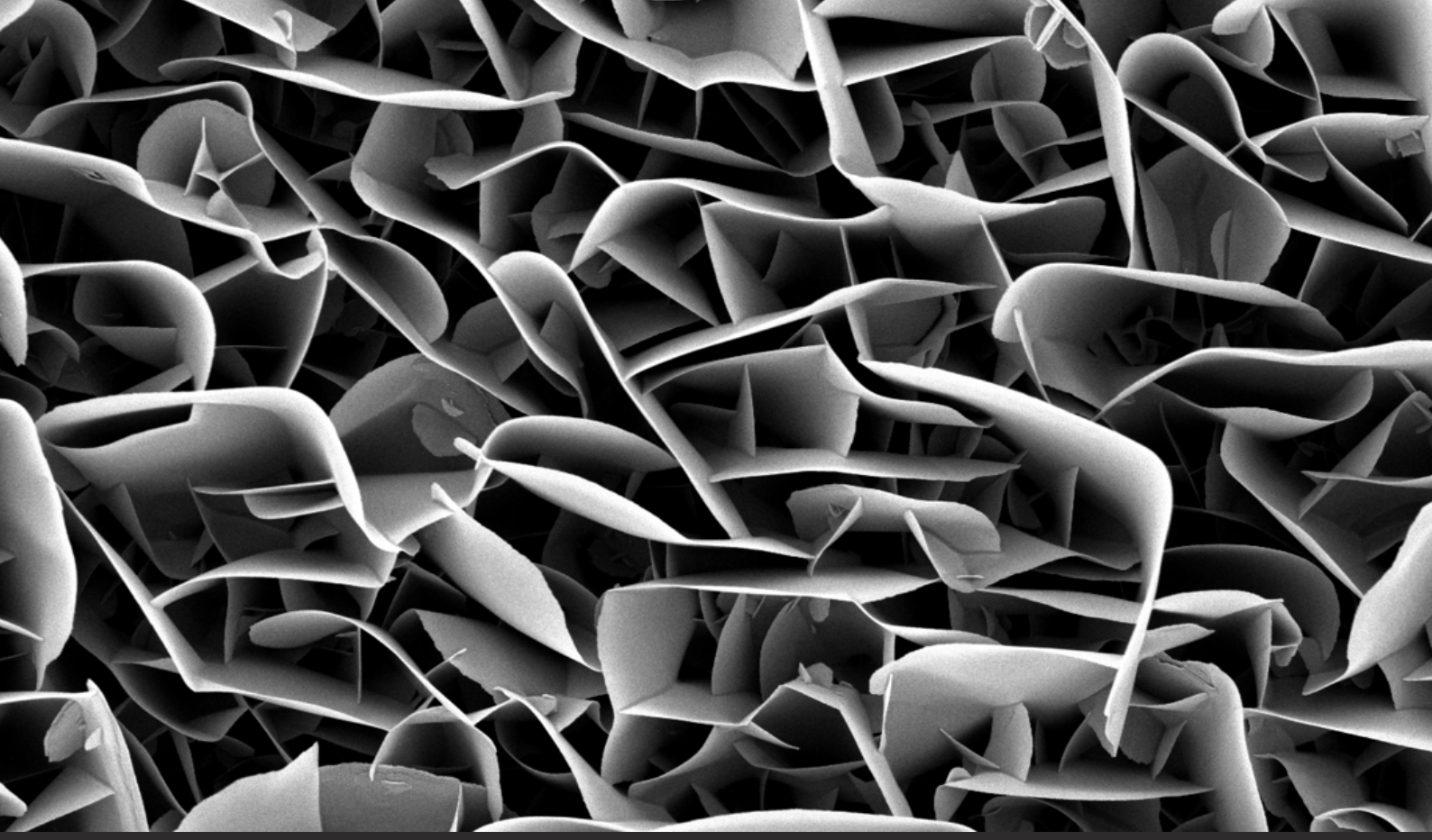

*"No pressure, no diamonds" Thomas Carlyle*

# *Chapter 1*
# Introduction

Carbon-based materials have attracted great interest in the scientific community for decades. Carbon is an extremely light and versatile element that can hybridize in several ways, such as linear ($sp^1$), trigonal ($sp^2$) and tetrahedral ($sp^3$) which leads it to adopt phases such as graphite, diamond, fullerenes, nanotubes and diamond-like carbon among others. Depending on the local bonding, carbon materials can display a huge range of properties such as super-high hardness and thermal conductivity in the case of diamonds, or unusual softness and lubricity for graphite. Because of these outstanding mechanical and tribological properties, carbon has also been a key element in the synthesis of coatings that are now used in a wide range of engineering applications to improve their tribological performance by reducing friction and wear.

# 1.Diamond-like Carbon DLC coatings

The family of DLC coatings is perhaps the largest and represents one of most studied among all carbon coating types. Diamond-like carbon (DLC) coatings are mainly classified as amorphous carbon (a-C), hydrogenated amorphous carbon (a-C:H) and tetrahedral amorphous carbon (ta-C), containing varying proportions of $sp^3$ bonding, which mainly depend on the hydrogen/dopant concentration and the fabrication process. DLC coatings are generally obtained by a deposition process that involves energetic ions in order to promote the metastable $sp^3$ bonding. Fig. 1 shows a ternary phase diagram (first derived by Jacob and Moller [1, 2]) where the different types of DLC coatings are classified according to their $sp^3$ /$sp^2$ fraction (sides of the diagram) and hydrogen content (base of the diagram).

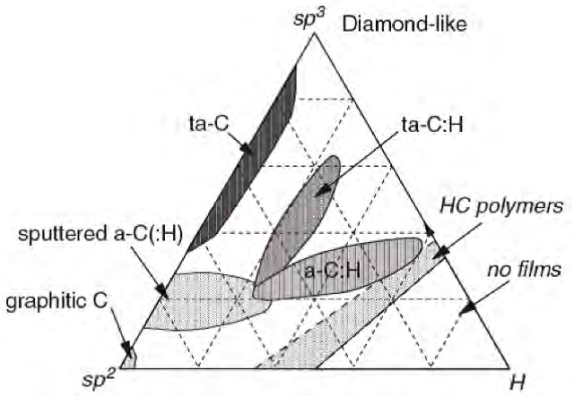


**Figure 1.** *Ternary phase diagram showing the different types of DLC coatings as a function of C bonding and H content.*

The left side of the diagram corresponds to the H-free DLC. Starting at the lower part, near the bottom left corner, we find coatings having a large fraction of $sp^2$ or graphitic a-C, which typically consist of glassy carbon, and are made by pyrolysis of hydrocarbon polymers or evaporation [3]. As $sp^3$ increases along the left side, we find the sputtered a-C coatings, which are typically fabricated by advanced sputtering techniques, such as Unbalanced Magnetron Sputtering (UBM) or High-Power Impulse Magnetron Sputtering (HiPIMS) [4-6]. At even higher $sp^3$ content, we find a specific type of a-C known as tetrahedral amorphous carbon or ta-C. In order to achieve this high $sp^3$ content, deposition methods such as mass selected ion beam deposition (MSIB), filtered cathodic vacuum arc (FCVA) and pulsed laser ablation deposition (PLD) are used [7-10]. These methods allow generating a high ion fraction with a narrowly defined high ion energy during the coating deposition process that promotes $sp^3$ bonding.

A second region of the phase diagram is the bottom right of the figure, where the H content is so large that material cannot form a fully connected network, but exists only as gas molecules. In between this region and the left side, we find a third region, labelled as a-C:H. These coatings are typically produced by plasma-enhanced chemical vapor deposition (PECVD) of hydrocarbon molecules [11, 12]. An alternative production route for this type of a-C:H coatings is to use reactive sputtering of graphite as deposition process in an atmosphere including hydrogen [13]. As deposition methods are evolving towards more energetic techniques, it is possible to produce more dense a-C:Hs with higher proportions of $sp^3$, which are called tetrahedral hydrogenated amorphous carbon or ta-C:H [14].

The diverse properties of DLC are influenced by the different types of bonding that can be found in the films: C-C $sp^3$ , C-C $sp^2$ and C-H bonds. The C-C $sp^3$ bonds mainly govern the mechanical properties (Young's modulus and hardness) [15]. The C-C $sp^3$ bonding leads to a tetrahedral arrangement of bonds resulting in a three dimensional network, resulting in harder films and good isotropic mechanical properties [15]. The C-C $sp^2$ do not contribute much to make the films harder; this type of $sp^2$ bonding is found in graphitic-like layers, providing bonding in-plane and weak bonding out-of-plane, such that layers can easily shear, which is beneficial for improving tribological properties. The C-H bonds normally act as network terminators introducing dangling bonds, and make no contribution to the mechanical properties. Nevertheless, these C-H bonds are of great interest regarding tribological properties, as they allow reducing friction in dry environments [16]. Thus, proper selection of bonding configuration can provide coatings with both, high hardness and low friction under dry sliding conditions. DLC is the only coating material in which this happens, giving them an unsurpassed advantage over competitor coatings in the solid lubrication field, as observed in Fig. 2.

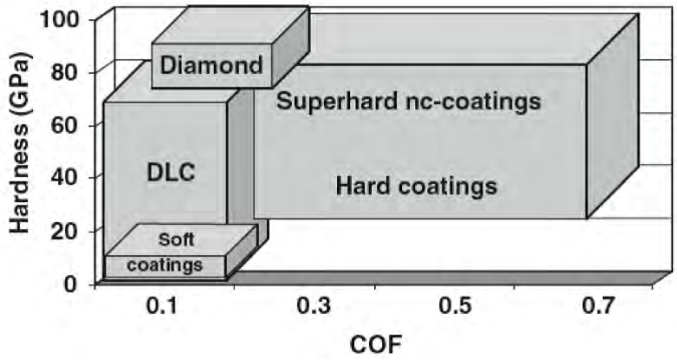


**Figure 2.** *Scheme of hardness and coefficients of friction (COF) for carbon-based and other coating types. [19]*

As a result of this advantage, DLC has made a significant impact on the manufacturing and transportation industries [17-22]. DLC coatings are used in various industries to prevent wear and material transfer during cutting, stamping, molding and rolling operations. In the transportation industry, many fuel injectors in high-performance diesel engines are now coated with DLC, as are a variety of other engine parts such as tappets, valve filters and wrist pins. The oldest and best-known application of DLC is as protective coating on computer hard disks, a technology that has been used for the last four decades [17]. Another emerging application for DLC films is in invasive and implantable medical devices [23]. Nevertheless, the present levels of industrial production of DLC coatings are probably still not reflecting their future potential. One of the aspects that is crucial for future implementation is the need to further reduce the coating costs and also fulfill the finishing quality and coating performance demanded by high-volume, large-scale production sectors (such as microelectronic, transportation and manufacturing). Despite its multiple advantages, DLC also has some drawbacks that must be overcome to produce better quality coatings.

Compressive intrinsic stresses usually develop in fully dense films such as DLC produced from energetic particles or by energetic deposition processes, as those used to produce coatings with a large $sp^3$ fraction. According to the model proposed by Windischmann et al. [29], energetic bombardment of the growing film surface causes displacements of atoms in the film away from their equilibrium positions through primary and recoil collisions. This situation leads to a volume distortion that can cause an excessive stress level and may end up in mechanical damage and early film delamination. For the majority of industrial applications, these issues need to be addressed as the contact loads in operation are pushed to the limit, very close to the yield point of the base material. Consequently, the adhesion of DLC to different substrates needs to be optimized in such a way as to counteract impact, fatigue and abrasive wear exhorted on the coating during operation by increasing its load-carrying capability.

In terms of in-service operation, low thermal stability is also an area of concern that limits the range of operation for DLC films for certain demanding applications. At elevated temperatures (≥250 °C), the advantageous tribological properties of DLC abruptly decay due to the graphitization of the DLC structure. This graphitization process has been detected to occur under many different conditions [30, 31]. The most usual in-service situation where transformation to graphite occurs leading to the degradation of local properties is the wear and friction-induced annealing on local contact areas [16, 32, 33]. For hydrogenated amorphous carbon coatings, at rather low temperatures, around 300ºC, the release of hydrogen from the film surface facilitates the transformation of $sp^3$ into $sp^2$ [34]. The larger the $sp^3$ content the higher the thermal stability [30]. For hydrogen-free carbon coatings, the thermal stability is expected to be higher. For these films, stress relaxation at temperatures close to 400ºC is the main factor associated with mechanical and tribological deterioration [15]. In order to allow higher operating temperatures, it is necessary to explore different approaches to delay the onset of graphitization.

The latest trends in the search for improved performance in demanding applications and environments include the possibility of doping and alloying DLC with different elements such as Si, F, N, O and metals to modify their nature and properties while preserving the intrinsic beneficial properties of the DLC coating [24-28]. In this way, different film properties such as thermal stability, hardness, internal stress, tribological properties, electrical conductivity, surface energy and biocompatibility can be adapted for a specific application.

The study of efficient new ways to improve adhesion and thermal stability of DLC coatings is of great interest for the industry. These improvements will give rise to new exciting opportunities for expanding their range of application.

The final objective of this thesis is to contribute to the expansion of DLC coatings applicability and relevance in industry by providing tailored solutions for industry, as well as improving our current understanding of the underlying physical processes that limit their application, proposing new solutions to overcome some of these limitations.

## 2. Aims and strategy

**The first goal** of this thesis is to deposit DLC coatings with mechanical properties that meet the actual industrial demands for tribological applications.

**Strategy:** in order to optimize the performance of the coatings and to deposit DLC coatings with a high density and $sp^3$ fraction, it is necessary to understand and overcome the issue of the low ionization degree for carbon achieved in conventional magnetron sputtering discharges. To this end, we have developed a new strategy which is based on the use of HiPIMS with the introduction of strong positive voltage reversal discharges at the end of the negative pulses. Such an operation process allows enhancing the ion bombardment on the sample, increasing the $sp^3$ fraction and thus, improving its mechanical properties.

**The second goal** is to develop a pretreatment process for optimizing the adhesion of DLC hard coatings to steel substrates.

**Strategy:** the applied strategy consists on an innovative approach based on the use of HiPIMS technology for metal ion etching. With this strategy, high-energy ions can be used to remove oxides and contamination from the substrate surface. Moreover, high energy ions are implanted at a certain depth underneath the substrate surface, creating a gradual interface which favors the coating-substrate adhesion.

**The third goal** is to evaluate the tribomechanical response of DLC coatings at high temperatures and to propose novel alternatives to overcome the actual limitations of DLC in this field.

**Strategy:** Firstly, the range of temperature where DLC loses its tribomechanical properties will be determined as this still remains unclear in the literature. The deterioration in mechanical properties is associated to structural changes such as graphitization. It is the aim of this work to understand the relationship between mechanical properties and structural modifications. High temperature nanoindentation is used to evaluate the evolution of mechanical properties and high temperature pin-on-disk tests are used to study the frictional behavior of coatings. The work will be completed with the introduction of novel metal-doped DLC coatings for enhanced high temperature tribological behavior. Metals such as Cr, W and Ti will be introduced into the carbon structure by using HiPIMS technology. This process takes advantage of the high ion energy produced by HiPIMS discharges to introduce the metal into the carbon structure without destabilizing the $sp^3$ content.

## 3. Outline of the thesis

After presenting the main aims of this thesis and the selected strategies in the previous two sections of this introductory chapter (**Chapter 1**), the outline of the remaining of the chapters of this thesis is presented as follows:

**Chapter 2** is devoted to introduce the experimental techniques used in this thesis for the synthesis and characterization of the coatings. This chapter includes fundamentals of physical vapor deposition (PVD) deposition methods with special focus on magnetron sputtering and novel techniques derived from conventional sputtering methods such as HiPIMS. In particular, the processes developed to deposit DLC coatings with improved properties will be highlighted. Then the plasma characterization techniques are described. Finally, the techniques used for the microstructural, elemental composition, mechanical and tribological characterization of the coatings are illustrated.

**Chapter 3** focuses on the study of the effectiveness of a novel HiPIMS metal ion etching pretreatment to improve the adhesion of DLC coatings on high speed steel substrates. Two metals (Cr and Ti) were selected for this study. The influence of the HiPIMS pretreatment parameters, the selected metal, and the bonding layers on the microstructure of the substrate-coating interface and the level of adhesion are evaluated. This work has been published in ***Surface and Coatings Technology 349, 2018, 787-796.***

**Chapter 4** describes a novel processing methodology based on the incorporation of positive pulses to a HiPIMS discharge in order to enhance the mechanical properties of DLC coatings. The potential of this technology to increase the ion energy of the plasma discharge is evaluated. The effect of the positive pulses on the structural and mechanical properties of DLC coatings is studied. This work has been published in ***Surface and Coatings Technology 358, 2019, 43-49.***

**Chapter 5** is devoted to analyze the influence of deposition mode and parameters (hydrogen content and temperature, substrate bias, etc.) on the structural properties of the DLC coatings. The influence of the structural properties on the mechanical and tribological behavior is assessed. This study is complemented with computer simulations which allows a complete description of the nanoindentation process and the identification of the atomic-scale mechanism and potential failure precursors for a-C coatings with diverse $sp^3$ content. The computer simulation has been carried out by collaborators PhDs Rafael Gonzalez and Felipe Valencia from the "Universidad Mayor de Chile" (Chile) and Eduardo Bringa from Universidad Nacional de Cuyo (Argentina).

**Chapter 6** explores the potential of metal-doped DLC coatings deposited by HiPIMS technology for tribological applications. The influence of metal dopants such as Cr, W and Ti on the structural, mechanical and tribological properties is investigated. Particular emphasis is placed on high temperature tribomechanical properties. The part of the study dedicated to Cr-doped DLC coatings has been published in ***Surface and Coatings Technology 382 (2020) 124899.***

The thesis closes with a summary of the results and a short outlook (**Chapter 7**), which hopefully will inspire future work in this field of research. Finally, an **Appendix** is dedicated to describe the industrial transfer of the technology developed in this thesis.

---

References:

[1] W. Jacob and W. Moller, App. Phys. Lett., 63, 1771 (1993)

[2] J. Robertson, Mat. Sci. Eng. R. 37, 129-281 (2002)

[3] R. Hauert, Diamond and Related Materials 12 (2003) 583–589

[4] S. Zhang et al., Surface and Coatings Technology 167 (2003) 137–142

[5] D. Camino et al., Vacuum 52 (1999) 125-131

[6] K. Sarakinos et al., Surface and Coatings Technology 206 (2012) 2706-2710

[7] P. J. Fallon et al., Phys. Rev. B 48 (1993) 4777.

[8] M. C. Polo et al., Diam. Relat. Mater. 9 (2000) 663.

[9] Y. Lifshitz et al., Diam. Relat. Mater. 4 (1995) 318.

[10] V. I. Merkulov et al., App. Phys. Lett. 73 (1999) 1228.

[11] P. Koidl et al., Mat. Sci. Forum 52 (1990) 41.

[12] C. Donnet et al., J. App. Phys. 85 (1999) 3264.

[13] W. Tillmann et al., Surface and Coatings Technology 206 (2011) 1705-1710

[14] M. Weiler et al., Phys. Rev. B. 53 (1996) 1594.

[15] A.C. Ferrari, J. Robertson, Phys. Rev. B, 61 (2000) 14095

[16] A. Erdemir et al., Surface and Coatings Technology, 86-87 (1996) 692-697

[17] M. Schlatter, Diamond and Related Materials 11 (2002) 1781–1787

[18] J. Vetter, Surface and Coatings Technology 257 (2014) 213–240

[19] Tribology of Diamond-Like Carbon films: Fundamentals and Applications, Springer, N. York, 2007

[20] Tetrahedrally bonded amorphous carbon films I: basics, structure and preparation, Springer series in Material science 263, 2018

[21] A.A. Voevodin, Surface and Coatings Technology 116–119 (1999) 36–45

[22] A. Erdemir et al., Current Opinion in Solid State & Materials Science 22 (2018) 243–254

[23] G. Dearnaley et al., Surface and Coatings Technology 200 (2005) 2518 – 2524

[24] K. Oguri et al., Surface and Coatings Technology 47 (1991) 710 – 721

[25] E. Broitman et al., Wear 248 (2001) 55–64

[26] JC. Sánchez-López et al., Doping and alloying effects on DLC coatings, Tribology of Diamond-Like Carbon films: Fundamentals and Applications, Springer, N. York, 2007

[27] S.C. Trippe et al., Thin Solid Films 446 (2004) 85–90

[28] M. Grischke et al., Diamond and Related Materials 7 (1998) 454–458

[29] H. Windischmann et al., Critical Reviews in Solid State and Mat. Sci., 6, 17 (1992)

[30] A. Erdemir et al., Surface and Coatings Technology, 76-77, 559-563, (1995)

[31] K.Y. Li et al., Wear, 258, 1577-1588 (2005)

[32] C. Donnet et al., Tribology Letters, 9 (3-4), 137-142 (2000)

[33] Y. Liu et al., Surface and Coatings Technology, 82, 48-56 (1996b)

[34] P. Koidlet et al., Materials Science Forum, 52, 41(1990)

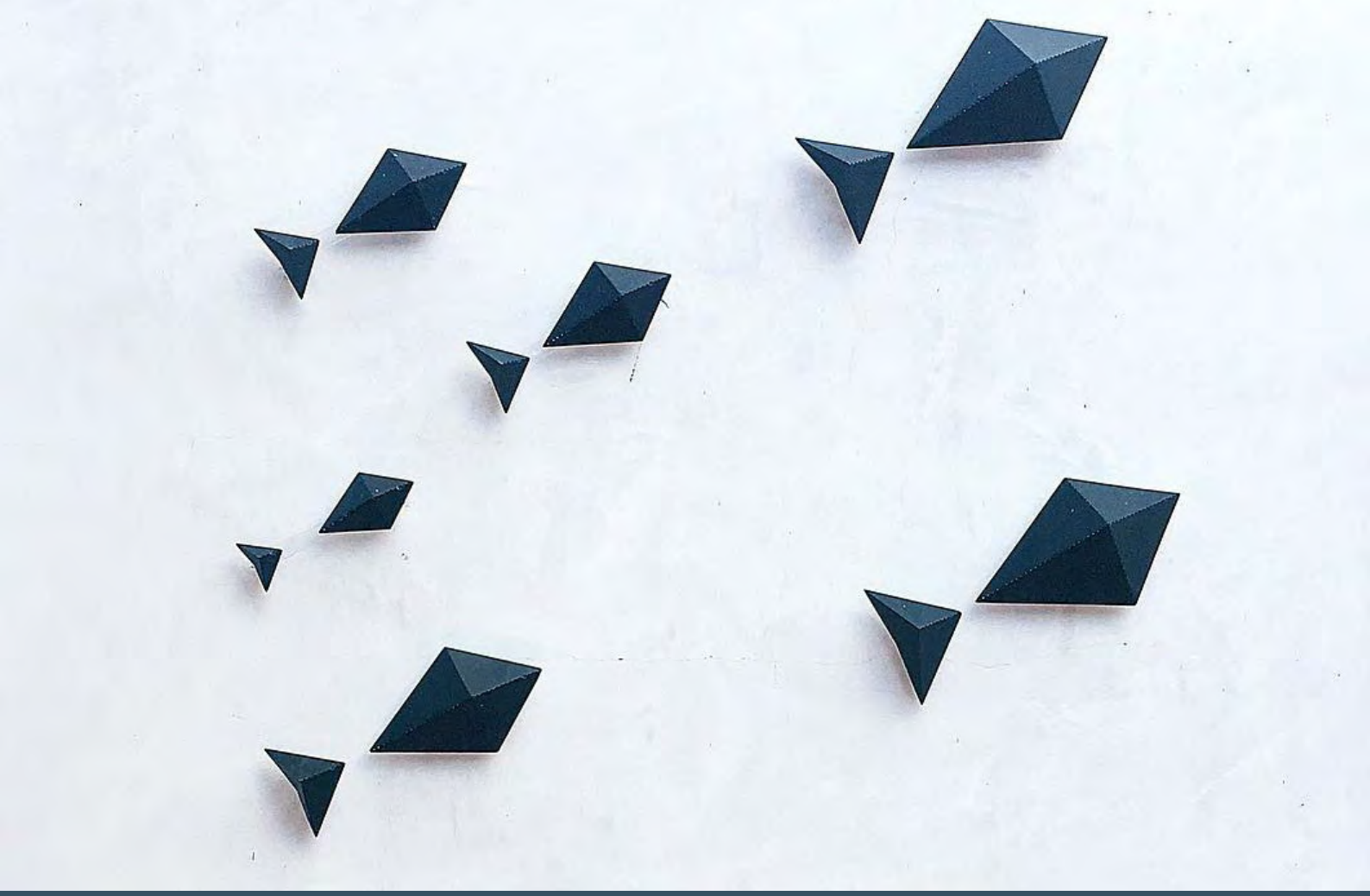

*"A diamond is just a lump of coal that stuck to its job." Leonardo da Vinci*

# Chapter 2

# Synthesis and characterization of sputtered DLC coatings

The first part of this chapter is devoted to the description of the fundamentals of the main deposition methods used for the synthesis of DLC coatings, with particular emphasis on the chosen method and plasma characterization techniques used in this thesis. In the second part, all the techniques used in this thesis for the characterization of the structural, mechanical and tribological properties of deposited coatings are described.

# 1.Synthesis of DLC coatings by sputtering methods

The deposition of the coatings studied in this thesis has been performed by using magnetron sputtering-based methods. In the following sections, an introduction to physical vapor deposition (PVD) processes is given, focusing on the peculiarities of conventional and high-power impulse magnetron sputtering (HiPIMS) methods.

## 1.1. Physical vapor deposition methods

Physical vapor deposition (PVD) is used to designate a group of vacuum-assisted methods to fabricate thin films using physical processes, either evaporation or sputtering. These methods are widely used for the synthesis of DLC coatings both at laboratory and industrial scale. Among all the available PVD techniques, those used for the deposition of DLC coatings are cathodic arc evaporation (CAE), pulsed laser deposition (PLD) and sputtering, especially magnetron sputtering-based methods. In this thesis, sputtering is the selected method for the deposition of the coatings, because of its many advantageous characteristics, including: easy control, environmental friendly, versatility, scalable and low cost. Therefore, in the following, the sputtering process is described in detail.

In sputtering, the material to be deposited is bombarded with energetic ions extracted from a glow discharge (plasma). Through momentum transfer from the impinging ions to the target material, atoms are ejected or sputtered. In general, the gas used for sputtering is Ar, although in the so called reactive sputtering some other gases such as H, N or O are commonly used, normally in conjunction with an inert gas, like Ar. To produce an effective sputtering, ions from the plasma are accelerated towards the target by applying a negative potential to it. As a result, various ion-solid surface interactions occur. A schematic representation of the sputtering process is illustrated in Figure 1.

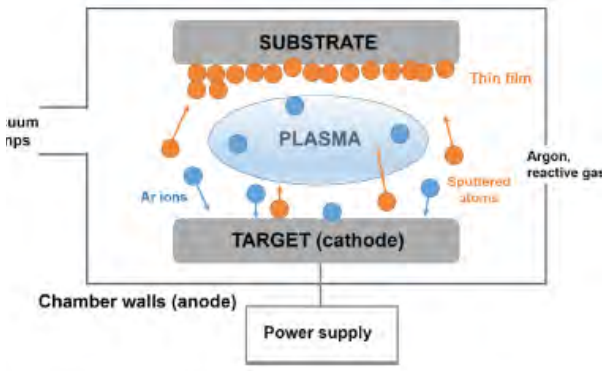


**Figure 1.** *Schematic representation of the sputtering process.*

The ion-target interaction is influenced by many factors such as: the energy and the angle of incidence of the ions, the binding energy of the target atoms, the mass of the incident ions and of the target atoms, etc. As a consequence of these interactions, a fraction of the target atoms are sputtered away and traverse the plasma through their course until arriving at the substrate. In this travel, sputtered atoms suffer elastic collisions with background gas atoms and they are subsequently thermalized. However, it may be that not all the atoms are thermalized but a fraction of them can also be ionized due to the inelastic collisions with electrons present in the plasma. This process turned out to be the main reason for the development of magnetron sputtering [1, 2].

## 1.2.Magnetron sputtering

Magnetron Sputtering is an upgrade of early sputtering techniques which was developed in order to increase the ionization efficiency of the plasma. During a conventional sputtering discharge, the amount of ejected secondary electrons is low for most metals [3]. Therefore, in order to achieve an easier sustainability of the discharge it is highly desirable to enhance the ionization efficiency of the secondary electrons [4]. This can be achieved by placing strong permanent magnets on the back of the targets so that the resulting magnetic field confines the

electrons in a region close to the target surface, which notably increases the probability of ionizing the neutral gas, creating more ions out of it. These ions are then able to participate in the bombardment of the target increasing the sputtering rate [5].

Depending on the power mode delivered to generate the glow discharge, it is possible to classify the magnetron sputtering technique in various methods: DCMS (Direct Current Magnetron Sputtering), RFMS (Radiofrequency Magnetron Sputtering) and HiPIMS (High Power Impulse Magnetron Sputtering).

DCMS is the most commonly used sputtering-based method for the synthesis of thin films. In DCMS, a constant power is applied to the target keeping the target power density in the order of a few $W/cm^2$ and the current densities below 100 $mA/cm^2$. This provides plasma densities in the range of $10^{14}$-$10^{16}$ $m^{-3}$. The resulting ionized fraction of the sputtered metals in the DCMS method is rather low [6, 7] and the majority of the depositing flux consists of neutral species. This means that energetic deposition conditions are difficult to achieve by using DCMS. A common approach to overcome this problem is the application of a negative bias voltage to the substrate. Such a bias drives the displacement of plasma ions towards the substrate. Therefore, the application of a suitable substrate bias voltage allows the control of the energy of the arriving particles up to certain extent. In general, the higher the negative bias voltage, the more energy is transferred to the substrate by the positively charged ions.

A better way to achieve "high" energetic conditions is to increase the plasma density which in turn relies on the target power density [8]. However, the heat sinking at the target limits the power densities that can be achieved using a constant power. One way to better manage thermal loads is to use pulsed magnetron sputtering.

Pulsed magnetron technology was initially developed to overcome limitations taking place during reactive sputtering deposition of poorly conducting thin film materials (e.g. many transparent oxides). The main limitation for the deposition of these materials when using DCMS was that the sputtering process tends to get unstable because the anode and especially the target itself get covered with an insulating layer. In consequence, due to the negative polarity of the target, positive charges are accumulated on its surface producing a high electric field across the surface layer which can lead to the production of arcs and eventually to breakdown. Under these conditions, arcing and the associated extreme local heating would lead to the emission of particles such as droplets that finally contribute to deteriorate the quality of the deposited films. One way to prevent arcing was to periodically interrupt the negative D.C. voltage applied to the target. This working mode is called DC-pulsed magnetron sputtering [9]. During the interruption of the negative D.C. voltage applied to the target, referred to as the "off" time, and due to the high thermal current density of the electrons compared to the heavy and cold ions, the surface of the insulating layer is subjected to a net negative flux which neutralizes the accumulated positive charge. The selection of proper pulse parameters allows preventing electrical breakdown and droplet emission, favoring the deposition of films free of such impurities and with a denser structure, as reported in several publications [10, 11].

Typical pulse parameters are shown in Figure 2. It is observed that during a certain time ($t_{on}$) a negative potential is applied which is periodically switched off during a certain time denoted as $t_{off}$. Both, the $t_{on}$.and $t_{off}$. times define the pulse period (T) or its inverse, the pulse frequency (f). The $t_{on}$ /T ratio is defined as the duty cycle (η) of the discharge:

$$\eta = \frac{t_{on}}{t_{on} + t_{off}} = \frac{t_{on}}{T} = f \bullet t_{on} = 1 - f \bullet t_{off}$$

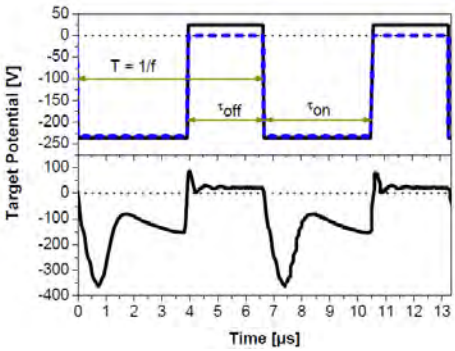


**Figure 2.** *Target potential waveforms in pulsed magnetron sputtering configuration. (Top-blue dashed line) For comparison, theoretical waveform where the pulse parameters are displayed. (Top black) Theoretical waveform for a typical bipolar discharge. (Bottom black) [12]*

In this context, to achieve an efficient deposition, the "on" time has to be long enough for the ions to cross the sheath (region between the plasma and the electrodes) and gain their full energy, but it has to be short enough to prevent arc formation. Thus, the discharge must be switched off before the accumulated charge is large enough for the breakdown to happen.

The "off" time has to be selected to be at least long enough to complete the decay of the plasma. Indeed, it is usually designed to allow a complete neutralization of the accumulated charge on the insulator surface.

These requirements imply that practical DC-pulsed magnetron discharges are operated in the frequency range from few kHz up to hundreds of kHz, which can be followed by ions and therefore, electrons, with duty cycles between 0.1 and 0.9. It is worth noting that sometimes it is more convenient to apply a small positive potential (asymmetric bipolar mode) to the target during the "off" time than to switch it "off" and keep the target at ground potential (unipolar mode) (see Fig. 2 top, dashed blue versus black waveforms). An accurate explanation about the influence of the application of a positive potential during the "off" time on the deposition of DLC films is given in Chapter 4.

## 1.3. High impulse power magnetron sputtering (HiPIMS)

High impulse power magnetron sputtering (HiPIMS) is a relatively recent advance in pulsed sputtering configuration in which the power is applied to the target in short pulses using cathode voltages higher than 500 V with low duty factors (<10%) and frequencies from tens of Hz to several kHz. As shown in Fig. 3, these conditions result in high peak power densities, around several kW/cm$^2$.

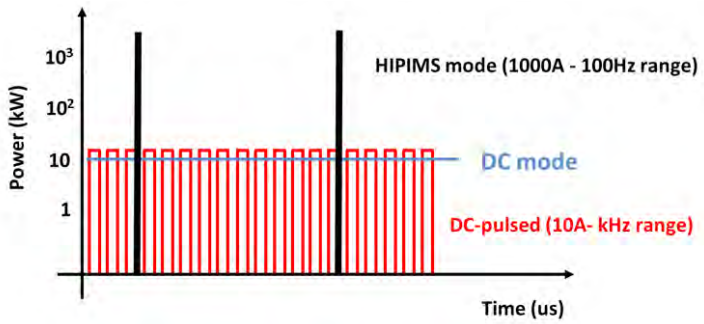


**Figure 3.** *Schematic comparison of different sputtering methods: DC mode, DC-pulsed and HiPIMS*

The HiPIMS process conditions have been shown to promote higher levels of ionization of the sputtered metals [13, 14] as well as relatively higher energies of the sputter-ejected metal ions as compared to the DCMS configuration [15]. Plasma conditions achieved in HiPIMS have been shown to enable the deposition of ultra-smooth and dense films [16, 17]. Furthermore, uniform film deposition on complex-shaped substrates, improved film adhesion to the substrates and the possibility of low-temperature synthesis of thin films have also been demonstrated by HiPIMS [18].

HiPIMS discharges are characterized by their current waveforms. Indeed, many important aspects of the discharge can be inferred by analyzing its time evolution. Typical current characteristic curves from a HiPIMS discharge are presented in Fig. 4.

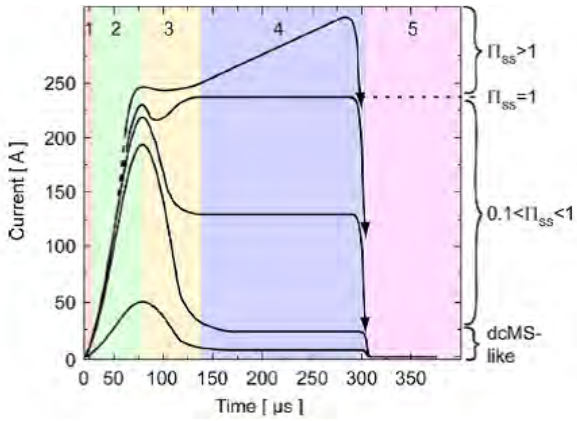


**Figure 4.** *Schematic illustration of typical target current waveforms in HiPIMS discharges. The time-evolution of the target current is described in 5 phases: discharge ignition (1), plasma build-up (2), gas rarefaction (3), target self-sputtering (4) and plasma decay (5), [19].*

In this figure, we observe that the time-evolution of the target current can be described in five phases: (1) discharge ignition, (2) plasma build-up, (3) gas rarefaction, (4) target self-sputtering and (5) plasma decay [19]. In the plasma ignition phase (phase 1), secondary electrons are generated and collected near to the target by the magnetic field to feed the plasma discharge. During the plasma build up (phase 2), the current increases as the electron population does. At this point, the plasma is constituted mainly by sputtering gas ions. After this period, the sputtering gas ions are depleted due to the intensive ionization and because of their collisions with the sputtered target material atoms, the so-called gas rarefaction (phase 3). In phase 4, the target material atoms are also ionized and they contribute to the sputtering process. Thus, in phase 4 the target is sputtered by a mixture of process gas and target ions. Depending on the discharge conditions and the kind of target material, the target current can either reach higher or lower values in a sustained ($\Pi_{ss} \geq 1$) or non-sustained ($\Pi_{ss} \leq 1$) self-sputtering phase. Finally, the target current rapidly drops when the plasma species are lost by recombination and diffusion to the chamber walls (phase 5).

The influence of the discharge characteristics of the HiPIMS process on the adhesion of DLC coatings to HSS substrates by using Cr and Ti ions is investigated in Chapter 3. Novel HiPIMS configurations with the implementation of positive pulses at the end of the regular negative discharges and its influence on the mechanical properties of the DLC coatings is studied in Chapter 4. The synthesis of a-C and a-C:H films by HiPIMS technology is explored in Chapter 5. Finally, Chapter 6 examines the potential of high-density Cr-HiPIMS plasma discharges for Cr-doped DLC coatings with enhanced tribomechanical behavior at high temperature.

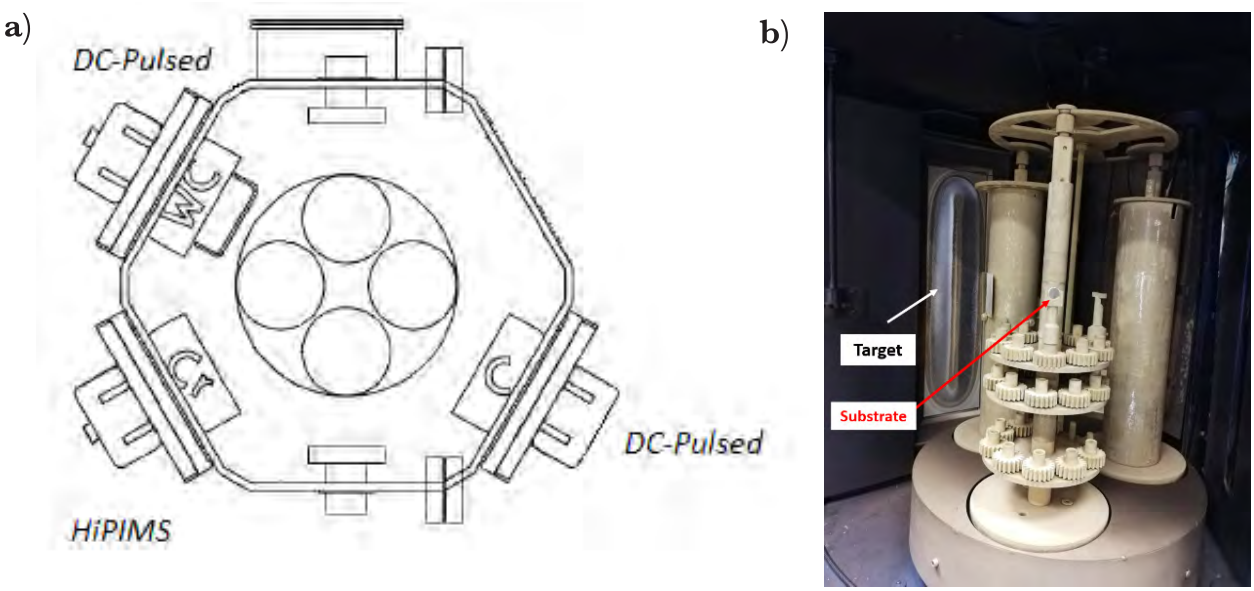


**Figure 5.** *(a) Schematic view of the sputtering system used in this thesis (b) Image of the laboratory system used for DLC coatings deposition.*

## 1.4. Semi-industrial laboratory system

The setup used for the deposition of the DLC coatings studied in this thesis is a small-medium batch coater system which is equipped with two large magnetron cathodes, used for the deposition of WC and DLC and an additional small magnetron cathode which has been used for the deposition of metal bonding layers as well as of Me-doped DLC. The schematic cross-sectional view (Fig. 5a) shows the substrate table with the substrates on a planetary system, the cathodes disposal and the configuration used during deposition. The vacuum chamber of the coating system is shown in Fig. 5b.

The most important hardware elements are listed below:

a) Plasma sources

- 2 large rectangular magnetron cathodes (length 40 cm x width 10 cm) from Gencoa Ltd. equipped with:
  - Graphite target
  - WC/Co target (6%wt Co as binder material)
- 1 small circular magnetron cathode (diameter 2") equipped with either Ti or Cr
- 1 DC-pulsed power supply from Advanced Energy (Pinnacle Plus – 10 kW average power and 150 kHz max. frequency)
- 1 HiPIMS power supply from hip-V (6 kW average power, 500 A peak current)

b) Substrate table and shutters

- 1 continuously operated cathode shutter
- Substrate rotary table (2-fold rotation up to 5 rpm)

c) Vacuum and gases

- 1 turbomolecular pump (nominal capacity 600 l/s)
- 1 rotary pump (nominal capacity 20 $m^3$/hr)
- 2 mass flow controllers for process gases (Ar, $C_2H_2$)

d) Sensors

- Thermocouple
- Penning gauge

e) Automation

- Visualization unit
- Speedflo from Gencoa Ltd.

A mixed load of test coupons, silicon wafers and/or components were used for coating deposition. The substrates used and the process sequence for each step are described in the relevant chapters of the thesis as different processes have been carried out.

## 1.5. Plasma characterization

Because of its large influence on the properties of the sputtered coatings, the study of the plasma properties is a key point in order to develop more energetic processes and to achieve coatings with improved properties. Therefore, in this thesis we have studied the dynamics and the composition of the plasma discharges by means of optical emission, mass spectroscopy and by analyzing target and substrate voltage-current waveforms.

### 1.5.1. Optical Emission Spectroscopy

Optical emission spectroscopy (OES) is often used for plasma diagnostics. This method is based on measurements of light emission radiated outwards from plasma volume as a function of wavelength.

The operation of an OES setup can be described as follows: the optical emission from a plasma discharge is collimated and subsequently directed to a slit. The grating and mirror arrangement resolve the component wavelengths of the collected emission. The obtained spectrum is sent to a photo-diode array or to a CCD camera, which converts the optical signal into an electrical one. The electrical signal is further sent to the processing unit.

In this way, a spectrum containing the emission intensities plotted against the wavelength of the radiations from the plasma constituents is obtained.

In this thesis, OES measurements were carried out during the deposition process of DLC coatings in both DCMS and HiPIMS configurations. Measurements were performed by using a Speedflo developed by Gencoa Ltd. coupled to a plasma emission monitoring module. The light was collected by a fiber located in a window in one side of the deposition chamber and from there it is directed to the entrance slit of the spectrometer. In this setup, the spectral range goes from 200 to 1000 nm and its resolution is 0.5 nm. The spectra were recorded using the Speedflo software developed by Gencoa Ltd.

OES provides qualitative information about the ionized fraction of the different species present in the plasma, but it does not allow us to accurately quantify them. For quantification, mass spectrometric measurements were performed.

### 1.5.2. Mass Spectroscopy

Mass spectroscopy (MS) was used as a complementary to OES to quantify the fraction of the different species present in the plasma. Mass spectroscopy is an analytical technique that ionizes chemical species, separates the ions in a mass analyzer according to their mass-to-charge ratio, and finally, detects the ions, recording their relative abundance. Therefore, MS allows measuring the energy distribution of the different ions present in the plasma. By inserting an extraction probe into the plasma, the mass spectrometer uses both electric and magnetic fields to filter incoming ions with respect to their energy and mass-to-charge ratio. This means that if we want to study neutral species, they first have to be ionized. Ionization is achieved by activating an ionization stage situated inside the extraction orifice consisting of a hot filament which emits electrons. These emitted electrons allow the ionization of the neutral atoms via impact ionization.

The energy resolution is achieved by using energy filters which consists of electrodes that retard and focus the incoming ions. For mass filtering, a quadrupole mass filter with four parallel electrodes was used. It consists of parallel electrodes to which a constant (DC) or a variable (AC) potential is applied. In such a device the ion trajectories are separated depending on the mass-to-charge ratio. Therefore, depending on their mass, some ions will pass the filter while others are deviated from their original path. Finally, the ions are detected with a secondary electron multiplier and monitored.

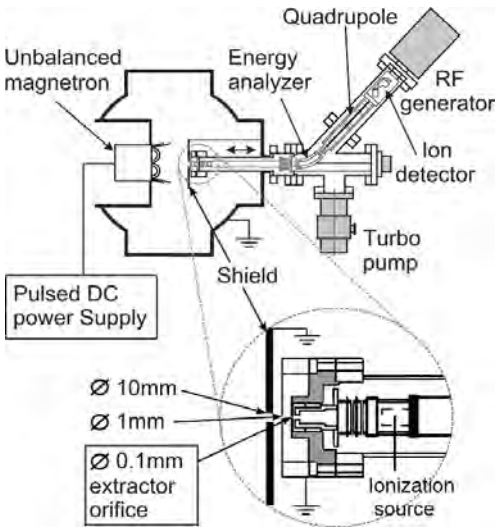


**Figure 6.** *Schematic description of the setup used for mass spectroscopy measurements*

In this thesis, the time-averaged energy-resolved spectra of positive ions were measured with a Hiden EQP 300 spectrometer which was attached to the deposition chamber. An schematic picture of the placement of the spectrometer in the vacuum chamber is shown in Fig. 6. Starting from left in the figure, the spectrometer consists of (i) a extraction section, (ii) an ionization source, (iii) energy analyzer, (iv) quadrupole and (v) ion detector. The entrance of the spectrometer (extractor orifice) is placed at a distance of 130 mm from the target. The Hiden EQP 300 mass

spectrometer system couples the exit of the spectrometer to a removable radio frequency head ("RF Head") and an electrostatic analyzer head. The analyzer head is connected to a mass spectrometer interface unit which continuously transmits the data collected to the control PC. The description of the measurement procedure used in this thesis to evaluate the ionization of carbon HiPIMS plasma discharges is described in Chapter 4.

# 2. DLC films characterization

## 2.1. Elemental composition analysis

### 2.1.1. X-ray photoelectron spectroscopy

X-ray photoelectron spectroscopy (XPS) provides information on the composition and stoichiometry of all the elements present in a material, in concentrations larger than 0.1% atomic (except Hydrogen and Helium due to their low cross section). In principle, XPS is a surface sensitive analytical technique with a typical analysis depth of less than 5 nm. However, this technique also allows characterization of the elemental concentration as a function of depth when it is combined with ion etching. Ion etching is also normally used to remove the contaminated surface layer which could negatively influence the accuracy of the analysis.

XPS relies on the interaction of X-rays with the sample surface which leads to the ejection of photoelectrons whose kinetic energies are measured under ultra-high vacuum conditions. By the principle of conservation of energy, the chemical binding energy can be calculated and the different intensities measured at different energies giving rise to characteristic peaks that allow elemental identification and quantification.

When dealing with DLC samples, XPS is a useful non-destructive method to evaluate the structure of DLC films because it can reveal the binding energy of the carbon atoms and discern between $sp^3$ and $sp^2$ hybridizations [23, 24]. XPS is also highly sensitive to the bonding environment of the studied elements, which is particularly interesting to characterize the structure of the doped DLC films [25]. In addition, XPS was used to investigate the formation of carbides in the studied Cr-doped DLC as well as to estimate the metal dopant contents. Moreover, it was also used as a first assessment to quantify the $sp^3$ content for the deposited DLC coatings.

In this thesis, XPS spectra were measured using a VG ESCALAB 210 instrument, which was upgraded with a SPECS Phoibos 100 DLD hemispherical electron energy analyzer. Non-monochromatic Al Kα radiation (1486.6 eV) was used as X-ray excitation source. The measurements were performed in constant analyser energy mode with a 35-eV pass energy for high resolution spectra of the detected elements. In order to minimise surface contaminants (i.e. ubiquitous C, oxides…), samples´ surfaces were sputter-etched using Ar+ ion bombardment at 10-4 Pa (2 keV; 15-20 μA) during 10 min. For the quantitative elemental characterization, the area under the C 1s, O 1s and Cr 2p peaks was calculated following a Shirley background subtraction and accounting for the relative sensitivities of the elements using Scofield cross-sections. Then, the relative amount of the different carbon bonds (carbides, C-C, C=O and carbonates) was obtained by performing a least square fit of the C 1s peaks, in agreement with previous works [26].

### 2.1.2. Ion Beam Analysis techniques

Ion Beam Analysis (IBA) is a family of analytical techniques which use a beam of high energy (MeV) ions to study the elemental composition of materials. When accelerated ions strike a material, they interact with the electrons and nuclei of the material atoms, slow down and possibly deviate from their initial trajectory. This lead to the emission of particles or radiation whose energy is characteristic of the elements which constitute the sample material.

IBA techniques can be characterized and divided according to the main interaction process that is analysed into: Rutherford Backscattering Spectroscopy (RBS), Elastic Recoil Detection Analysis (ERDA), Nuclear Reaction Analysis (NRA), Particle Induced X-rays Emission (PIXE) and Particle Induced Gamma-rays Emission (PIGE) among others. A brief overview of the different IBA techniques and the main interaction processes is shown in Table 1.

In general, IBA techniques are usually multi-elemental, non-destructive, relatively fast and do not require sample preparation.

**Table 1.** *Summary of the different IBA techniques and their operating principles*

| Acronym | IBA technique | Interaction |
|---|---|---|
| **RBS** | Rutherford Backscattering Spectrometry | Elastic scattering at backward angles |
| **ERDA or FRS** | Elastic Recoil Detection Analysis, Forward Recoil Spectroscopy | Elastic recoil at forward angles, not necessarily Rutherford |
| **NRA** | Nuclear Reaction Analysis | Nuclear reaction between incident beam and nuclei in the target, producing a light charged particle |
| **NRP or RNRA** | Nuclear Resonance Profiling, Resonant Nuclear Reaction Analysis | Exploitation of narrow nuclear resonances via scanning of the incident beam energy |
| **PIXE** | Particle-Induced X-ray Emission | Characteristic X-ray emission following ionization by the primary beam |
| **PIGE** | Particle-Induced Gamma Emission | Prompt gamma emission during ion beam irradiation |

In this work, RBS was used to characterize the elemental composition of the Me-doped DLC coatings, whereas RNRA was used to determine the H content in the hydrogenated DLC coatings. A brief overview of these techniques and of the particular experimental conditions selected to carry out the measurements is given next.

### Rutherford Backscattering Spectroscopy

Rutherford Backscattering Spectroscopy (RBS) is based on nuclear elastic scattering of the incident ion by the nucleus of the target atom. The backscattered ions and their energy are then detected by a suitably positioned detector. The RBS method can be used for quantitative determination of the amount of target atoms (without the need for reference samples and with moderate mass resolution) and also for their depth distribution, with a resolution of the order of several nm. RBS is non-destructive and provides a very good sensitivity for heavy elements, in the order of parts-per-million (ppm). Because of the stopping power of ions in matter, the analyzed depth is typically ~2 μm for incident He-ions and ~20 μm for incident protons. The drawback of RBS is its low sensitivity for light elements, which often requires the combination of other nuclear based methods like nuclear reaction analysis (NRA) [27] or elastic recoil detection (ERDA).

Experimental measurements indicate that the cross sections differ from Rutherford when the energy of the incident ion is such that its interaction with the sample atoms cannot be considered merely Coulombian. In these cases, when the cross section is represented in relation to the energy of the incident ion, it significantly increases for certain energy ranges. This enhanced cross-section is known as resonant or non-Rutherford and it is the basis of the analytical technique called Non-Rutherford Backscattering (Non-RBS).

In this thesis, Non-RBS measurements were performed using a He beam at 4263 keV at which the cross-section for C is Non-Rutherford which, as previously mentioned, increases the sensitivity for its detection. Measurements were performed in a high vacuum chamber which is connected to a 3 MV tandem accelerator model 9SDH-2 of NEC [28] located at the Centro Nacional de Aceleradores (CNA/CSIC) in Seville. The backscattered ions were detected by a standard Si-barrier detector located at an angle of 165º.

The elemental composition of the samples was estimated by comparing measured and simulated spectra. For the simulations, the SIMNRA commercial computer code [29] was used.

### Nuclear Reaction Analysis.

Nuclear Reaction Analysis (NRA) describes a group of analytical techniques based on nuclear reactions which occur when the impinging ion interact with the atoms in the samples producing a nuclear reaction. As a consequences of this nuclear reactions, charged particles (particle-particle reactions) or γ-rays are produced (particle-induced γ.reactions, PIGE). These nuclear reaction products are further detected, allowing us to obtain information about the elemental composition and depth profiling. While RBS is the method of choice for the detection and depth profiling of medium mass and heavy elements, NRA is widely used for the quantitative determination and depth profiling of light elements. Because NRA is isotope specific, a measurement at a specific energy and with a specific incident ion species detects only one (or maximum a few) different isotopes, and the

composition of a target cannot usually be determined by only one measurement, requiring measurements at different energies and/or different incident ion species. Some other drawbacks to be considered when carrying out NRA experiments are:

- The effective cross sections are usually lower than those for RBS. Therefore, it is necessary to accumulate enough statistics to obtain a good resolution.
- Sometimes, more than one nuclear reaction can be produced in the same sample, resulting in an overlap of peaks in the experimental spectrum, which makes the data interpretation and analysis difficult.
- Necessity of standards for a proper quantification.

Depending on the shape of the cross section within the selected energy interval, the technique is named non-resonant or resonant nuclear reaction analysis (RNRA and NRA, respectively). The first makes use of flat cross section whereas, in the second sharp resonances (with a typical width of some keV) are used.

In this thesis, RNRA measurements were carried out to accurately determine the H content in the hydrogenated DLC coatings. The H content of the samples was estimated as a function of the $P_H/P_{Ar}$ at different depths (40, 60, 80, 90 and 100 nm). RNRA experiments were carried out at the Forschung Zentrum Dresden Rossedorf (HFZDR) by using the $H(^{15}N,He\gamma)1^2C$ [30] nuclear reaction with a $N^{2+}$ beam impinging onto the sample surface at normal incidence. This reaction has a sharp resonance at 6.385 MeV. The beam energy was varied in the range from 6.457 to 6.547 MeV. The 4.43 MeV γ-rays were detected by a 4 × 4 $inch^2$ BGO detector mounted immediately outside the vacuum chamber about 1.5 cm behind the sample. Some special precautions were taken in order to carry out reliable depth profiling measurements and to avoid ion beam-induced hydrogen diffusion [31]. The beam spot and the current were selected to be 2 × 2 mm2 and ~10 nA, respectively. In addition, the beam spot position was changed every two measurements. As described in Ref [32], in order to assure that the selected experimental configuration does not lead to ion beam-induced diffusion, several spectra were sequentially measured on the same point up to a dose 10 times higher than that used in these experiments. No ion beam-induced hydrogen diffusion was detected in any case.

## 2.2 Morphological and structural characterization

### 2.2.1. Optical microscopy and profilometry

The morphology of all the deposited coatings in this thesis was initially investigated by optical microscopy (OM). The operating principle of optical microscopes is to create a magnified image of an object by using visible light and a series of lenses. In this thesis, OM images were taken by a Leitz Laborlux 12 ME microscope. The instrument has a magnification of up to 200x and uses a CCD camera to generate an image, which is finally displayed on a computer screen. The topography of the samples was also characterized by optical profilometry (OP).

OP is a rapid, nondestructive, and noncontact surface technique. An optical profiler is a type of microscope in which light is split into two paths by a beam splitter. One path directs the light onto the sample surface, whereas the other does to a reference mirror. The differences in the topology of the sample will alter the path lengths of the reflected beam which leads to diverse interference patterns. From the study of the interference patterns a 3D profile can be derived. Vertical resolution can be of several angstroms while lateral resolution, depends on the objective, being typically in the range of 0.3-8 microns.

In this thesis OP was used for evaluating the worn volume after tribological testing and the residual stress in deposited DLC films. Measurements were performed by using a three-dimensional optical profilometer, Leica DCM 3D with a vertical resolution of ~0.1 nm and lateral resolution lower than 0.5 μm.

### 2.2.2 Electron Microscopy (EM)

The resolution of features in optical microscopy is limited by the wavelength of the incident light so that if the features are smaller than the wavelength, they cannot be resolved. As the wavelength is much smaller for electrons than for photons of the same energy, an electron microscope has much better resolution and it allows to see finer details at higher magnifications.

In an electron microscope, the electrons produced by an electron gun are further accelerated, up to energies typically in the the range of some KeV, and focused on the sample surface. During the electron-matter interaction different types of signal are generated, which reveal information about the sample morphology, chemical composition, and crystalline structure. A schematic picture of the different electron-sample interactions is given in Fig. 7. Depending on the operation modes, two main types of electron microscopes can be distinguished: Scanning electron (SEM) and transmission electron (TEM). Their operation principles are described in the following:

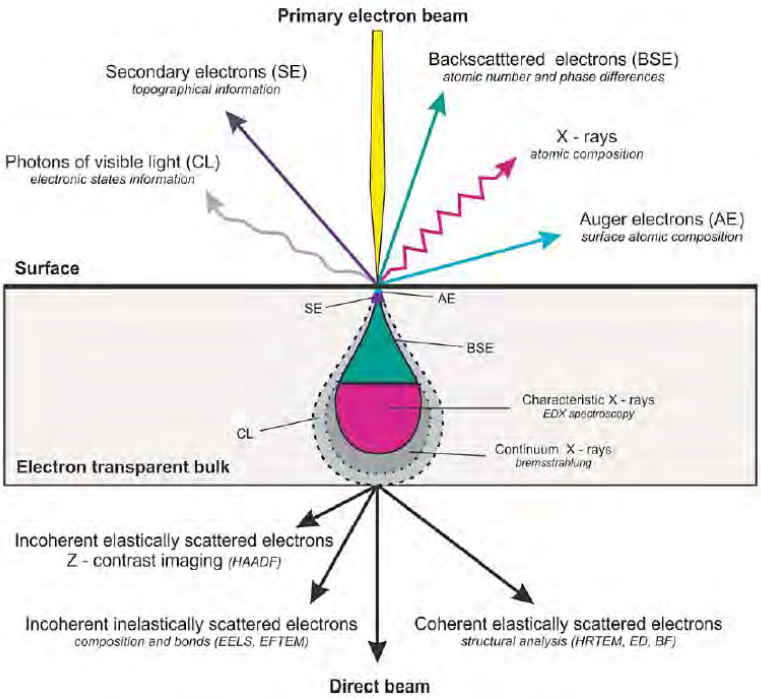


**Figure 7.** *Signals generated when a high-energy beam of electrons interacts with matter*

#### Scanning electron microscopy (SEM)

In a Scanning Electron Microscope, images are acquired by scanning the sample surface with a finely focused electron beam. As shown in Fig. 7, in this configuration, the signals produced from the electron-matter interaction are: secondary electrons (SE, used to produce surface images), backscattered electrons (BSE, used for images with atomic number contrast), Auger electrons (AE, used to study the chemical composition of the material), X-rays (used for elemental analysis) and photons of visible light (used to study the composition, growth and quality of the material).

In this thesis, top view and cross-sectional SEM images were taken to analyze the morphology and thickness of the studied coating. SEM measurements were performed by using a FEI Helios Nanolab 600i Dual Beam microscope. This instrument is also equipped with a focused ion beam (FIB).

#### Transmission electron microscopy (TEM)

Microscopic analysis is completed with transmission electron microscopy (TEM) measurements. In TEM, a beam of electrons is transmitted through an ultra-thin specimen (thickness ≤ 100 nm), which interacts with matter as it passes through it. Elastic and inelastic collisions of electrons with the atoms of the specimen result in the electron beam being transmitted and scattered at different angles as illustrated in Fig. 7.

When the electrons selected for the analysis are the elastically scattered ones, typically four different imaging modes can be defined: (i) bright-field, (ii) dark-field, (iii) high-resolution and (iv) diffraction, depending on the selected electron beams exiting the sample. As shown in Fig. 8, to operate the microscope in the bright field (BF) or dark field (DF) imaging mode, an aperture located in the back focal plane is positioned such that it allows either transmitted or diffracted electron beams to contribute to the image. If the beam is directly transmitted, a BF image is obtained, whereas a dark field (DF) image is formed when the aperture is positioned to select just one of the diffracted beams. In high-resolution TEM (HRTEM), the image is the result of the interference of more than one diffracted beam. It is used for detailed structural analysis since it allows obtaining a direct imaging of the structure of the sample with atomic resolution. In the diffraction operation mode, only the diffracted beams are analyzed. Under these conditions, the atoms act as a diffraction grating to the electrons, and one can insert an aperture in the first image plane below the sample, defining the area from which the diffraction pattern is to be recorded. This working mode is called selected-area electron diffraction (SAED). SAED is a very important tool to obtain information from a desired area, for example, about the presence of crystalline and/or amorphous phases, the crystallographic orientation of a single grain in a polycrystalline sample, orientation relationships between different phases, the existence of precipitates, etc.

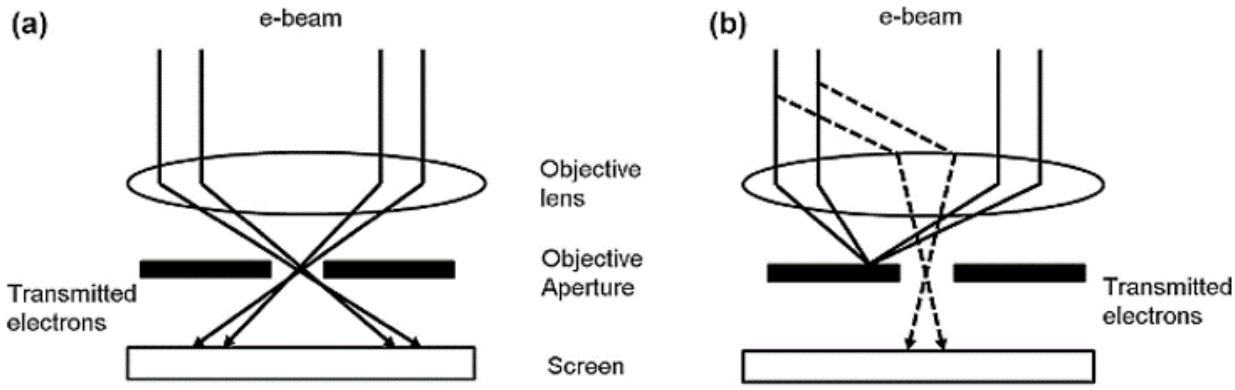


**Figure 8.** *Transmitted and diffracted electrons for (a) bright field and (b) dark field images in TEM [33]*

In this thesis, DF, BF and HRTEM were used for determining the microstructure of the different films. The selected area electron diffraction (SAED) method was employed to obtain diffraction patterns from specific sample areas in order to determine lattice parameters and crystal structures (where applicable). For SAED measurements, the area selection was made by inserting the SAED aperture in the image plane. TEM measurements were performed in a FEI Talos F200X TEM.

### Sample preparation for HRTEM and EELS analysis

Samples for TEM and EELS measurements should be thin enough (< 100 nm) to allow the electrons to pass through. In this thesis, the lift-out technique by FIB was the method used to prepare cross-sectional samples for TEM and EELS analysis. FIB is a technique that uses an ion beam for imaging, milling and metal deposition. To fabricate the cross-section of the sample to be analyzed, a protective layer of Pt was first deposited on the surface of the chosen area of the sample by a gas injection device (GIS). Ga+ ions were then used to mill trenches on both sides of the selected area to make a thin wall (≈ 1 μm) that can be cut out of the surface, lifted out and attached to a Cu grid holder using Pt, as shown in Figure 9. Once in the Cu grid, the sample was further thinned and polished using decreasing ion currents, until the final sample thickness was less than 100 nm in order to be electron transparent.

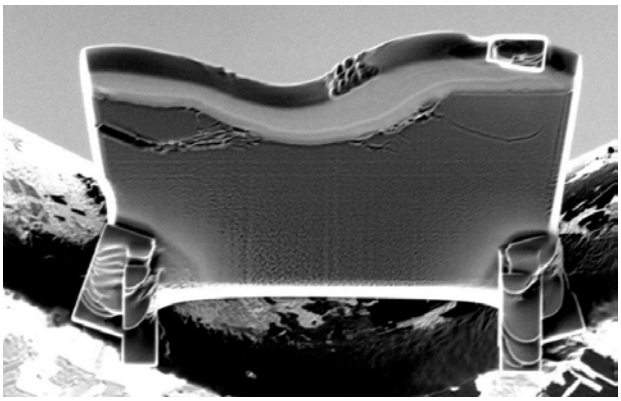

**Figure 9.** *Micrograph of a cross-section sample with a protective Pt layer before the final thinning steps to achieve electron transparency. The deformation and cracks observed in the lamella are the result of multiple impact testing.*

**Electron energy loss spectroscopy (EELS)**

This technique is performed inside a TEM instrument, where the electrons pass through a thin lamella obtained from the sample, suffering a loss of energy. The electrons selected for the analysis are the inelastically scattered ones and the energy lost by the electrons is measured by a spectrometer obtaining information about the processes that cause the energy loss. EELS works particularly well for light elements like boron, carbon, nitrogen and oxygen, since these elements exhibit sharp well-defined edges in their spectra. The energies of the edges correspond to inner shell excitations and are used for EELS analysis as they are characteristic of the elements as X-ray peaks. From this point of view, EELS is a powerful addition to EDX, because the X-rays detected in the latter are more sensitive to elements with intermediate or high atomic numbers. Besides, EELS also provides information about the chemical bonding state of a detected element because of its extremely high energy resolution.

In this thesis, EELS measurements were performed to characterize the $sp^3$ content of the studied DLC coatings. EELS measurements were carried out by using a Gatan Imaging Filter (GIF QUANTUM SE model) attached to a FEI Tecnai field emission gun scanning transmission electron microscope (STEM-FEG), mod. G2F30a with a high angle annular dark field (HAADF) detector from Fischione allowed an energy resolution of ≤ 1 eV. Figure 10 presents an EELS spectra obtained for a carbon coating, showing the typical features visible in both the low-loss and high-energy loss regions.

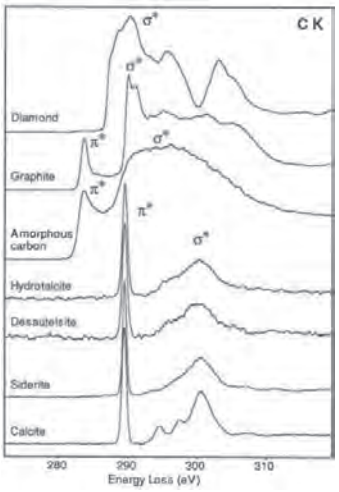


**Figure 10.** *Typical C 1s EELS absorption spectra obtained from different carbon forms*

Berger et al. [34] devised a method of analyzing EELS spectra to determine the $sp^3$ concentration of amorphous carbon films. In this method, the intensity of the π* resonance in the EELS spectra of a-C is used to measure the concentration of π bonded atoms in the films, because the absorption intensity of the electronic transitions from the C 1s core level to the π* antibonding states has been found to be proportional to the concentration of $sp^2$ bonded atoms [35]. The method consists in integrating the area under the carbon k-edge ($I_{u\pi}$) normalized to the total integral area ($I_u(\Delta E)$). The normalized ratio gives a number that is proportional to the number of π bonded electrons in that material. A graphite sample is used as a reference because $I_{ref\pi}$/ $I_{ref}(\Delta E)$ represents 100% $sp^2$ content. Therefore, the concentration of $sp^2$ bonded atoms in a carbon film can be determined from the ratio between the π* peak integral in the film to that of the reference given by:

$$sp^2 = 100\left[\frac{\left(\frac{I_{\pi^*}}{I_{\pi^*+\sigma^*}}\right)_{sample}}{\left(\frac{I_{\pi^*}}{I_{\pi^*+\sigma^*}}\right)_{100\%\ sp^2}}\right] \quad (2)$$

The used 100% $sp^2$ reference was a polycrystalline graphite sample deposited onto a holey carbon grid and the spectra were measured at magic angle conditions, at which the carbon signal would be independent of the sample orientation (TEM mode and a spectrometer collection angle of 1 mrad). The two-windows method described by S. Urbonaite [36] was used to obtain the $sp^2$ fraction. Iπ* and Iσ* were obtained by integrating the intensity over a 4 eV window (282-286 eV) and 10 eV window (288-298 eV) respectively. Several measurements were done for each sample to obtain a mean value and a correction was applied to the obtained % $sp^2$ value, to take into account the damage induced during FIB preparation which increases the $sp^2$ fraction [37].

This methodology basis was used to calculate the $sp^3$ content of DLC coatings in Chapter 5 and 6. EELS combined with TEM were also used as analytical techniques with atomic resolution to detect oxygen contamination when steel substrates were pretreated with HiPIMS metal ion etching (Chapter 3).

### 2.2.3 Atomic Force Microscope (AFM)

AFM is a type of scanning probe microscopy (SPM) technique in which a probe with a very sharp sensor tip mounted on a flexible cantilever scans the surface of the sample. The forces experienced between the atoms on the surface of the sample and those on the tip cause the deflection of the cantilever, which is monitored by using a laser beam focused on top of the cantilever. The cantilever reflects the incident light towards a photodetector. Depending on the AFM mode used (contact or tapping), a feedback signal is used to keep either the force on the sample or the oscillation amplitude of the cantilever constant. The photodetector signal and the position of the probe on the sample surface are electronically recorded to produce a three-dimensional map of the sample topography.

In this thesis, AFM was used to investigate the topography of the plasma treated samples, the etching profiles and the roughness of the coatings. AFM measurements were performed in tapping mode under ambient conditions using a Dimension Icon equipment from Bruker with super sharp Si probes (tip radius about 3 nm) by Bruker (model TESP-SS).

### 2.2.4. Raman spectroscopy

Raman spectroscopy is a common method for qualitative structural analysis [38, 39]. The method is based on measuring the changes in the energy of the incident light due to inelastic scattering from molecular or crystal vibrations. The inelastic scattering can also occur if the transition starts from an excited vibrational level (anti-Stokes scattering) in which case the energy of an incident photon is up-shifted. In both cases, the scattered light provides information about the molecular or crystal vibration modes.

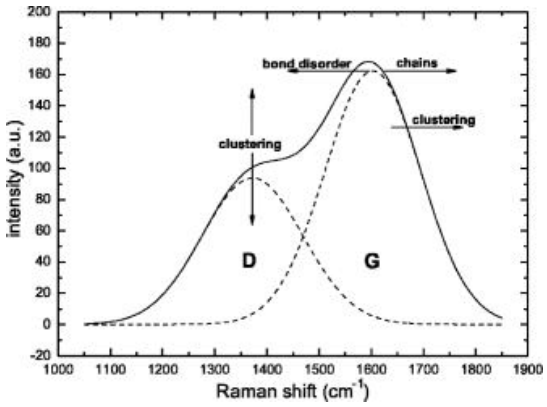


**Figure 11**. *Typical Raman spectra for an amorphous carbon material*

In a Raman spectroscopic measurement, a laser beam with wavelength in the visible, near infra-red or near ultra-violet range is used. The inelastically scattered light from the sample is collected and the scattered intensity is plotted as a function of the shift in the wavelength with respect to the wavelength of the incident laser beam. Typically, the Raman spectrum of a-C shows two broad peaks: 1) the G (graphite) peak at about 1560 $cm^{-1}$ and 2) the D (disorder) peak at about 1350 $cm^{-1}$ [40], as shown in Figure 11. The origin of the G-peak is attributed to the C-C $sp^2$ bond stretching vibrations whereas the D-peak is associated with the breathing modes of $sp^2$ bonds in a ring structure (aromatic rings). The G-peak can therefore be observed in both aromatic rings and olefinic chains, while the D-peak is observed when the ring structure is disrupted (disordered) which allows breathing vibrations in the remaining rings. The relationship between both peaks provides relevant information to infer other properties such as density, mechanical properties, etc. [41, 42].

In this thesis, Raman was used to evaluate the evolution of D and G peaks with different deposition parameters. Raman spectra were recorded using a Renishaw inVia micro-Raman spectrometer, using a 10 mW Ar ion laser working at a line of 532 nm, which was focused on the surface of the film onto a spot of approximately 1 μm in diameter. The measurement time was 10 s and spectra were accumulated 10 times in order to reduce the noise level. The region of interest (1100-1750 $cm^{-1}$) of the obtained Raman spectra, where the disordered (D-band) and graphite (G-band) modes become active for disordered carbon films, was deconvoluted using two Gaussian functions, a shape expected for a random distribution of phonon lifetimes in disordered materials [40]. A linear background was assumed due to the Raman photoluminescence (PL) effect. The relative intensity of the D and G bands ($I_D/I_G$) was obtained from the ratio of peak heights.

## 2.3. Determination of residual stresses

Residual stresses are usually observed in PVD coatings as a consequence of the high energy of impinging species during growth. The determination of residual stresses is of key importance for thin film analysis, since it provides relevant information about the growth mechanisms and the mechanical integrity of the films.

There are several methods for measuring residual stresses such as X-ray and neutron diffraction, using strain gages or photo stress coatings, and the curvature method among others.

In this thesis, we used the curvature method because it is perhaps one of the most practical methods in terms of implementation, as it is non-destructive and involves simple tool usage and post-measurement analysis. The method was introduced by Stoney and is based on measuring the deflection of the film-substrate structure [43]. The theoretical approach of this method stems from elasticity and mechanics of materials theories that relate the change of curvature in the substrate to the bending loads caused by residual stresses. The most used and simple theoretical relationship between stress and substrate curvature change is given by Stoney´s equation:

$$\sigma = \frac{E_s h_s^2}{6(1-\vartheta_s)h_f}\left(\frac{1}{R_f} - \frac{1}{R_s}\right) \quad (3)$$

where $\frac{E_s}{(1-\vartheta_s)}$ is the substrate´s biaxial elastic modulus, hs is the substrate thickness and hf is the film thickness. The main advantage of this technique is that only the elastic constants of the substrate are required for the determination of the magnitude of the residual stresses.

For residual stress determination, films were deposited onto stainless steel substrates with a thickness of 200 µm. The curvature radius was measured by a Leica DCM 3D confocal profilometer for both sides of the sample before and after film deposition, considering the whole surface of the sample. The thickness of the films was measured from cross-sectional images obtained by scanning electron microscopy (SEM) as previously described (section 2.2.2.).

## 2.4 Adhesion analysis

There are a large number of surface methods for evaluating the adhesion strength of coatings to the substrate. In this thesis, a qualitative assessment on adhesion was carried out by the Daimler-Benz Rockwell test while a quantitative assessment was performed by nano-scratch testing.

### 2.4.1 Rockwell-C indentation testing

Daimler-Benz Rockwell test is a low-cost qualitative technique commonly used in industry to verify the resistance to detachment of coatings which relies on the observation of a Rockwell C indent. The test is simple and requires less time than other techniques which makes it ideal for quality control purposes. As this method stands out for its simplicity, it was used in this thesis as a first assessment of the coating´s adhesion.

The Daimler-Benz test adhesion measurements follow the Rockwell C hardness test procedure described by the ASTM standard E18-8b [44] and are interpreted using guidelines prescribed by VDI Guideline 3198 (Figure 12) [45]. An indentation load of 150 kgf is applied to the surface. Once a steady indentation depth is reached, the applied load is removed. The indentation crater is then examined under an optical microscope and the observed damage to the coating-substrate system is graded from HF1 to HF6 using the VDI Guideline 3198. The grading provides a semi-quantitative assessment of the coating adhesion strength. There are six levels of adhesion:

**HF1:** Minor microcracking and no delamination

**HF2:** Significant microcracking and no delamination

**HF3:** Significant microcracking and minor delamination

**HF4:** Significant microcracking and delamination within the microcracked area

**HF5:** Significant microcracking and delamination extending past the microcrack region

**HF6:** Delamination around entire circumference

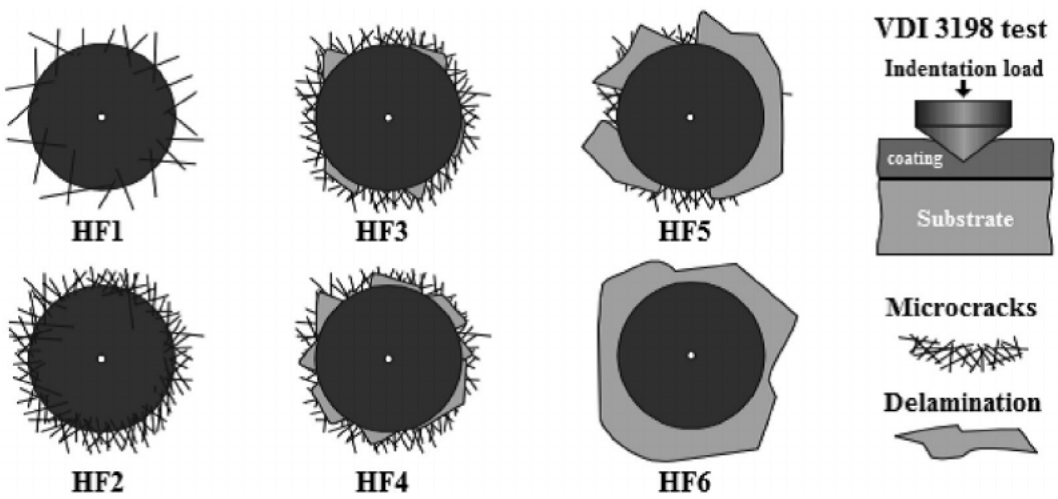


**Figure 12.** *Classification of failure modes according to the VDI Guideline 3198 for Rockwell-C adhesion test*

For most applications, adhesion results from HF1 to HF4 are deemed sufficient adhesion, while adhesion levels of HF5 and HF6 are considered insufficient adhesion.

### 2.4.2 Nano-scratch testing

Nano-scratch testing is a nanomechanical characterization method used to measure the adhesion strength and the failure modes of the studied coatings. Nanoscratching is performed by applying a controlled increasing load on a nanometric tip which travels on the sample surface for a set distance. During the test, the applied normal load, the lateral force on the tip and its lateral displacement are continuously recorded. After the test, the scratched surface is typically observed by optical or scanning electron microscopy in order to observe features of the scratch characteristic which allows obtaining information about the particular deformation and failure modes. It is a flexible method that can be easily tailored to represent different application scenarios by using various types of tips or different test kinetics with constant or ramped applied loads. There is no standard method for carrying out nano-scratch testing and therefore, the obtained results are somehow dictated by intrinsic factors (scan speed, loading rate, probe radius and geometry), and extrinsic factors (surface roughness, film stress, coatings thickness, etc.) [46].

In this thesis, nanoscratch tests were performed with a Hysitron TI 950 triboindenter using a spheroconical diamond probe with an end radius of 10 µm. Progressive load nanoscratch tests (up to a normal force of 400 mN) were carried out while simultaneously recording lateral force and penetration depth. A three-pass scratch method was used to evaluate the adhesion of DLC coatings. A schematic of the procedure is presented in Fig. 13:

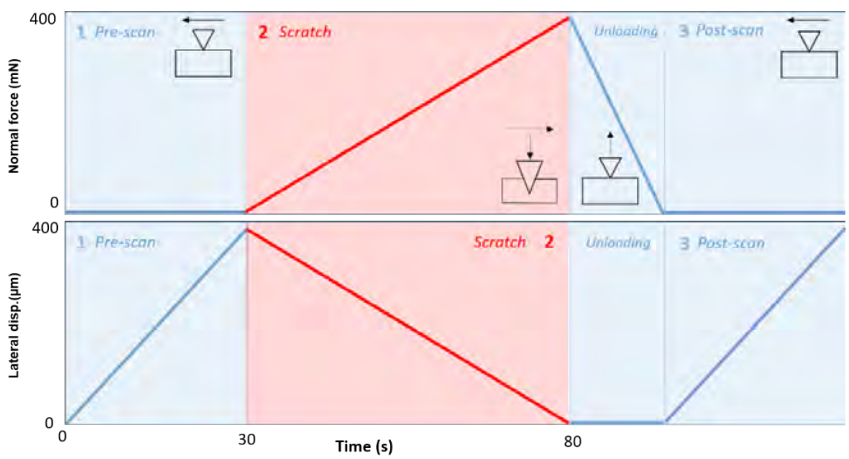


**Figure 13.** *Schematic representation of the different stages in nanoscratch testing*

The first segment (pre-scan) is used to obtain a representation of the surface topography before the scratch. In this case, the tip moves 400 µm. A low load (≈ 2 µN) is used in this segment to record a profile, so ideally, the load should be only large enough to cause elastic deformation in the surface. After this segment, a ramped force (from 0 to 400 mN in 40 seconds) is applied (red segment in Figure 13). The penetration depth data collected during loading is corrected subtracting the penetration depth collected in the initial scan. The critical load value is obtained in this segment as the load at which an abrupt decay on penetration depth and/or a sudden change in the lateral force is observed. After reaching the maximum load, an unloading step is implemented. The third stage or post-scan is finally performed to evaluate the wear of the sample after the test. SEM observation of the scratches was used to check critical load values and to distinguish the failure modes.

The failure modes were evaluated as adhesive and cohesive failure. The spallation of the coating at the interface defines an adhesive type of failure, while if the damage consists of chipping within the coating, the failure is denoted as cohesive. A mixture of both failure modes can be observed in some of the performed tests. Further analysis on the failure modes are presented in Chapter 3, where the adhesion of the deposited DLC coatings onto steel substrates under different plasma pretreatments was examined by this technique.

## 2.5. Mechanical characterization

Nanoindentation measurements were performed to analyze the mechanical properties (hardness and elastic modulus) of the produced coatings.

In a conventional nanoindentation test, a sharp tip with a well-defined geometry and very high hardness is pressed into the surface of the material while the applied load and the vertical displacement are continuously recorded. Figure 14 is an example of typical load-displacement curve where $P_{max}$ is the peak indentation load, $h_{max}$ is the displacement at peak load and $h_f$ is the final depth of the contact impression after unloading [47].

The contact area of the indentation imprints for elasto-plastic materials is usually estimated following the Oliver and Pharr's model [47] where the contact area (A) is obtained from the calibrated area function of the indenter tip, $A = f(h_c)$ which relates area to contact depth ($h_c$). In the Oliver and Pharr method, the contact depth (hc) is obtained assuming elastic unloading response, as (4)

$$h_c = h_{max} - \varepsilon \frac{P_{max}}{S} \quad (4)$$

where S is the contact stiffness, calculated from the derivate of load with respect to displacement at the maximum displacement point (the slope at the beginning of unloading curve), and ε is a factor that depends on the tip, and is equal to 0.72 for the Berkovich tip used for the tests. For non-rigid indenters, the obtained modulus is defined as reduced elastic modulus, ($E_r$) since it includes the contribution of the indenter to the measured stiffness. The reduced modulus ($E_r$) is obtained from equation (5), which relates $E_r$ with the stiffness (S) and the contact area (A). The reduced modulus ($E_r$) is obtained from equation (5), which relates $E_r$ with the stiffness (S) and the contact area (A). The Young's modulus can be obtained from equation (6), where E and υ are the Young's modulus and the Poison ration for the specimen and $E_i$ (=1140 GPa) and $\upsilon_i$ (=0.07) are the same parameters for the diamond indenter used for the tests.

Finally, the indentation hardness (H) can be determined from equation (7).

$$E_r = \frac{\sqrt{\pi}}{2 \cdot \sqrt{A}} S \quad (5)$$

$$H = \frac{P_{max}}{A} \quad (7)$$

$$\frac{1}{E_r} = \frac{(1-\vartheta^2)}{E} - \frac{(1-\vartheta_i^2)}{E_i} \quad (6)$$

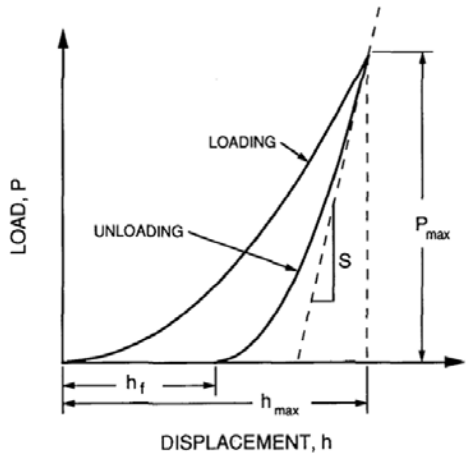


**Figure 14.** *Schematic representation of a load-displacement curve in a nanoindentation test*

In this thesis, a triboindenter TI 950 from Hysitron was used for all nanoindentation tests. It has a three-plate capacitive transducer that is used both as the actuator and sensor of the instrument. The force is electrostatically applied, while the displacement is simultaneously measured by a change in capacitance. A three-sided Berkovich pyramidal diamond tip was used as indenter. Indentations on fused silica reference sample were used to calibrate the area function of the tip $f(h_c)$. Applied testing loads were chosen such that penetration depths into the sample were kept below ≈10% of the total film thickness in order to avoid substrate effects on the measured E and H values.

### High temperature mechanical characterization

In most tribological applications, coatings are subjected to variable conditions of temperature and atmosphere. Since all mechanical properties are temperature dependent, the knowledge of the temperature dependence of the mechanical properties results essential to assess the tribological performance of coatings in real service conditions. In this sense, being able to perform nanoindentation at high temperatures is of extraordinary interest.

In this thesis, high temperature nanoindentation measurements were performed to evaluate the temperature dependence of the mechanical properties of the deposited coatings. In particular, we aim to characterize the threshold temperature at which the hardness of the coatings notably decreases. This would allow to estimate an operational range based on in-situ experimental tests instead of the estimates currently used, which are based on ex-situ measurements after annealing tests.

In this thesis, for the high temperature nanoindentation measurements, a Hysitron xSol hot stage was attached to the setup previously described for the room temperature measurements. This stage (Fig. 15) is designed to minimize the thermal drift which is one of the main issues for obtaining accurate measurements during high temperature nanoindentation.

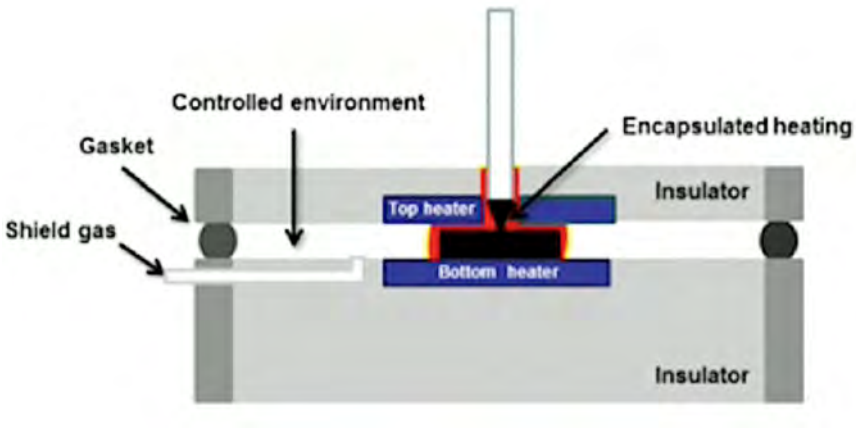


**Figure 15.** *Schematic representation of Hysitron´s xSol high temperature stage*

The thermal drift due to different mechanical and electronic response of the system caused by thermal fluctuations inside the testing chamber are counteracting by placing the sample between two resistive heating elements which heat it from top and bottom. This configuration eliminates temperature gradients through the sample thickness. Also, once the sample reached the selected temperature and before the start of the indentation test, the tip, which is attached to a special long insulating shaft, was placed at ≈ 100 μm from sample surface for 10-15 minutes to ensure passive heating of the tip and thermal equilibrium with the sample, so that thermal drift is minimized.

Dry air and argon (shield gas), were used to purge the testing area around the tip and the sample surface in order to prevent heated gases reaching the transducer and possible oxidation of the coatings. The closed design of the stage with a gasket placed between the top and bottom plates, ensures that the Ar gas must flow over the sample surface to escape.

## 2.6. Tribological characterization

The friction and wear behavior of the studied coatings were characterized by the pin-on-disk method using a tribometer. The device consists of a stationary pin that is placed under a specified load over a rotating disc (Fig. 16).

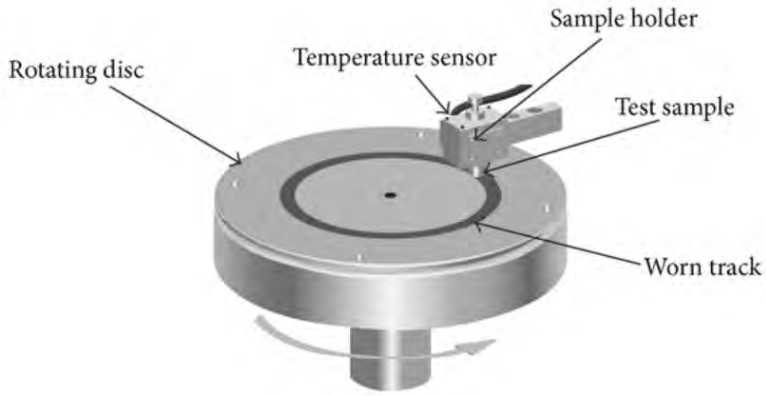


**Figure 16.** *Schematic overview of a pin-on-disc testing setup*

During a test, the pin presses down into the disc generating a circular wear track. The pin is held in position by a solid steel beam. The motion of the steel beam is translated through a linear variable differential transformer as a measurable voltage change. The software of the tribometer uses the signal obtained from the transformer and the elastic properties of the beam to determine the tangential force experienced by the pin. The coefficient of friction is then calculated with the equation 8:

$$\mu = \frac{F_T}{F_N} \qquad (8)$$

Where $F_T$ is the tangential force and $F_N$ is the applied normal force.

The wear rate is determined from the amount of lost material during the test. The wear rate can be calculated with the following expression:

$$k = \frac{V}{S \cdot F_N} \qquad (9)$$

Where k is the wear rate, V is the worn volume and S is the total sliding distance. The total length of the test can be calculated from the perimeter of the wear track multiplied by the number of cycles in the test. The worn volume is calculated by measuring the area of the wear track in cross section and multiplying it by the length of the track.

In this thesis, the tribological properties were studied to optimize the deposition conditions of a-C, a-C:H and a-C:Me coatings deposited using novel magnetron sputtering techniques. Measurements were carried out using

a pin-on-disc tribometer from Microtest MT which operates according to ASTM G99 standards [48]. Figure 15 shows a schematic picture of the testing setup. The pin used a ball bearing of alumina ($Al_2O_3$) with a diameter of 6 mm. The coatings were tested at room temperature (RT), 100, 125, 150, 175 and 200°C. The normal load was 5 N and the sliding speed was 0.1 m/s during 5000 cycles.

For the determination of the worn volume, the area of the track was measured in cross section configuration at four different locations by using high definition confocal microscopy (described in section 2.2). Moreover, to characterize the influence that the application of a frictional force has on the DLC microstructure, wear tracks were post-mortem examined by Raman spectroscopy. Further experimental details on testing conditions will be given in the chapters dedicated to tribological characterization (Chapters 5 and 6).

---

References:

[1] J.A. Thornton, Journal of Vacuum Science and Technology 15 (1978) 171

[2] J.A. Thornton, JE Green, Handbook of Deposition Technologies for Films and Applications, Ed. Noyes Publications, Park Ridge, 5 (1994) 249

[3] A.V. Phelps, Z.L. Petrovic, Plasma Sources Science Technology 8 (1999) R21-R44

[4] P.M. Martin (Ed.) Handbook of Deposition Technologies for films and coatings, 3rd edition, Elsevier Inc., Oxford (2010)

[5] J.S. Chapin, Magnetron Sputtering Apparatus, US Patent 4166018, 1979

[6] S.M. Rossnagel, Thin Solid Films 171 (1989) 125-142

[7] S.M. Rossnagel, Journal of Vaccum Science Technology A, 6 (1988) 223

[8] M. Ohring, Materials Science of Thin Films: Deposition & Structure, 2nd ed., Academic Press, San Diego, USA, (2002)

[9] S. Schiller et al., Surface and Coatings Technology 61 (1993) 331

[10] P.J. Kelly, R.D. Arnell, Vacuum 56 (2000) 159

[11] P.J. Kelly et al., Surface and Coatings Technology 174-175 (2003) 795

[12] T. Welzel, PhD thesis, Time-resolved characterization of pulsed magnetron discharges for the deposition of thin films with plasma diagnostic methods (2009)

[13] U. Helmersson et al., Thin Solid Films 513 (2006) 1-24

[14] A. Anders, J. Andersson, Journal of Applied Physics 102 (2007) 113303

[15] J. Bohlmark et al., Thin Solid Films 515 (2006) 1522-1526

[16] J. Alami et al., Thin Solid Films 515 (2007) 3434-3438

[17] K. Sarakinos et al., Surface and Coatings Technology 204 (2010) 1661-1684

[18] M. Lattemann et al., Thin Solid Films 518 (2010) 5978-5980

[19] J.T. Gudmunsson et al., Journal of Vacuum Science & Technology A, 30 (2012) 030801

[20] W. Jacob, W. Moller, Applied Physics Letters 63 (1993) 1771

[21] J. Robertson, Materials Science Engineering, 37 (2002) 129-281

[22] A. Aijaz, PhD thesis, Synthesis of Carbon-based and Metal-Oxide Thin films using High Power Impulse Magnetron Sputtering, 2014

[23] J. Filik et al., Diamond and Related Materials, 12 (2003) 974-978

[24] J. Diaz et al., Physical Review B, 54 (1996) 8064-8069

[25] J.F. Zhao et al., J. Phys. D. Appl. Phys. 37 (2004) 2416-2424

[26] L. Yate et al., Surface and Coatings Technology, 12 (2012) 2877-2883

[27] M. Mayer, Rutherford Backscattering Spectrometry, lectures given at the Workshop on Nuclear Data for Science and Technology: Materials Analysis, Trieste, 19-30 May 2003

[28] J. García López et al., Nuclear Instruments and Methods in Physics Research B, 161-163 (2000) 1137-1142

[29] M. Mayer, SIMNRA, Version 6.09, Max Planck Institut für Plasmaphysik

[30] J.R. Tesmer and M.A. Nastasi, 1995, Handbook of modern ion beam materials analysis (Materials Research Society)

[31] I.P. Chernov et al., J. Nucl. Mater. 233–237 (Part 2) (1996) 1118

[32] R. González-Arrabal et al., Nuclear Instruments and Methods in Physics Research B 270 (2012) 27–32

[33] C.Y.Tang et al., et al., Membrane Characterization 2017, 145-159

[34] D. Berger, D.R. McKenzie, P.J. Martin, Philos. Mag. Lett. 57, 285 (1988).

[35] J. Díaz, S. Anders, X. Zhou, E.J. Moler, S.A. Kellar, Z. Hussain, Phys. Rev. B

64, 125204 (2001)

[36] S. Urbonaite et al., Carbon 45 (2007) 2047-2053

[37] X. Zhang et al., Carbon 102 (2016) 198-207

[38] A.C. Ferrari et al, Phys. Rev. B, 64 (2001) 075414

[39] C. Casiraghi et al., Phys. Rev. B, 72 (2005) 085401

[40] A.C. Ferrari, J. Robertson, Phys. Rev. B 61 (2000) 14095

[41] A.C. Ferrari et al., Appl. Phys. Lett., 75 (1999) 1893

[42] V.I. Merkulov et al., Phys. Rev. Lett., 78 (1997) 4869

[43] CEN/TS 1071-11:2005: Advanced technical ceramics: Methods of test for ceramic coatings, Part 11: Determination of internal stress by the Stoney formula

[44] ASTM standard E18-8b. Standard test methods for Rockwell Hardness of metallic materials

[45] Verein Deutscher Ingenieure Normen, VDI 3198, VDI-Verlag, Düsseldorf

[46] B.D. Beake et al., Tribology-Materials, Surfaces & Interfaces,7 (2013) 87-96

[47] W.C. Oliver and G.M. Pharr, Journal of Materials Research, 7 (1992) 1564-1582

[48] ASTM Standard G99-05. Standard method for wear testing with a pin-on-disk apparatus.

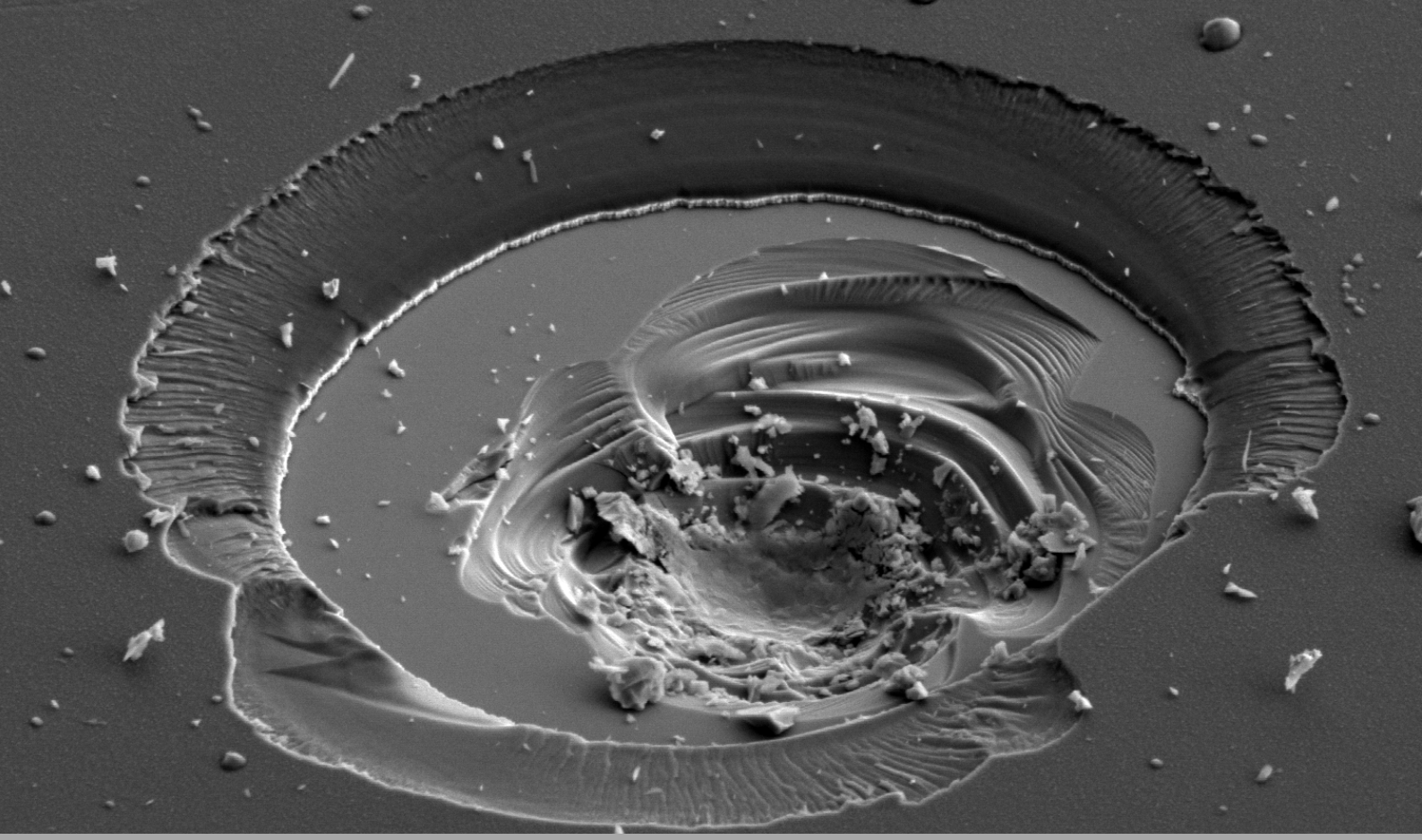

*"The greatest value among the objects of human property, not only among precious stones, is due to the diamond, for a long time known only to kings and even to very few of these." Plinio the Elder*

# Chapter 3

# Adhesion enhancement of DLC hard coatings by HiPIMS metal ion etching pretreatment

As already mentioned in the introduction, DLC coatings with improved tribomechanical properties, are deposited by highly energetic deposition techniques [1-3]. As a result of the bombardment with energetic particles, compressive residual stresses are developed in the films, which may cause mechanical damage and early delamination of coatings from the substrate.

# 1.Introduction

The lack of adhesion is a recurring problem, not only for DLC coatings, but also for most of the coatings deposited using physical vapor deposition (PVD) processes [4].

The fracture and the delamination of coatings are governed by the elastic energy stored in the coating adhered to the substrate surface. This elastic energy depends on the film thickness and the magnitude of the residual stresses in the film. Assuming that residual stresses (σ) are biaxial and isotropic in the plane of films, the elastic energy (U) stored in the film of unit surface area is given by [5]:

$$U = \left(\frac{1-\nu_f}{E_f}\right) t_f \sigma^2 \quad (1)$$

where $t_f$ is the film thickness and the term in brackets is the reciprocal biaxial modulus of the film, where $E_f$ and $v_f$ are the coating´s modulus and Poisson´s ratio respectively.

According to equation 1, the elastic energy (U) linearly rises with increasing film thickness. This available energy can be consumed to produce mechanical failure of the coating-substrate system. In particular, adhesion failure between coating and substrate occurs when the elastic energy (U) exceeds a critical value ($U_C$), which is determined by the work of adhesion ($W_d$) required to separate a unit area of an interface into two surfaces. The adhesion work is calculated according to the following equation [6]:

$$W_d = \gamma_f + \gamma_s - \gamma_i \quad (2)$$

where $\gamma_f$ and $\gamma_s$ are the surface energy of the coating and of the substrate, respectively ; and $\gamma_i$ is the energy of the coating-substrate interface. This interface energy, $\gamma_i$ has to be minimized in order to increase the work of adhesion and thus, improve the adhesion between the coating and the substrate. The interface energy depends on the chemistry, morphology and structural integrity of the interface between the coating and the substrate.

Therefore, not only the high compressive residual stresses developed when coatings are deposited using highly energetic PVD techniques are of key importance in the determination of the coating-substrate adhesion, but also the presence of contaminants at the substrate-coating interface can deteriorate the adhesion; e.g. the presence of native oxides and hydroxides at the substrate/coating interface promote weak metal-oxide bonding in comparison with metal-metal bonding, which deteriorates adhesion.

These negative effects are particularly evident when DLC is deposited onto steel substrates, and for this reason a number of techniques have been developed as pretreatment steps to improve DLC adhesion.

Traditionally, the substrate pretreatment is performed in an argon glow discharge plasma whereby contamination is sputtered away by bombardment with $Ar^+$ ions, which are accelerated towards the substrate with energies in the range of several hundred eV [7]. This method is easily implemented in industrial processes since argon is often used for subsequent sputtering deposition. However, there exist some limitations with this pretreatment, such as: (1) low sputtering yield of carbon-based contaminants with Ar; (2) implantation of $Ar^+$ ions into the substrate, which can occupy interstitial sites in the substrate lattice, thus inducing high elastic strains; and (3) diffusion and agglomeration of Ar species at the interface, which can lead to the formation of bubbles and a weaker interface. Because of that, improved adhesion values can potentially be accomplished when the substrate pre-treatment is carried out with discharges that contain highly ionized metal fluxes, such as the ones achieved by cathodic arc or high-power impulse magnetron sputtering (HiPIMS) [8].

The high-power density pulses (>1000 W/cm$^2$) produced by HiPIMS at the sputtering target, with very short selectable pulse durations (50 – 200 μs) provide higher plasma densities than standard magnetron sputtering (>$10^{19}$ m$^3$). These features meet the requirements of applications that are conventionally served by cathodic arc plasma processing such as substrate etching [9]. The metal ion etching with HiPIMS pretreatment was first reported by

Ehiasarian et al. [10] for the pretreatment of substrates prior to nitride coatings deposition; the high content of metal ions in the bombarding flux boosted the etching of the substrate surface and facilitated the formation of a metal implanted area that promoted a strong bonding between the coating and the substrate. Different metal ion etching pretreatments with HiPIMS have been reported so far using Cr [11, 12], Nb [10], Al, Ti, W [13] and WC [14] for enhancing the adhesion of hard coatings such as CrN, TiAlN, $CN_x$ or DLC to the substrate. The selection of the metal for the etching pretreatment is usually done by considering the chemical affinity of the coating-substrate system [13]. The chemical bonding strength together with the mechanical influence of the metal acting as a compliant interlayer reducing shear stresses, have been identified as the main factors dictating the level of adhesion [15].

The aim of this chapter is to improve the adhesion of DLC coatings deposited on high-speed steel (HSS) substrates using a HiPIMS metal ion etching pretreatment. The study focuses on the potential of HiPIMS to generate highly energetic Cr and Ti metallic ions in order to remove oxides from the substrate surface and promote the formation of a gradual coating-substrate interface. The influence of HiPIMS pretreatment parameters, metal ion selection, and addition of bonding layers on the adhesion properties are studied in detail. For samples with improved adhesion, the benefits of using WC/DLC multilayered structure instead of a pure WC layer in the adhesion is also investigated.

## 2. Experimental methods

Eight samples were deposited on square (20x20 $mm^2$) mirror polished high-speed steel (HSS) substrates to study the influence of the substrate pretreatment, bonding layer and multilayer on the adhesion.

The deposition system is described in further detail in the Chapter 2. A sketch of the experimental setup is shown in Fig.1.

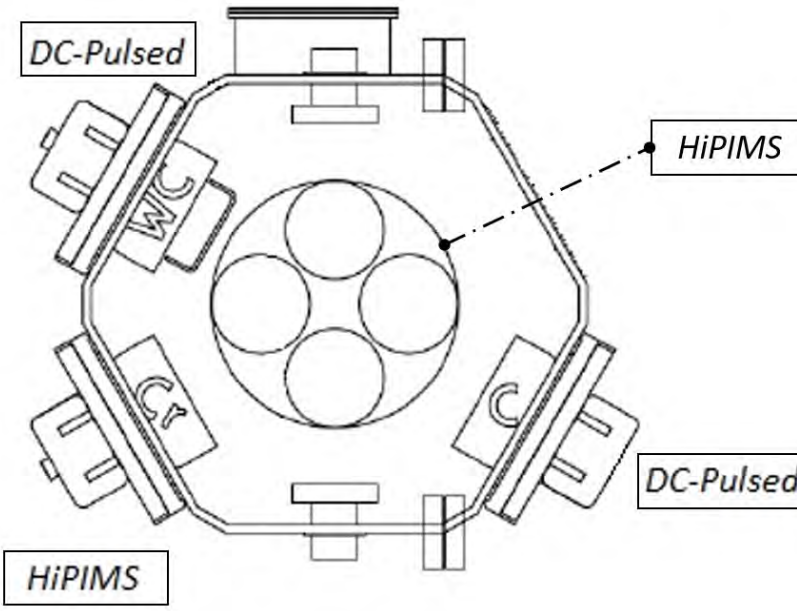


**Figure 1**. *Sketch of the experimental setup used for HiPIMS metal ion etching.*

A hip-V 6 kW HiPIMS power supply with a peak power capability of 500 A at -1200 V was connected to the target to establish the Ti and Cr HIPIMS metal discharge. A second hip-V 6 kW power supply also able to operate up to -1200 V was used to apply the negative bias voltage to the substrate. An Enerpulse EN10 DC-Pulsed power supply was used for the deposition of the DLC and WC coatings. The argon working pressure was set to 0.65 Pa and the vacuum base pressure was kept under $10^{-4}$ Pa. The substrate was placed inside the chamber at distances of 10 cm from the circular magnetron for HiPIMS metal ion etching pretreatment and 13 cm from the WC and graphite targets during coating deposition.

Prior to any pretreatment, the substrates were cleaned using a sequence of ultrasonic washing with alkaline detergents, rinsing with de-ionized water, cleaning with isopropanol and air-drying.

The parameters used for the different substrate pretreatment steps, including the deposition of the metal (Ti or Cr) bonding underlayer, of the WC/DLC maultilayer and the final deposition of the DLC coating are described in the following sequence of the complete process:

1. Ar etching: an $Ar^+$ discharge was established at the substrates for 15 minutes, using a DC-pulsed bias voltage of -500 V and a frequency of 150 kHz.

2. HiPIMS metal ion etching: the substrates that underwent this step were biased to voltages in the range from -100 to -900 V. The target was operated in HiPIMS mode with the following parameters: pulsing time of 100 µs, repetition frequency of 100 Hz and pulsing voltages of 600 V (for Ti) and 1100 V (for Cr). The measured peak currents for Ti and Cr were 85 A and 22 A respectively. The etching time was set to 5 minutes for Ti and 15 minutes for Cr.

3. Deposition of Cr/Ti bonding underlayer: the magnetron was operated at the same conditions as in the previous step, but the substrate bias was reduced to -75 V. The time of this step was adjusted after a series of calibration steps to obtain a Cr/Ti bonding layer with a thickness between 5 and 10 nm (see more details in section 3.1.).

4. Deposition of the WC interlayer: WC was deposited in DC-pulsed mode with a power density of 1.5 $W/cm^2$, a peak voltage of 1050 V, a frequency rate of 150 kHz and a pulse width of 2.7 µs. The substrate was biased at -150 V. The thickness of this layer was approximately 100 nm.

5. Deposition of WC/DLC multilayered structure: the WC target was initially operated under the same conditions as in step 4, ramping down the power from an initial 0.6 kW to 0 kW. The power delivered to the graphite target was ramped up from 0 kW to 0.7 kW. The duration of this step was 15 minutes. The substrate rotation speed was set to 1 rpm.

6. Deposition of the DLC coating: DC-pulsed mode was used for the DLC coatings deposition. The power density of the pulses reached values up to 3 $W/cm^2$ with a peak voltage of 1200 V at a repetition frequency of 150 kHz and a pulse width of 2.7 µs. A substrate bias voltage of -150 V was applied.

The sample code and the processing steps that each particular sample underwent are depicted in Table 1.

**Table 1**. *Schematic representation of the steps performed for the deposition of the studied samples.*

| Sample | Ar etching | Ti etching | Ti layer | Cr etching | Cr layer | WC layer | WC/DLC ML | DLC coating |
|---|---|---|---|---|---|---|---|---|
| **DLC/WC** | ✓ | | | | | ✓ | | ✓ |
| **DLC/WC/$Ti_{HiP}$** | ✓ | ✓ | | | | ✓ | | ✓ |
| **DLC/WC/Ti** | ✓ | | ✓ | | | ✓ | | ✓ |
| **DLC/WC/Ti/$Ti_{HiP}$** | ✓ | ✓ | ✓ | | | ✓ | | ✓ |
| **DLC/WC/$Cr_{HiP}$** | ✓ | | | ✓ | | ✓ | | ✓ |
| **DLC/WC/Cr** | ✓ | | | | ✓ | ✓ | | ✓ |
| **DLC/WC/Cr/$Cr_{HiP}$** | ✓ | ✓ | ✓ | | | ✓ | | ✓ |
| **DLC/$ML_{WC-DLC}$/Cr/$Cr_{HiP}$** | ✓ | | | ✓ | ✓ | ✓ | v | ✓ |

The evaluation of the HiPIMS parameters on the coating properties is done by analyzing both, the plasma generated during the deposition process and the voltage and the current waveforms of the pulses applied on the target. The plasma was characterized by OES. Special attention was paid to the evaluation of the ionization degree in the Ti- and Cr-HiPIMS plasma discharges.

The topography of the plasma treated samples and the etching profiles were characterized by tapping mode AFM operated under ambient conditions.

The morphological and microstructural properties of the different samples were characterized by SEM, HR-TEM and DDP. The elemental analysis at the interface was performed by EELS.

A first assessment of the adhesion strength was obtained following the Rockwell-C indentation test. As a second assessment, nanoscratch testing was used to quantitatively evaluate the adhesion strength of the DLC coatings following the procedure described in Chapter 2. Progressive load nanoscratch tests (up to a normal force of 400 mN) were carried out while simultaneously recording lateral force and penetration depth. The nano-scratch pass was carried out at a loading rate of 10 mN/s, covering a length of 400 µm. In section 3.4., the maximum normal force was extended to 500 mN, as well as the length to 500 µm. Five or more scratch tests separated by 100 µm were performed on each sample until reproducible results were obtained.

The mechanical properties of the resulting DLC coatings were measured by nanoindentation techniques. The obtained values are an average of twenty indents performed using maximum loads of 2, 7 and 12 mN with loading, holding and unloading times of 5, 2 and 5 seconds, respectively. The DLC coating residual stress was estimated using the substrate curvature method based on the Stoney equation. Further information on measurement conditions is presented in Chapter 2.

The implantation elemental profiles into the substrate and the microstructure evolution across the interface are analyzed by Electron Energy-Loss Spectroscopy (EELS) and High-resolution Transmission Electron Microscopy (HRTEM) providing an atomic level insight into the interfacial structure and chemistry.

## 3. Results and discussion

The DLC coatings studied in this chapter are classified as amorphous carbon (a-C) and they present a compressive residual stress of ~5 GPa. The hardness and the reduced Young's modulus of the coatings are 29.4 ± 2.6 GPa and 225 ± 17 GPa, respectively.

As shown in Fig. 2, the thickness of the DLC coating was ~1 µm. In this figure, the WC interlayer, with a thickness of ~200 nm, can be distinguished below the DLC coating.

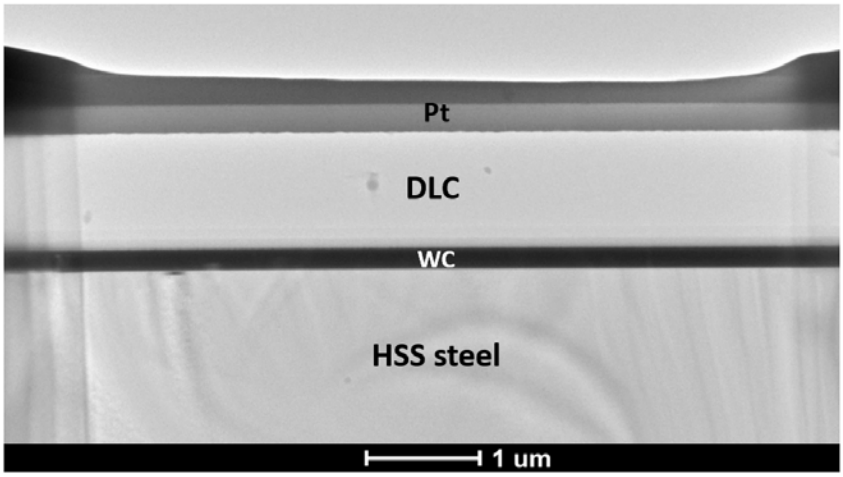


**Figure 2**. *Cross-sectional TEM micrograph of a typical DLC coatings structure. From bottom to top: HSS steel substrate, WC interlayer, DLC coating and Pt protective layer used for ion milling.*

### 3.1. Optimization of the HiPIMS metal ion etching pretreatment

As already mentioned, HiPIMS is a deposition technology currently attracting much interest as new industrial applications emerge. However, associated with its development, there is a need to establish correlations between

process parameters such as peak current, voltage and plasma duty cycle and coatings growth mode. By varying the HiPIMS parameters, it is possible to move from conditions of net deposition to metal ion etching, especially when working with highly ionized plasmas. In this case, the Ti and Cr HiPIMS discharges were operated at the highest peak current densities allowable in the low Ar pressure range, as it is well known that in HiPIMS operation mode, the ion-to-neutral ratio of the sputtered species is strongly dependent upon the peak current [16]. Very high peak current densities (up to 5 A/cm$^2$) were achieved for Ti at a target voltage of 600 V (Fig. 3a). The bias current density collected at the substrate was 150 mA/cm$^2$ at a bias voltage of -450 V. As demonstrated in previous works [17], the occurrence of high peak current densities with the Ti target might be associated with the presence of multiply charged Ti ions (up to $Ti^{+4}$) along with enhanced secondary electron emission. Therefore, only very low bias voltages might be necessary to perform efficient substrate metal etching. In the case of Cr (Fig. 3b), much lower current densities were obtained, reaching maximum values of 1 A/cm$^2$ at a voltage target of 1050 V with a bias current density of 30 mA/cm$^2$ measured when the substrate was biased at -750 V.

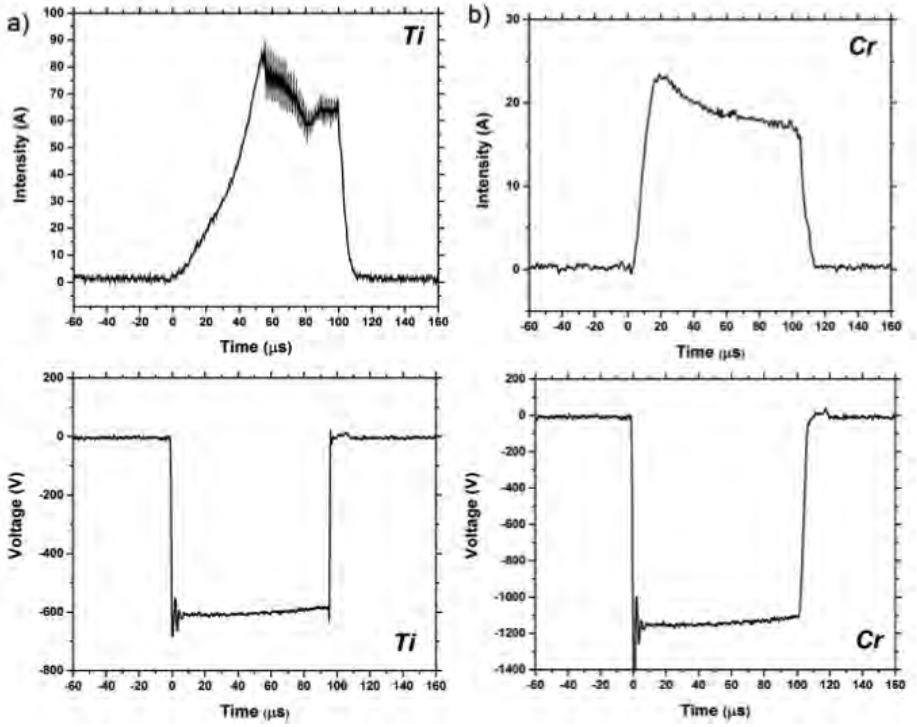


**Figure 3.** *a) Current (top) and voltage (bottom) waveform for a Ti plasma discharge during the HiPIMS metal ion etching pretreatment.*
*b) Current (top) and voltage (bottom) waveform for a Cr plasma discharge during the HiPIMS metal ion etching pretreatment.*

The higher current obtained for Ti as compared with Cr is symptomatic of a higher degree of ionization. In order to obtain information about the ionized fraction of the sputtered Ti, Cr and the sputtering gas (Ar in this case) during the sideways deposition of thin films, OES measurements were carried out; the obtained spectra are shown in Fig. 4.

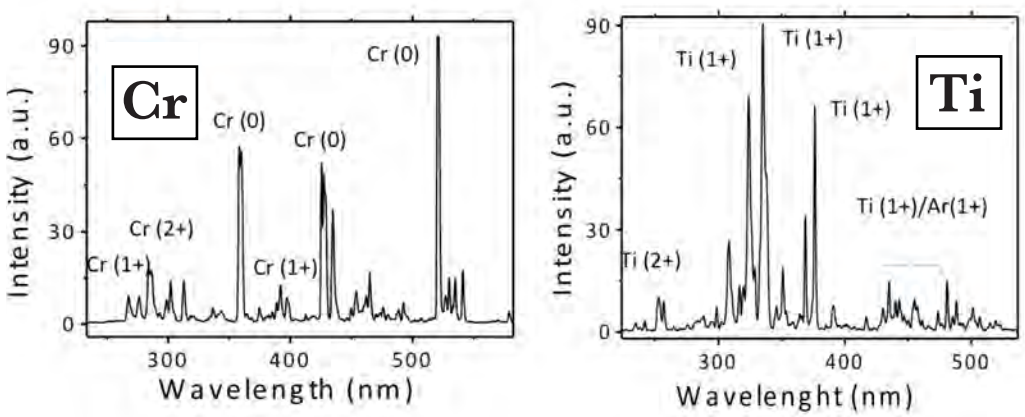


**Figure 4.** *OES spectra for Cr (left) and Ti (right) glow discharge during the HiPIMS pretreatment.*

The ion to neutral ratio is higher for Ti than for Cr. This effect results from the higher density of electrons in the Ti plasma discharges which are generated as secondary electrons emitted from the target during each pulse. Increasing the cathode voltage enhances the density and the energy of the emitted secondary electrons leading to higher ion densities with larger peak discharge currents, which facilitates metal etching conditions.

The transition from net deposition to substrate etching was measured for both Ti and Cr, as shown in Fig. 5. By using a masked stainless steel sample, the net deposition or substrate etching was evaluated as a function of substrate voltage. In the case of Ti, the substrate bias voltage threshold for ion etching is considerably lower (<400 V) than for Cr, where voltages over -750 V are required in order to reach the etching conditions. This is largely due to the higher Ti ions charge state and ion-to-neutral ratio. It is well known that the kinetic energy of the ions generated during a plasma discharge and accelerated towards a negatively-biased substrate is determined by the charge state and the substrate voltage. According to the extended zone diagram proposed by *Anders* to link growth conditions with plasma or process parameters [18], when the substrate bias voltage is increased, the sputtering yield in the substrate is enhanced and thus, the net deposition rate is reduced until effective ion etching is achieved. It is also worth mentioning that the high voltages and currents flowing to the substrate can cause undesirable arcing problems that can interrupt the normal operation of the power supplies. Therefore, proper arc management in both HiPIMS power supplies is required to achieve efficient metal etching results. In our case, this problem was solved by shutting down the voltage bias during an arc event in the magnetron to prevent etching inhomogeneities, and in the opposite case (during a substrate bias arc event) by extinguishing the plasma at the magnetron. Both power supplies were synchronized, particularly to prevent net deposition of metal during bias arc occurrence. Peak current control was carried out for arc detection in both the magnetron and substrate bias power supplies. Current limit values of 35 A for Cr, 100 A for Ti and 15 A for substrate bias were used.

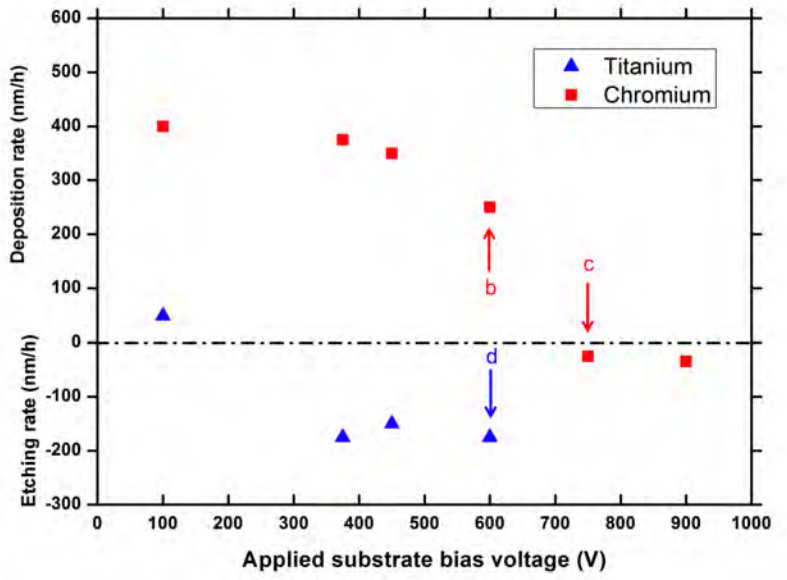


**Figure 5.** *Deposition and etching rates evaluated for Cr and Ti HiPIMS pretreatment under different applied substrate bias voltages. A transition from net deposition to etching is observed in both cases.*

Figs. 6b and c show bright field cross-sectional TEM images of the samples deposited under the conditions labeled with b and c in Fig. 5. For comparison Fig. 6a shows a TEM image of the interface of a DLC/WC sample without any HiPIMS metal etching pretreatment. Relevant differences in the sample morphology are observed for samples that underwent a HiPIMS pretreatment in comparison to those that did not. Furthermore, significant changes are also observed when pretreatment is applied depending on the substrate bias voltage. As shown in Fig. 6a, DLC/WC sample without any HiPIMS metal etching pretreatment has a low-density area between the steel and the coating (marked by an arrow), which reveals the presence of impurities that have not been removed by the $Ar^+$ etching only. The presence of these impurities leads to a poor contact between the coating and the substrate generating a weak adhesion spot. When increasing substrate bias voltage up to -600 V for Cr-HiPIMS pretreatment, the low-density area disappears and an amorphous layer with a thickness of 5 to 10 nm is observed on top of the substrate surface (Fig. 6b). The observation of similar amorphous layers when cleaning a substrate

material with HiPIMS metal ions has been previously reported [11]. It is worth noting that the extent of the amorphous layer coincides with the low-density area of impurities observed when no HiPIMS pretreatment is applied (Fig. 6a). TEM-EDX analysis (not shown) reveals that oxygen and argon are still present within this amorphous layer but at a much lower level. Over the Cr amorphous layer, a polycrystalline Cr layer is observed. The origin of the recrystallized Cr layer is still not clear. It may be due to a temperature enhancement at the layer surface related to the high ion bombardment flux, but more work needs to be done to clarify this issue.

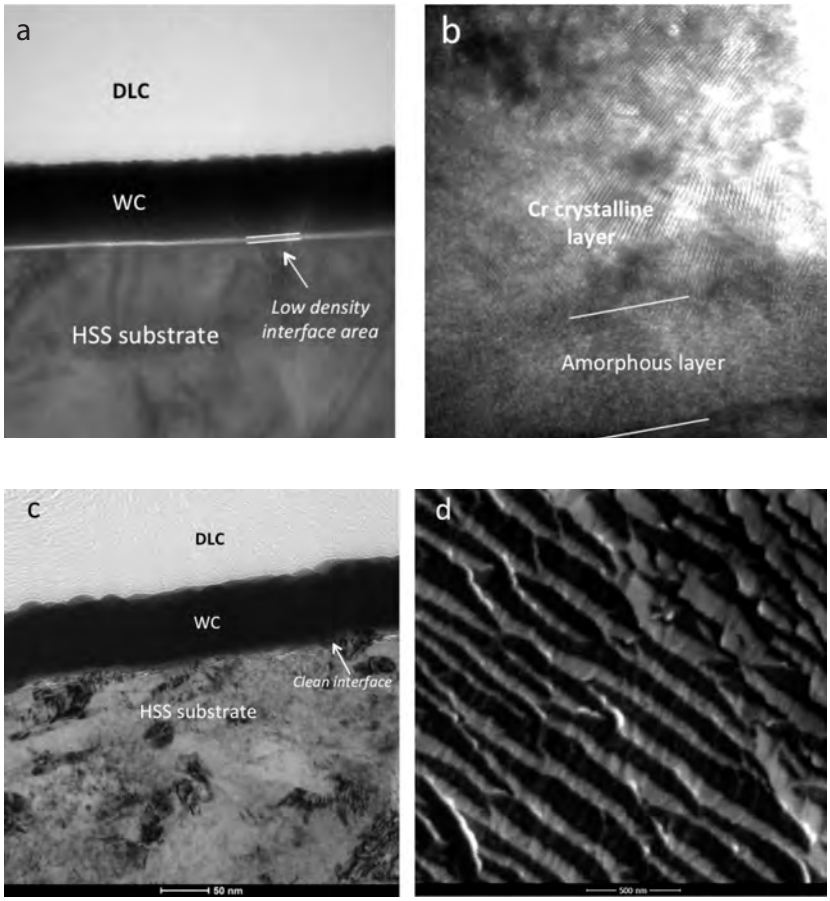


**Figure 6.** *Cross-sectional TEM images showing different coating-substrate interfaces: a) Observation of a low-density interface area for the DLC/WC sample without HiPIMS metal etching, between WC coating and HSS substrate. b) Amorphous transition layer for a Cr-HiPIMS pretreatment with -600 V substrate bias voltage under net deposition conditions. c) Clean interface with optimal coating-substrate contact observed for a sample whose substrate was pretreated with Cr-HiPIMS and biased at -750 V. d) Top-view SEM image showing the roughness induced on steel substrate surface for a sample whose substrate was pretreated with Ti-HiPIMS and biased at -600V.*

Fig. 6c shows the morphology of a sample subjected to an Ar glow discharge plus a Cr-HiPIMS ion etching pretreatment at a bias voltage of -750 V (DLC/WC/$Cr_{HiP}$). Under these process conditions, the ion kinetic energy is sufficiently high to promote effective etching over net deposition. This situation leads to a clean interface with optimal coating-substrate contact. Fig. 6d shows an SEM surface image of the steel substrate, for the case when the etching rate is too high (almost -200 nm/h), as in the sample subjected to a Ti-HiPIMS ion etching at a bias voltage of -600 V. Titanium ions reach the substrate with a high kinetic energy that leads to a significant sputter removal of the steel substrate. The high arrival energy together with the high current flux obtained during the discharge produce a rough surface (rms roughness=17.4 nm). This situation is highly undesirable from the adhesion point of view as previously reported in Ref [19].

## 3.2 Adhesion tests

Fig. 7 shows typical results from the Daimler-Benz test along with critical load values (below each image) obtained from scratch tests for all the samples studied. In order to discuss the results, we have divided the samples

into two groups: (i) samples where HiPIMS pretreatment was not applied and (ii) samples that underwent an Ar glow discharge plus an additional HiPIMS metal-ion pretreatment. Regarding the first group (columns 1 and 2 of Fig. 7) we observe that the sample without any bonding layer (DLC/WC) exhibits an adhesion strength of HF6, which is inadmissible for industrial purposes. The addition of a Ti- or Cr- bonding underlayer improves the adhesion, avoiding spallation around the indent. However, the strength quality of these samples depends on the metal selected for the bonding underlayer, being HF5 for the sample with Ti and HF1 for the sample with Cr. This difference in the strength quality is related to the extent of crack propagation, which is much larger in the sample containing Ti than in the one containing Cr.

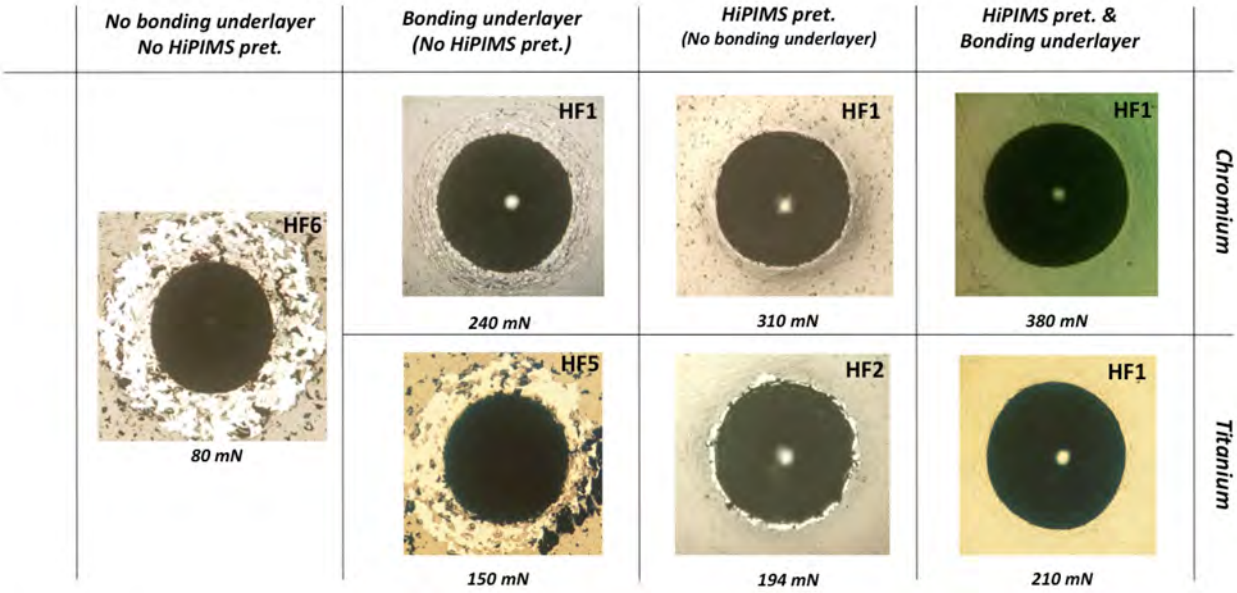


**Figure 7.** *Optical micrographs of the Rockwell indents for the different specimens of the study. The adhesion strength HF as well as the critical load values are shown in each case.*

By comparing the results obtained for both groups (see Fig. 7), it is clear that the addition of HiPIMS metal ion etching as a pretreatment step significantly contributes to enhance the adhesion. All the samples belonging to the second group show satisfactory adhesion, with a slight improvement in the Cr-HiPIMS pretreatment sample (HF1) over Ti-HiPIMS pretreatment sample (HF2). Moreover, adhesion is optimum (HF1) for both Cr and Ti, when the HiPIMS pretreatment is combined with a bonding underlayer.

Adhesion critical load values shown in Fig. 7 are consistent with the Daimler-Benz results. For coatings without any bonding underlayer and no HiPIMS pretreatment, the critical load values obtained are the lowest (80 mN). When a Ti underlayer was used, the adhesion strength is clearly improved, with critical load values reaching 150 mN. The same trend is observed when a Cr bonding layer was used, raising the critical load values from 80 to 240 mN. In order to decouple the effect of the HiPIMS pretreatment from the bonding underlayer, it is instructive to analyze the outcome of the scratch tests on the samples where the Cr- or Ti- HiPIMS ion etching pretreatments were employed without any bonding underlayers. For the titanium case, DLC/WC/$Ti_{HiP}$ reaches a critical load of 194 mN whereas for chromium, DLC/WC/$Cr_{HiP}$, the value goes up to 310 mN. Therefore, the results show that the degree of adhesion improvement is larger when using only HiPIMS pretreatment than with the use of bonding layers only. Finally, the combination of both steps (HiPIMS ion etching pretreatment followed by a metallic bonding underlayer) produces the largest improvement in adhesion. These samples exhibit critical loads that reach 210 mN in the case of Ti and 380 mN in the case of Cr. This is reasonable, as both approaches can be considered complementary. On the one hand, the HiPIMS pretreatment efficiently cleans the steel surface and provides an optimal coating-substrate contact ensuring the removal of amorphous layers that are usually developed under net deposition conditions, as shown in Fig. 6c. On the other hand, the addition of bonding layers enables the distribution of loads on larger interlayer areas relaxing stresses and reducing deformation [20-22]. Nevertheless, it is worth noting that the major difference in terms of adhesion is related to the metal that was selected for HiPIMS pretreatment. Critical load values are doubled when Cr ions are used instead of Ti ions. The adhesion strength difference is also reflected in the observation of different delamination modes.

Figs. 8a and 8b show optical micrographs and SEM images of the scratches as well as plots of normal force, lateral force and penetration displacement for the DLC/WC/Ti/$Ti_{HiP}$ and DLC/WC/Cr/$Cr_{HiP}$ respectively. When Ti pretreatment was used, a brittle delamination mode is observed (Fig. 8a) with increased hemispherical ("kidney-shaped") coating chipping failures extending over the side of the scratch track. The cracks formed along the track propagate a considerable distance before stopping in the form of a compressive spallation. Many of these cracks nucleate at large interfacial flaws such as polishing defects present in the substrate (Fig 8a). On the contrary, the delamination mode with Cr is ductile, as observed in Fig. 8b. A detailed view of the SEM image reveals a tensile buckling failure mode behind the indenter and sideward pile-up in the direction of the moving indenter. The pile-up of the material ahead and to the sides of the stylus causes the bending of the coating and controls the buckle failure mode [23], which places the coating surface in tension. The well-adherent and tough Cr underlayer forms strong bonds with the steel substrate and produces a more compliant coating-substrate system, which prevents the catastrophic adhesive failure. On the other hand, titanium undergoes a brittle failure because the compliance of the underlayer is not effective at minimizing shear stresses at the coating-substrate interface. These big differences in performance between Ti and Cr can be better understood in the light of the chemical and microstructural characterization of the interfaces, which is described in the following section.

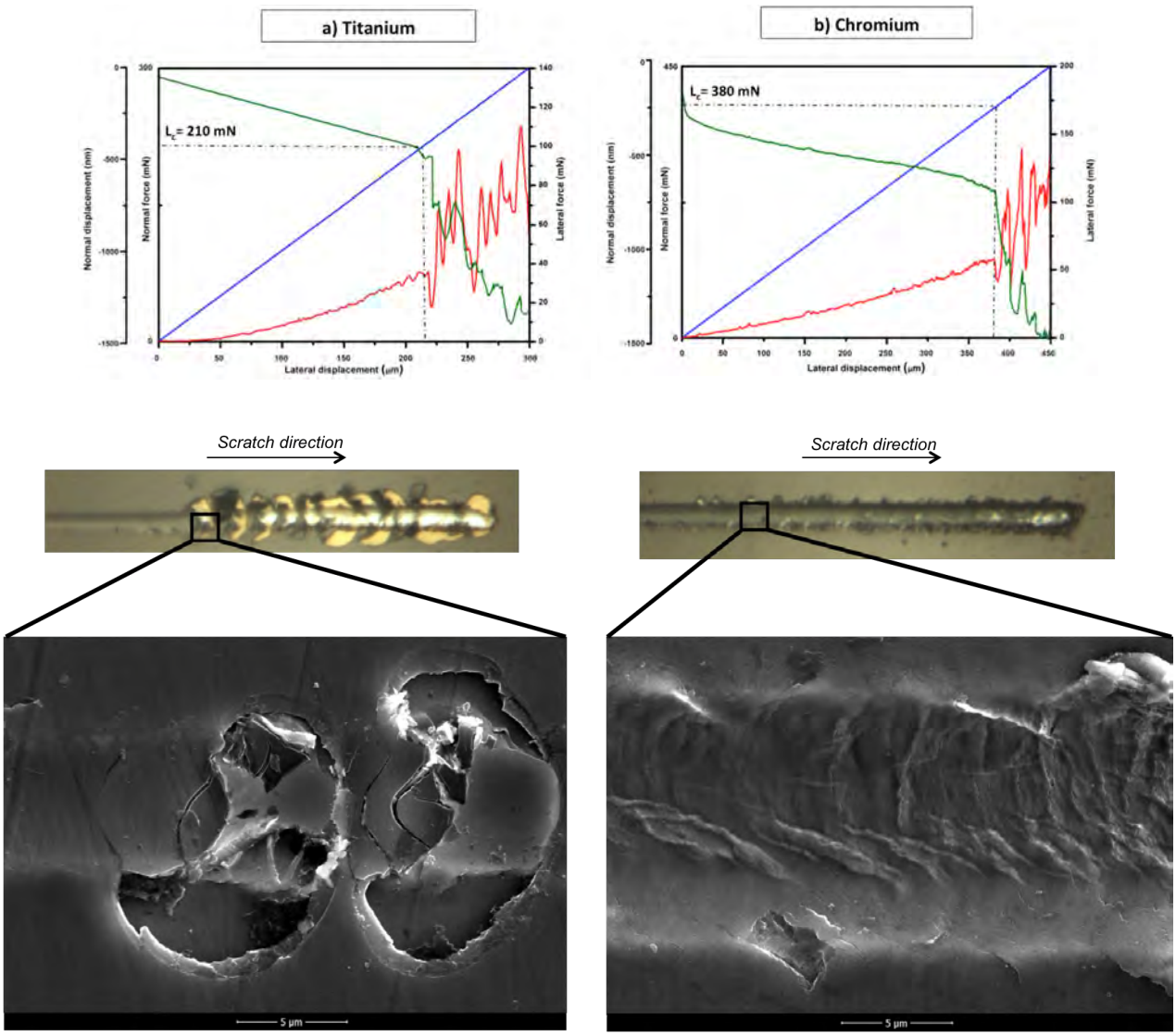


**Figure 8.** *Nanoscratch test results for DLC/WC/Ti/$Ti_{HiP}$ and DLC/WC/Cr/$Cr_{HiP}$ samples. Evolution of the normal force (blue), ateral force (red) and depth displacement (green) with the lateral displacement. Optical micrographs of the scratch tracks and SEM images of the failure mode for titanium (left) and chromium (right).*

## 3.3. Elemental distribution, morphology and microstructure of coatings exhibiting enhanced adhesion.

The elemental distribution, the morphology, and the microstructure of the DLC/WC/Ti/$Ti_{HiP}$ and DLC/WC/Cr/$Cr_{HiP}$ samples were investigated across the coating/substrate interface in order to further elucidate the role of the selected metals for HiPIMS metal-ion pretreatments on the adhesion improvement.

Fig. 9a shows the elemental distribution of the DLC/WC/Ti/$Ti_{HiP}$ sample as a function of the distance from the WC layer to the steel substrate, as characterized by EELS. The profile shows a Ti-rich region underneath the WC layer, with a thickness of ≈6 nm, where Ti content continuously increases until reaching the substrate, followed by a region of ≈6 nm where Ti is implanted into the steel substrate (shaded area in Fig. 9a). This distribution is reflected in the HRTEM image of Fig. 9b, where we can observe that the layer with lower contrast corresponds to the Ti-rich region. Ti ions have a high bonding affinity and are incorporated at lattice sites inside the steel substrate. It is worth mentioning that the distribution profile for oxygen shown in Fig. 9a follows a similar trend as the one shown for titanium, which is indicative of the formation of oxides due to the gettering effect of titanium [24, 25]. Gettering effect involves the formation of brittle oxide phases when the metal is saturated with gas [26]. The embrittlement of the titanium underlayer, due to the oxygen uptake, might not provide enough compliance to the structure, which can lead to fracture when the coating is subjected to frictional forces, as it was observed in the scratch micrographs (Fig. 8a). The gettering of oxygen can take place from native oxide films present in the surface or by the diffusion of oxygen during the titanium deposition. The Ti/O ratio remains constant along the interface, which points out to dynamic diffusion of the oxygen during coating deposition as the main gettering factor. On that assumption, the amount of oxygen incorporated into the titanium layer is linked to the residual oxygen present within the chamber. Thus, a careful control of vacuum base pressure is necessary to improve coating adhesion.

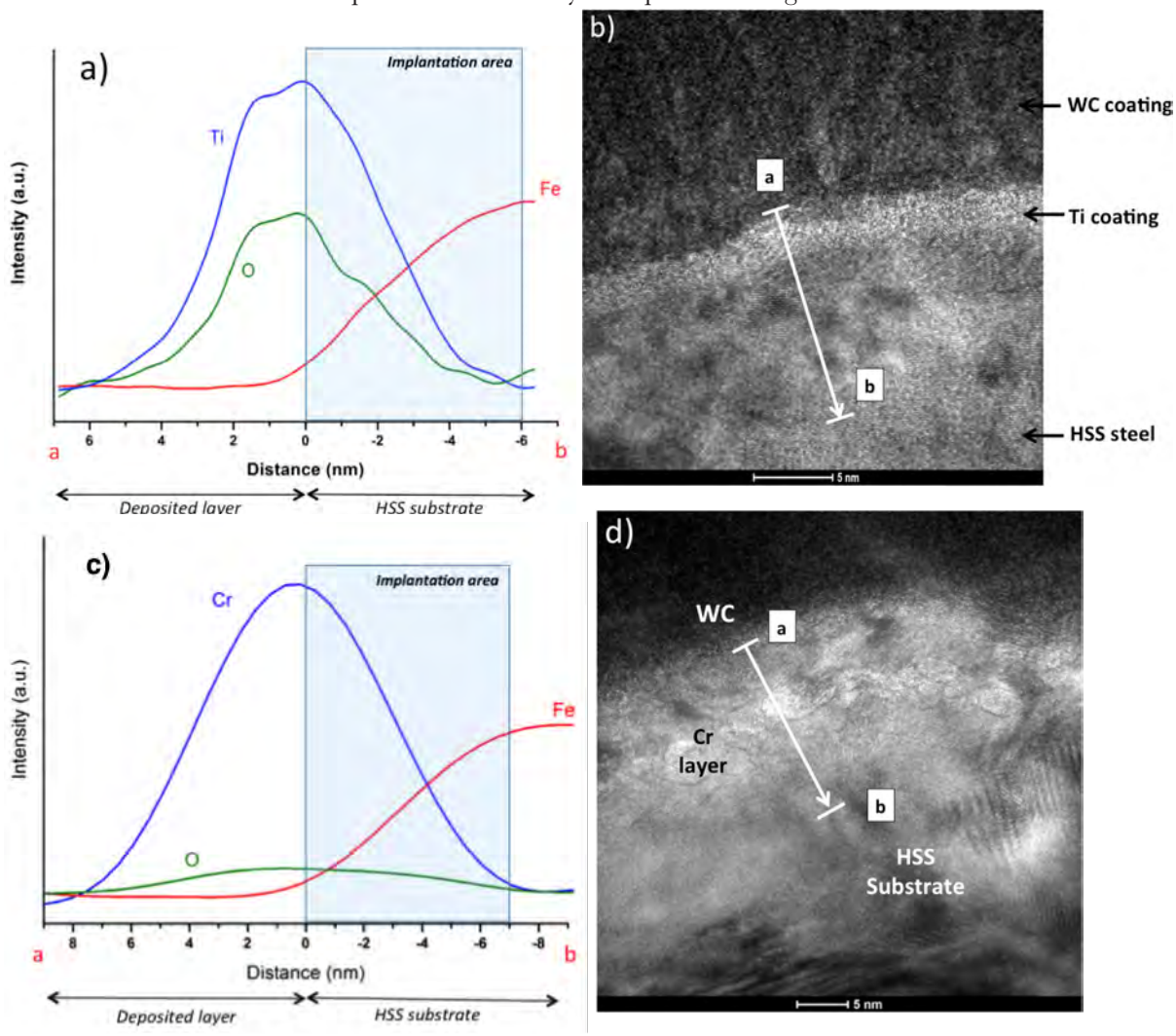


**Figure 9.** *Line-scans EELS elemental distribution analysis of the (a) Ti-HiPIMS and (c) Cr-HiPIMS pretreated interfaces and cross-sectional HRTEM images of the (b) DLC/WC/Ti/Ti-implanted/HSS steel and (d) DLC/WC/Cr/Cr-implanted/HSS steel interfaces.*

The elemental distribution of the DLC/WC/Cr/$Cr_{HiP,,}$ as characterized by EELS is depicted in Fig. 9c. The Cr signal covers a wide range of 15 nm in depth. Moving from the WC layer (left-hand side of Fig.9c) to the steel, it is found that the initial 8 nm correspond to deposited Cr. This is followed by 7 nm where the Cr signal starts decreasing and the Fe signal increases, signifying that Cr is implanted into the steel substrate. The increase in the implantation range for Cr ions is related with the higher voltage bias used for effective etching (-750) V in comparison with that used for Ti (-450 V), which provides Cr ions with higher energy. In contrast to the titanium case, the oxygen signal is negligible along the interface. As surface contamination species are kept at a very low level, metallic bonding is further promoted, which largely explains the adhesion enhancement of the Cr-ion etched samples.

From the morphological point of view, in both cases a clean and dense interface is generated as a result of the intense bombardment and highly energetic incoming flux of metal ions with no visible bubbles, voids or droplets and a wide substrate-modified area (Figs. 9b and 9d) giving rise to a more gradual DLC-steel substrate interface.

A more detailed analysis of the microstructure along different regions of the substrate-coating interface was performed by HRTEM and DDP. For each region, the sample was tilted to the zone axis of one of the substrate grains. For DLC/WC/Ti/$Ti_{HiP}$, the HRTEM image of the interface in Fig. 10a shows a fully dense nanocrystalline Ti layer. The DDP in region 1 corresponds to the [111] zone axis of the underlying fcc steel grain, with a lattice parameter, $a_{Fe(\gamma)}$ = 3.59 Å. The DDP in region 2 from the Ti underlayer suggests a hetero-epitaxial growth of the Ti layer on the steel substrate, as evidenced by the coincident DDP's from the two regions. The fact that the Ti undertakes a substantial amount of oxygen, according to the EELS analysis, introduces an uncertainty on the determination of the crystal structure of this Ti underlayer. However, the nanocrystalline nature of the Ti layer is indicative of a moderate concentration of oxygen, as higher contents have been associated with the amorphization of titanium [25, 27]. Moreover, the heteroepitaxial growth indicates an intimate bonding with the underl ying substrate.

For DLC/WC/Cr/$Cr_{HiP}$ specimens, the crystalline structure across the interface is shown in Fig. 10b. The Cr underlayer (indicated as region 1 in Fig. 10b) shows its equilibrium bcc crystal structure, with a lattice parameter, $a_{Cr}$ = 2.93 (Å). The steel grain in the substrate area (region 2 in Fig. 10b) was oriented in a [1 -1 -2] zone axis and the Cr grains in a [111] zone axis, but alignment of the diffraction patterns also suggests a heteroepitaxial relationship between the steel substrate and the Cr layer, with the {110} lattice planes of bcc Cr growing parallel to the {111} lattice planes of the fcc steel. A gradual transition from the fcc structure of the steel substrate to the bcc structure of the Cr underlayer was found as the Cr content increased across the interface, which reflects an intimate bonding between the substrate and the Cr layer.

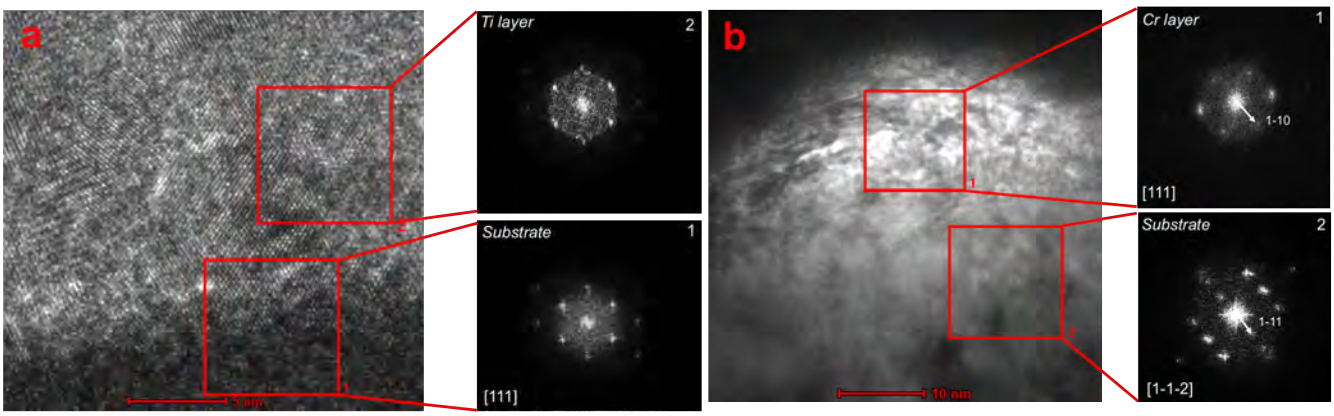


**Figure 10.** *a) Cross-sectional HRTEM images of HSS steel substrate and the subsequent titanium underlayer (bright contrast) (left). Digital diffraction patterns (DDP's) obtained from HSS steel substrate region (bottom-right, region 1) and for the Ti underlayer region (top-right, region 2) b) Cross-sectional HRTEM images of HSS steel substrate and the subsequent chromium underlayer region (bright contrast) (left). DDP's obtained from HSS steel substrate (bottom-right) and for the Cr layer region (top-right).*

Therefore, the HRTEM results confirm that the HiPIMS pretreatment alters considerably the interface structure, due to the highly energetic ion bombardment. In the case of Ti-ion etching pretreatment, a wide region of steel substrate is modified by the implantation of Ti ions and the Ti underlayers appear to grow hetero-epitaxially, indicating a clean interface free of contaminants. However, the Ti layer suffers a significant oxygen uptake, presumably from residual oxygen present within the chamber due to the getter effect of Ti. In the case of Cr pretreatment, the steel region modified by the Cr implantation is even wider, presumably due to the larger substrate bias during the Cr ion pretreatment. There is also evidence of some preferred orientation relationship of the Cr layer with the

underlying steel substrate, again suggesting a clean interface without contaminants. Even though the development of an intimate bonding between the metallic underlayer and the substrate as a result of the HiPIMS pretreatment could suggest a very good adhesion strength [12] in both cases, the resulting DLC coating adhesion was much better for chromium than for titanium. The reason for this appears to be the much higher effective removal of oxides when using Cr HiPIMS pretreatment, promoting the formation of a metallic bonding layer with optimal adhesion to the substrate, creating an interface structure that eventually fails in a much more ductile manner. On the contrary, even though the Ti seems to be as effective as Cr on removing surface contaminants, oxygen uptake due to the getter effect of Ti during deposition results in an oxygen-rich Ti bonding layer, that compromises the compliance of the interface. This assumption has been previously proposed when using titanium bonding layers [23] and agrees with the brittle deformation mode observed in the scratch tests (Fig. 8).

## 3.4 Gradual interfaces with multilayered structures for enhanced adhesion

As previously discussed, interfaces with abrupt changes in mechanical properties and chemical affinity tend to produce a poor and deficient bonding strength between the constitutive layers, leading to embrittlement. Nevertheless, if a sharp transition in the multilayer configuration is replaced by a continuous transition or graded multilayer, the bonding strength of the interfaces is usually improved. Also, there are other related benefits to the use of graded layers, such as more uniform stress distribution and reduction of thermal stresses and driving forces for crack propagation [28].

In this section, we investigate the influence in the adhesion of having a graded multilayer structure between the WC layer and the DLC coating. To do that we have selected the deposition procedure which leads to the best adhesion behavior in the previous section (DLC/WC/Cr/$Cr_{HiP}$) and we have added the WC/DLC multilayer between the WC and the DLC.

Fig. 11 shows a multilayer with a total thickness of ≈150 nm. The structure is composed of 30 layers with thicknesses ranging from 2-3 nm (DLC) and 7-8 nm (WC) to 2-3 nm (WC) and 7-8 nm (DLC) as the applied powers to graphite and WC are increased and decreased, respectively.

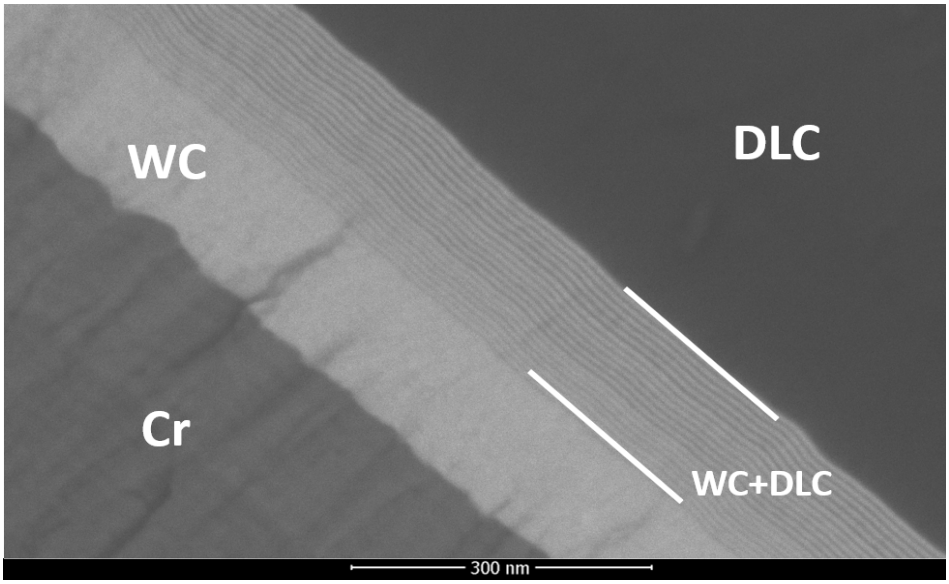


**Figure 11.** *SEM micrograph showing the multilayered structure WC+DLC between the WC layer and the DLC coating. Darker lines within the WC+DLC multilayer correspond to DLC while brighter ones correspond to WC.*

A SEM image of a scratch performed in the DLC/$ML_{WC\text{-}DLC}$/Cr/$Cr_{HiP}$ coating is shown in Fig. 12. As for the DLC/WC/Cr/$Cr_{HiP,}$ the delamination mode observed for the DLC/$ML_{WC\text{-}DLC}$/Cr/$Cr_{HiP}$ is ductile, despite some delamination spots observed along the edges of the scratch track. The deformation behavior is also very similar to the one observed for DLC/WC/Cr/$Cr_{HiP}$. However, the addition of the gradual multilayered structure increases the critical load from 380 mN to 410 mN during nanoscratch testing, which indicates that the addition of the multilayer results in an even better adhesion and provides a higher load support to the coating structure.

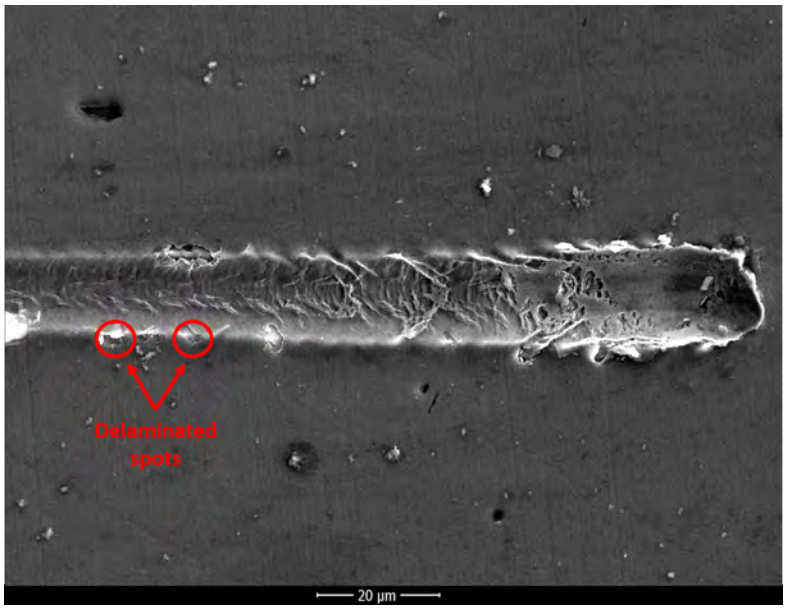


**Figure 12.** *SEM image of the track generated after nanoscracth testing the DLC/$ML_{WC\text{-}DLC}$/Cr/$Cr_{HiP}$ coating with a maximum load of 500 mN. The failure mode for this sample is ductile, as that observed for the DLC/WC/Cr/$Cr_{HiP}$.*

# 4. Conclusions

The efficiency of Ti- and Cr- HiPIMS metal ion etching pretreatment as a tool for optimizing the DLC coating adhesion on steel substrates has been demonstrated. The HiPIMS pretreatment was carried out with Ti and Cr ions under different process conditions, which were successfully optimized to obtain fully dense substrate-coating interfaces without contaminants. All samples whose substrates underwent a HiPIMS metal ion etching pretreatment exhibited superior critical load values for coating failure during scratch testing compared with pretreatments performed with just argon glow discharges or intercalation of bonding layers.

The major reasons for the remarkable adhesion enhancement achieved by the HiPIMS pretreatment process are the effective removal of contamination and impurities such as native oxides and the ability to generate a gradual interface with metal ions. The adhesion of DLC coatings to the substrate is further improved when Cr is selected as the metal for pretreatment over Ti. This is due to the higher capability of Cr to remove oxides from the interface which facilitates the metal bonding with the steel substrate. Moreover, a more compliant interface was obtained when Cr-HiPIMS pretreatment was used, which improves the stress distribution and reduces the coating deformation under load. For further adhesion enhancement, a WC/DLC multilayered structure was deposited along the interface in between the WC layer and the DLC coating. This WC/DLC multilayered structure improves the adhesion of the DLC coatings by providing a more gradual coating architecture, while preserving the ductile failure mode.

The exceptionally high critical load values presented here are of great interest for the industrial-scale deposition of DLC hard coatings.

References

[1] J. Robertson, Mat. Sci. Eng. R. 37, 129-281 (2002)

[2] K. Sarakinos et al., Surface and Coatings Technology, 206, 2706-2710 (2012)

[3] BD. Beake et al., Surface and Coatings Technology, 284, 334-343 (2015)

[4] H. Oettel, R. Wiedemann, Surface and Coatings Technology 76-77 (1995) 265-273

[5] J.J. Prescott, Applied Elasticity, Dover, New York, 187 (1961)

[6] M. Ohring, The materials Science of Thin Films, Academic Press, N. York, 1992, p.129

[7] A. Anders, Surface and Coatings Technology 200 (2005) 1893

[8] K. Sarakinos, J. Alami, S. Konstantinidis, Surface and Coatings Technology 204 (2010) 1661-1684

[9] A. Anders, Surface and Coatings Technology 257 (2014) 308-325

[10] A.P. Ehiasarian, J.G. Wen, I. Petrov, J. Appl. Phys. 101 (2007) 054301

[11] E. Broitman, Zs. Czigany, G. Grecynski, J. Bohlmark, R. Cremer, L. Hultman, Surface and Coatings Technology 204 (2010) 3349-3357

[12] M. Latterman, A.P. Ehiasarian, J. Bohlmark, P.A.O. Persoon, U. Helmersson, Surface and Coatings Technology 200 (2006) 6495-6499

[13] K. Bakoglidis, S. Schmidt, G. Greczynski, L. Hultamn, Surface and Coatings Technology 302 (2016) 454-462

[14] WD. Munz, M. Schenkel, S. Kunkel, J. Paulitsch, K. Bewilogua, J. Phys: Conf. Ser. 100 (2008) 082001

[15] D. Galvan, Y.T. Pei, J.Th.M. De Hosson, Acta Materialia 53 (2005) 3925-3934

[16] A. Anders, Appl. Phys. Lett. 92 (2008) 201501

[17] J. Andersson, A.P. Ehiasarian, A. Anders, Appl. Phys. Lett. 93 (2008) 071504

[18] A. Anders, Thin Solid Films 518 (2010) 4087-4090

[19] J. Takadoum, H. Houmid Bennani, Surface and Coatings Technology 96 (1997) 272-282

[20] A. Grill, B. Meyerson, V. Patel, Journal of Materials Research 3 (1988) 214-217 [21] H. Ronkainen, J. Vihersalo, S. Varjus, R. Ziiacus, U. Ehrnsten, P. Nenonen, Surface and Coatings Technology 90 (1997) 190-196

[22] C. Dumkum, D.M. Grant, I.R. McColl, Diamond and Related Materials 6 (1997) 802-806

[23] S.J. Bull, Surface and Coatings Technology 50 (1991) 25-32

[24] S.J. Bull, P.R. Chalker, C.F. Ayres, D.S. Rickerby, Materials Science and Engineering: A, 139 (1991) 71-78

[25] K.A. Pischow, L. Eriksson, E. Harju, A.S. Korhonen, Surface and Coatings Technology 58 (1993) 163-172

[26] V.L. Stout, M.D. Gibbons, J. Appl. Phys. 26 (1955) 1488

[27] N. Martin, C. Rousselot, D. Rondot, F. Palmino, R. Mercier, Thin Solid Films 300 (1997) 113-121

[28] H.A. Bahr et al., Materials Science and Engineering A362 (2003) 2–16

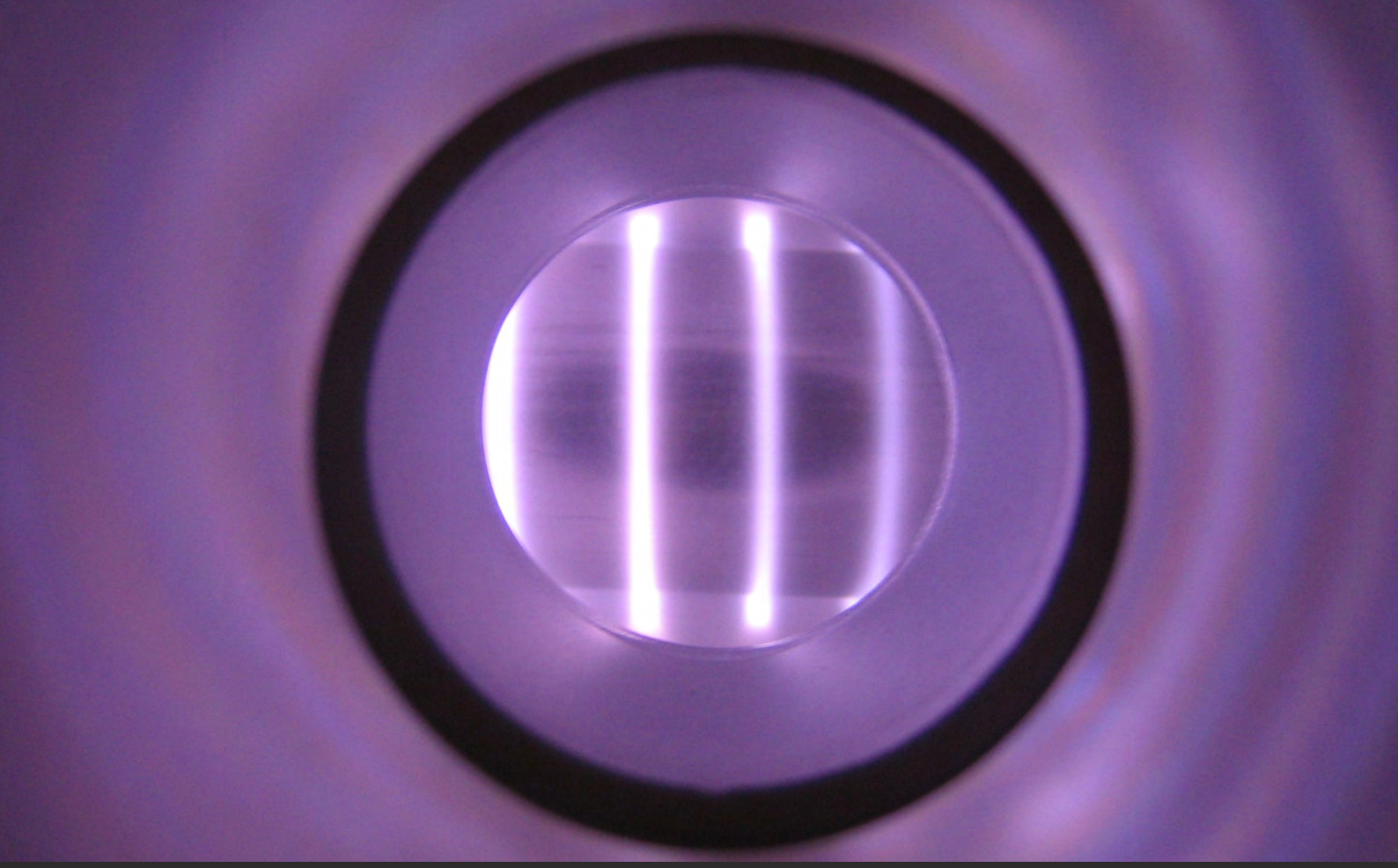

*"Diamonds are to be found only in the darkness of the earth, and truth in the darkness of the mind." Victor Hugo*

# Chapter 4

# Novel method for the deposition of hard DLC coatings by incorporating positive pulses with HiPIMS

Hard DLC coatings combine outstanding mechanical, chemical and electrical properties. Their unique mechanical properties arise from proper optimization of the $sp^3/sp^2$ bonding ratio, which can be controlled by the energy of the carbon and gas ions arriving at the surface of the growing film [1-3].

# 1. Introduction

In traditional direct current (DC) magnetron sputtering, the energy delivered into a growing DLC coating is usually insufficient to achieve a densified coating with a high $sp^3$ bonding fraction. This is due to the low ionized fraction of sputtered carbon atoms -a consequence of their low sputtering yield and high ionization potential of carbon atoms compared to other metals [4, 5]- and the low ion bombardment ($Ar^+$ and $C^+$) on the growing film. Recently, the development of high power impulse magnetron sputtering (HiPIMS) has attracted renewed attention for the deposition of hard DLC coatings [6-10], since it provides higher plasma densities than conventional DC magnetron sputtering [11]. However, in the standard HiPIMS process, the ionization probability of sputtered carbon is still insufficient to achieve optimum DLC properties [12].

In this chapter we present a HiPIMS configuration based on the concept of "plasma biasing". The basic principle of this approach is the application of short positive pulses adjacent to the negative sputtering pulses characteristics of the HiPIMS discharge, with the ultimate objective of increasing the energy, as well as the number of ions impacting on the growing coating leading to a much higher fraction of $sp^3$ content in the deposited DLC coatings.

This approach is based on previously reported asymmetric voltage polarity methods which have been used for high frequency pulsed DC discharges (up to 350kHz) in order to optimize the deposition of insulating films from conductive targets in reactive mode [13-16]. The application of a positive pulse causes the collapse of the sheath formed in front of the target during the negative pulse discharge. The voltage shift attracts electrons from the plasma preventing charge build-up on the target. Moreover, during the positive voltage pulses, ions are accelerated towards the substrate surface with energies which are proportional to the positive voltage amplitude. The plasma potential is shifted to positive values in what has been described as "plasma biasing" [17]. High-energy ions are generated during the discharge voltage overshoot, as reported by Budtz-Jorgensen et al. [18]. This is beneficial for increasing the films density and enhancing the mechanical properties of the deposited films. A similar approach has been proven effective to obtain tetrahedral amorphous carbon (ta-C) with the pulsed cathodic arc technique without the need of application of substrate bias [19].

In this chapter, we explore the effectiveness of the plasma biasing concept with carbon HiPIMS plasma discharges. To do that we deposit DLC coatings without and with diverse positive voltage pulses and we evaluate its influence on the residual stress, microstructural and mechanical properties. The benefits and implications of the applied method are supported by energy-resolved mass spectroscopy measurements.

# 2. Experimental methods

Six DLC coatings, with thickness ranging from 800 to 1100 nm, were deposited onto square (20x20 $mm^2$) M2 mirror polished steel substrates for structural and mechanical characterization. Circular SS304 stainless steel substrates of 25 mm in diameter and a thickness of 200 µm were also used for residual stress measurements. Prior to any plasma treatment, the substrates were thoroughly cleaned following a sequence of steps consisting of ultrasonic washing with alkaline detergents, rinsing with de-ionized water, cleaning with isopropanol and air-drying.

The depositions were carried out in the sputtering system described in the Chapter 2. The vacuum base pressure was kept in the $10^{-4}$ Pa range while the argon working pressure was set to 0.5 Pa. As a pretreatment step, an argon etching was performed using a DC-pulsed bias voltage of -400 V with a frequency of 150 kHz applied to the substrates for 15 minutes. Next, a Cr bonding layer was deposited using a hip-V 6 kW HiPIMS power supply connected to the circular magnetron at pulse target voltage of -1000 V, pulse duration of 100 µs, pulse repetition frequency of 100 Hz and peak discharge current density of 1.5A/$cm^2$. The thickness of the Cr bonding layer was approximately 100 nm. This was followed by a WC:Co buffer layer deposited in DC-pulsed mode with an average power density of 1.5 W/$cm^2$, pulse target voltage of -1050 V, pulse duration of 2.7 µs and pulse repetition frequency of 150 kHz. The thickness of this layer was approximately 150 nm. Finally, the hip-V 6kW HiPIMS power supply was connected to the graphite target for the synthesis of the DLC coatings.

The deposition process was carried out in two different modes: 1) regular HiPIMS mode, using the HiPIMS power supply at average power density of 1.5 (W/cm$^2$), pulse voltage of -1020 V, pulse duration of 45 µs, and pulse repetition frequency of 250 Hz. This mode implies that no positive voltage pulses were involved during shutdown of the plasma discharge; 2) new HiPIMS V+ mode, using different positive voltage pulse amplitudes or overshoot voltages or overshoot voltages applied at the end of the main negative-voltage pulse. Six different samples were studied for voltage pulse amplitudes ranging from 0 to +500 V in steps of +100 V.

For plasma characterization, optical and mass spectroscopy measurements were carried out as described in Chapter 2. The mass spectroscopy measurements could not be performed in the same chamber used for DLC coatings deposition. Therefore, a different vacuum system based on a standard DN 200 ISO-K stainless steel 6-way cross pumped by Pfeiffer Vacuum HiPace 700 turbomolecular pump (1250 l/s for $N_2$) backed up with Pfeiffer Vacuum ACP 40 multi-stage roots pump (max 37 m$^3$/hr for $N_2$) was used for this purpose. The system was equipped with a 4" magnetron (VTech, Gencoa Ltd) allowing in-situ control of the magnetic field strength over the carbon target (99.99 % purity, 6 mm thick). The base pressure before each experiment was lower than $5\times10^{-4}$ Pa. The power supply and discharge parameters (i.e., argon working pressure, pulsing time, frequency rate, average power density) were the same as those used for DLC depositions. In addition, the magnetic field of the magnetron was adjusted in order to reproduce the waveforms of the target voltage and the discharge target current density observed during DLC depositions. The waveforms were monitored by Pico Technology PicoScope 6403C digital oscilloscope, Testec TT-HV 150 voltage and Tektronix TCP303 current probes. Time-averaged energy distributions of $Ar^+$ and $C^+$ ions were measured with Hiden Analytical EQP 300 energy-resolved mass spectrometer placed at a central position above the target surface at an orifice-to-target distance of 130 mm. The mass spectrometer was grounded as it is structurally bound to the vacuum chamber. It was first tuned for maximum signal of $C^+$ ions at energies around 1 eV for which the highest number of ions were detected. The same setting was then used for all measurements of $Ar^+$ and $C^+$ ions at all energies. Since the energy range of the instrument for one scan is 200 eV, several consecutive energy scans with increasing reference (internal bias) voltage were performed. These scans were then combined to obtain the ion energy distribution functions from 0 up to 550 eV. Assuming equal sensitivity of the instrument to the various ions energies, the mean energy of ions was calculated by integrating over the ion energy distribution function.

Thickness was measured from cross-sectional images obtained by SEM. Deposition rates were calculated from the thickness measurements at a normalized power of 0.6 kW. The residual stress ($\sigma_f$) was measured using the substrate curvature method presented in Chapter 2.

The structural and mechanical properties of the DLC films were characterized by Raman spectroscopy and nanoindentation techniques, respectively. It is important to mention that the reported hardness and reduced elastic modulus values are an average of twenty indents performed using 2, 7 and 12 mN with loading, holding and unloading times of 5, 2 and 5 seconds, respectively. The maximum load was selected in order to remove undesirable substrate effects, as described in 2.5.

# 3. Results and discussion

## 3.1 Plasma properties

Fig. 1 shows the evolution of the target voltage and current waveforms as a function of time for the different positive voltage pulses configurations used during deposition.

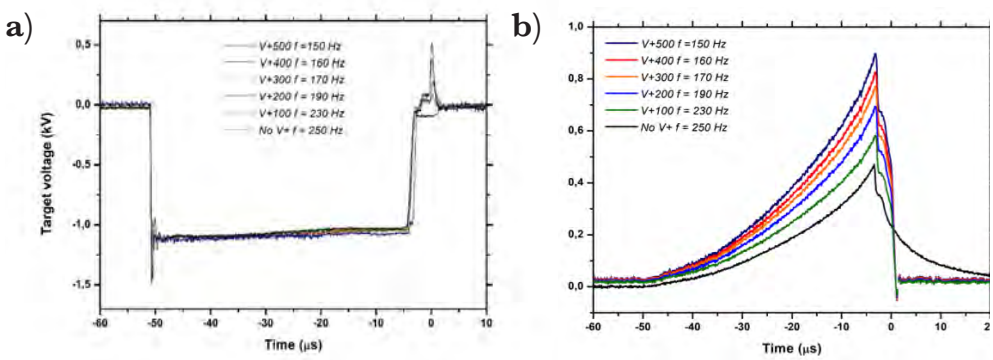


**Figure 1**. *a) Waveforms of target voltage and current density. b) Evolution of the current density and voltage waveforms during the positive voltage pulse application.*

A process without positive pulse is also shown for comparison. In all cases, both the pulse time duration as well as the average power density were kept constant at 45 μs and 1.5 W/cm$^2$, respectively. The positive pulse is generated during the plasma shutdown by connecting an inductor in series to the power supply output. The energy accumulated by this inductor during the negative pulse is used for the generation of a positive pulse with an amplitude given by the following expression:

$$V_+ = L \bullet \frac{dI}{dt} \qquad (1)$$

where L has a value of 1.2 μH and I is the peak current value obtained before the shutdown.

In this thesis, the graphite target is operated under high current densities dominated by the so-called "gas recycling effect" [20, 21] where high current densities can be achieved in target materials with low sputter yield, such as graphite or oxidized target surfaces. By operating in this regime, it is possible to achieve strong variations of peak current values (between 200 and 400 A) with small changes in cathode voltage (-1030 to -1075 V). These changes in current peak values allow us to modulate the amplitude of the positive pulse.

Negative cathode voltages of -1020 V for no overshooting voltage, -1030 V for +100 V, -1035 V for +200 V, -1040 V for +300 V, -1045 V for +400 V and -1075 V for +500 V were used for both plasma characterization and DLC coating deposition. The pulse frequency was adjusted from 150 to 250 Hz to keep the power density constant at 1.5 W/cm$^2$ in all experiments. The target current increases with time and reaches a maximum (peak value) at the end of the pulse, following an exponential trend. Peak pulse currents of 400 A with high current densities up to 0.9 A/cm$^2$ were obtained.

After the application of the negative voltage pulse to the cathode, the magnetron voltage is switched off. The shutdown is accompanied by an initial steep drop in the discharge voltage. The cathode voltage remains zero for approximately 2 μs while the target current gradually decays. After this time, the positive pulse is triggered, causing a sudden decay of the target current density. Fig. 1b shows the difference in target current evolution for the sample deposited without and with positive pulse. When no positive pulse is applied, the target current progressively decays as the ions of the plasma stay near the target area. However, when the positive pulse is triggered, ions are driven away from the target towards the substrate. When the positive pulse is applied, the plasma potential increases as it is always a few eV higher than the most positive electrode in the plasma (which is the target during the positive pulse). Ions are accelerated towards the substrate by the instantaneous potential difference between the plasma potential and the substrate potential. As the floated substrate is charged by the incoming ions, its potential gradually increases, thus reducing the potential difference between the plasma and itself. As a consequence, the energy of ions incident onto an insulated substrate is limited by its electrical capacity which determines the time needed to charge the substrate to the new floating potential value in equilibrium with the plasma potential. The target potential ($V_t$) and the floating potential ($V_f$) of the substrate are shown together in Fig. 2a. The difference of these two potentials at the peak of the positive voltage overshoot ($V_t$-$V_f$) increases monotonously with the positive pulse, therefore, an increase in the energy of ions deposited onto the substrate is expected for higher amplitudes of positive voltage pulses even for the substrates at floating potential.

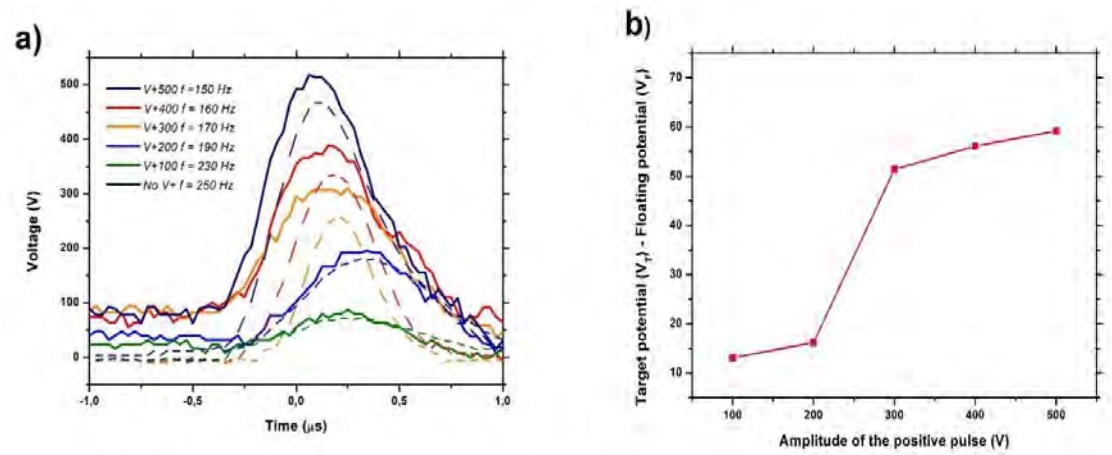


**Figure 2**. *a) Target potential (solid line) and substrate floating potential (dashed line) as a function of different positive voltage pulses. b) Evolution of the difference between target potential and substrate floating potential with positive overshoot voltages.*

Fig. 3 shows optical emission spectra (OES) for a plasma generated with and without positive pulse. In order to analyze and compare the plasma properties, spectra were normalized for the 811 nm region. In this range, neutral and ionized emission are somehow compensated, which provides a stable reference, having only notorious variations for different plasma conditions [22]. The main species observed by OES are $Ar^+$, Ar, $C^+$ and $C^{2+}$.

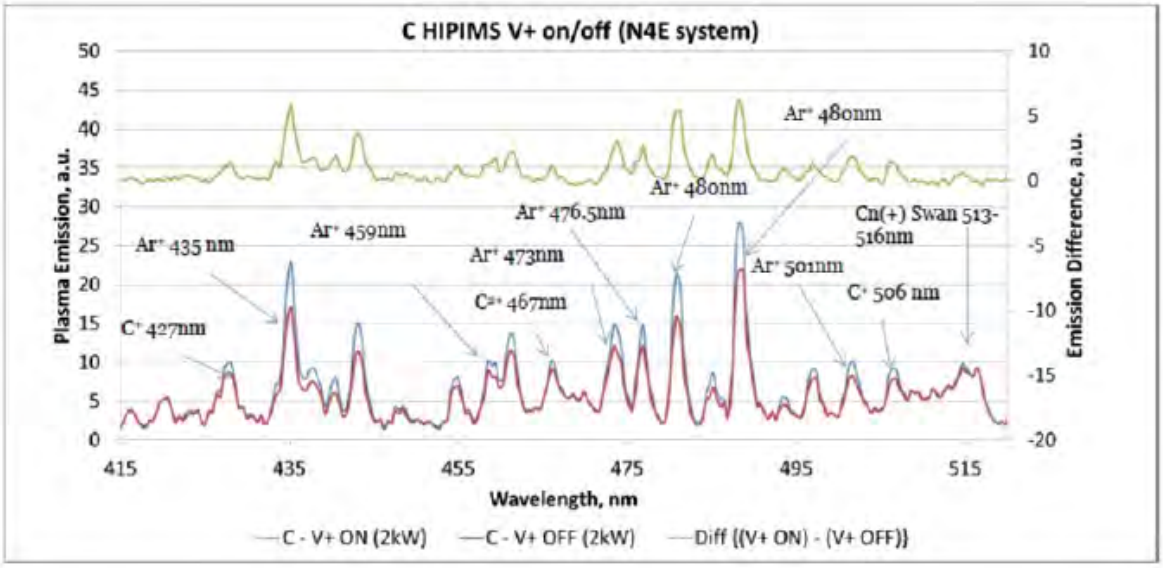


**Figure 3.** *Measured optical emission spectra (OES) for a plasma generated with (red line) and without (blue line) positive pulse and difference between both OES (green line).*

The OES obtained with and without positive pulses are quite similar. The difference lies in the intensity of the signal. In general, the intensity of the signal is larger when positive pulses are applied. Moreover, the application of positive pulses seems to have a larger influence in the Ar ions than in the C ones. A more detailed analysis of the observed differences can be assessed by using mass spectroscopy.

Analysis of a mass spectrum over masses in the range between 10 and 100 amu indicates that the dominant plasma species are $Ar^+$, $C^+$ and $Ar^{2+}$ (in order of decreasing abundance). Apart from that, small amounts of ions originating from the residual gas atmosphere ($N_2^+$, $H_2O^+$, $N^+$, $O^+$) and a trace amount of $C_2^+$ are also detected.

Fig. 4a and 4b show ion energy distribution functions (IEDF) of $Ar^+$ and $C^+$ ions measured by the grounded mass spectrometer at the substrate position for the different applied positive pulse voltages.

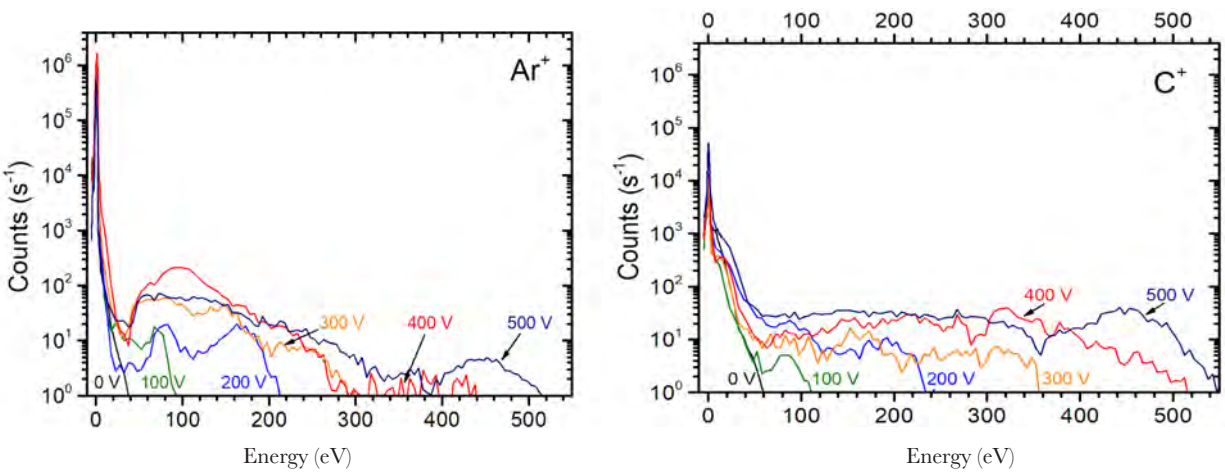


**Figure 4.** *Ion energy distribution functions of Ar+ and C+ ions measured at substrate position for positive pulse voltages of 0, 100, 200, 300, 400 and 500 V.*

In all cases, there is a dominant peak at energies of around 1 eV corresponding to the ions generated at the plasma potential with thermal kinetic energy, followed by a sharp drop in the IEDF of at least 4 orders of magnitude between 1 eV and 40 or 60 eV for $Ar^+$ and $C^+$, respectively. This trend is common for all cases. When

no positive pulses are applied (black line), no ions with energies more than 40 eV and 60 eV for $Ar^+$ and $C^+$, respectively, were detected. On the other hand, increasing amounts of $Ar^+$ and $C^+$ ions with higher energies were detected when positive pulses were applied (see Fig. 4a). This is inevitably a consequence of the positive voltage on the target causing a voltage drop between the plasma and the grounded spectrometer. As a result, ions are accelerated towards the spectrometer attaining maximum energies that correspond with the applied positive pulse voltage. The slightly higher ion energies (compared to the peak of positive voltage pulse) are caused by the fact that the peak voltage during the overshoot was slightly different in individual HiPIMS pulses as a result of the slightly different plasmas properties when the positive pulse is triggered. The relative number of high-energy ions is higher for $C^+$ than for $Ar^+$, cf. the ratio of high-energy ion counts to the peak counts at several eV.

Fig. 5 shows the normalized mean ion energies values as a function of the positive pulse voltage. The mean energy of ions detected by the grounded mass spectrometer was calculated by integrating the energy over the ion energy distribution functions (shown in Fig. 4), assuming equal sensitivity of the spectrometer for the different ion energies. The normalization was done by dividing between the values obtained for the case without any voltage overshoot.

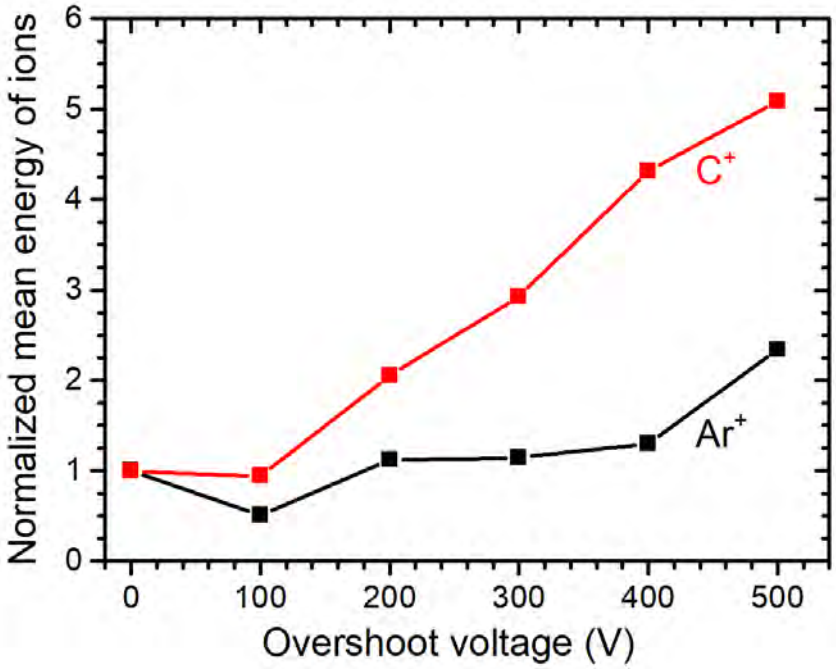


**Figure 5.** *Mean energy of ions sampled by the grounded mass spectrometer at substrate position for positive pulse voltages of 0, 100, 200, 300, 400 and 500 V normalized to the energy obtained for the regime with no overshoot (i.e. 1.0 eV for Ar+ and 4.7 eV for C+)*

As shown in Fig. 4, the mean energy of $C^+$ ions is higher than that of $Ar^+$ mainly because of the higher population of $C^+$ ions (relative to the peak) in the energy range 20 - 60 eV. Such a behavior is typical for HiPIMS discharges [23] as the C atoms are sputtered with higher energies (Thompson distribution) than those of the thermalized gas and the C atoms ionized in the dense plasma region are subject to local time-dependent electric fields which accelerate them away from the target [24]. The mean energy of $Ar^+$ ions slightly increases only for positive pulse voltages lower than 500 V, while it is about twice higher for a positive pulse voltage of 500 V. The mean energy of $C^+$ ions onto the grounded substrate significantly increases when positive pulse voltages larger than 200 V are used, reaching a value which is approximately 5 times higher for a positive pulse voltage of 500 V as compared with the case when no positive pulse voltage is applied. With respect to the film properties, it should be reminded again that the effective bias is much lower in the case of a floating potential substrate, cf. Fig. 2.

## 3.2 Residual stresses and deposition rates

A direct consequence of the higher energy observed for carbon and argons ions when a positive pulse is applied during the deposition process is an increase in the residual compressive stresses that build up on the deposited DLC films as the applied positive pulses voltage increases. Fig. 6 shows compressive stress and deposition rate values for DLC samples deposited without and with diverse positive pulse voltage applied during deposition.

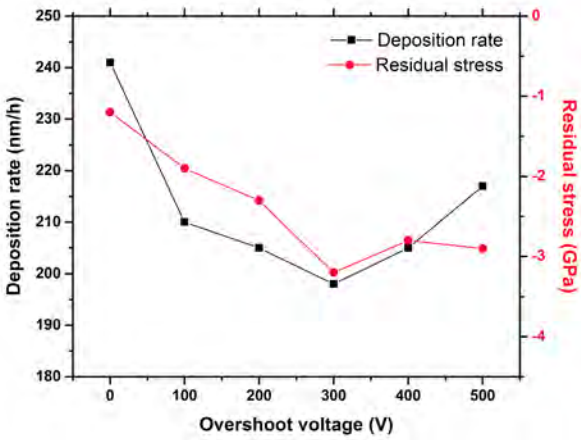


**Figure 6.** *Compressive residual stresses (a) and deposition rates (b) as a function of the applied positive pulse voltages*

As expected for samples deposited by sputtering, the residual stress measured for all studied DLC coatings is compressive [25-27]. The magnitude of the stress depends on the impact energy per atom from a discharge containing energetic argon, carbon or hydrocarbon ions, with typical energies ranging from tens to a few hundreds of eV [28]. For conventional magnetron sputtering discharges without applying substrate bias voltage, compressive residual stresses values usually remain below 2 GPa [29]. In fig. 6, we observed that the compressive stress obtained with no applied pulse voltage is ≈ 1.2 GPa. As the pulse voltage is increased, so does the energy of the ions arriving at the surface of the growing film, which develops compressive residual stresses of up to ≈ 3 GPa for pulse voltages of 300 V and over (Fig. 6).

At the same time, increasing the positive pulse voltage up to 300 V leads to lower deposition rates, which start increasing again for higher voltages (Fig. 6). There are two competing factors when using pulse voltages that may alter deposition rates. On the one hand, higher ion energies cause the densification of the coating structure which results in reduced deposition rates. On the other hand, increasing the pulse voltage leads to higher ion fluxes and consequently facilitates the ion incorporation into the growing film, thus increasing deposition rate. In this case, the densification of the structure explains the reduction of the deposition rate when ions are not very energetic (< 300V), while for higher voltage pulses, the ion flux enhancement probably plays a more important role by incorporating additional species into the coating.

Further insight into the structural evolution of the coatings with pulse voltages is obtained from Raman analysis.

## 3.3. Raman characterization

Fig. 7a shows the Raman spectra of the DLC coating with and without applied positive voltage pulses. For all samples, characteristic D and G bands of carbon were identified (by fitting of the Raman spectra using two Gaussian functions) around 1360 $cm^{-1}$ and 1540 $cm^{-1}$. All Raman spectra of the films exhibit broadening and overlapping of the two bands, indicating a disordered amorphous carbon structure [30, 31]. The D-band broadening is especially notorious in the case of the DLC coating grown without positive pulse voltage while for the DLC coatings grown with positive pulses, the G peak is well defined.

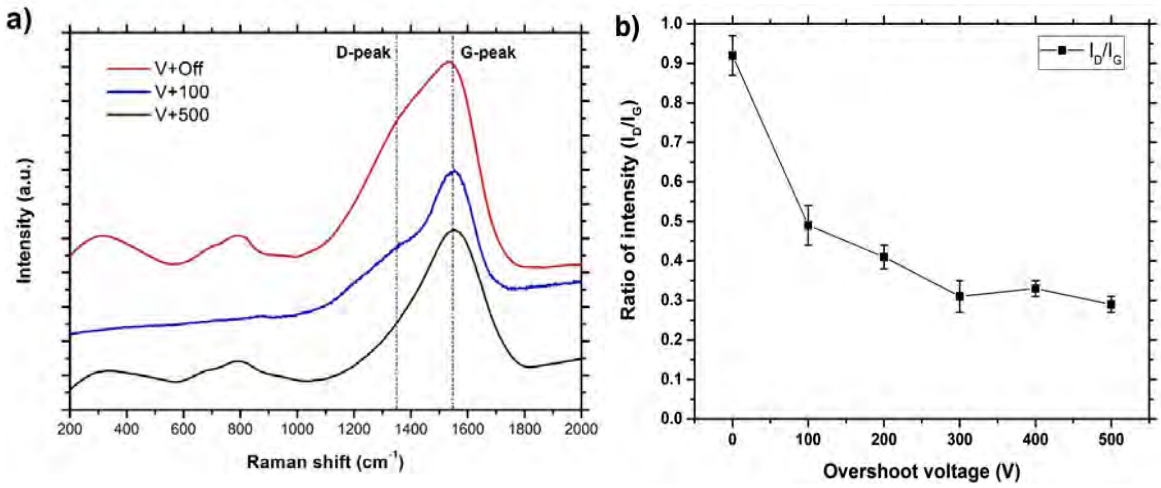


**Figure 7.** *(a) Raman spectra for DLC coatings deposited with and without positive pulses V+ and (b) evolution of $I_D/I_G$ ratio with different positive pulse voltages.*

The intensity ratio of the D and G peaks, $I_D/I_G$, as a function of applied pulse voltages is illustrated in Fig. 7b. This ratio has been widely used to qualitatively assess the $sp^3$ content and the film hardness [25]. In amorphous carbon, the ratio $I_D/I_G$ provides a measure of the size of the $sp^2$ phase organized in rings. For visible excitation (532 nm in our case), a decrease in $I_D/I_G$ ratio has been related to $sp^3$ enhancement while $sp^2$ sites change gradually from rings to chains [32]. This trend is observed when the pulse voltage is increased. For DLC coatings deposited without pulses, the ratio $I_D/I_G$ is 0.92 whereas for DLC deposited with a pulse voltage of 100 V, the ratio abruptly drops to 0.49. For higher positive voltages up to 500 V, the ratio $I_D/I_G$ progressively decays down to 0.29. As the ratio $I_D/I_G$ tends to zero, a transition from a-C to ta-C is expected to happen according to the three-stage model that predicts the amorphisation trajectory of the carbon structure from nanocrystalline graphite to diamond [33]. Therefore, on theses basis our results show that higher positive pulse voltages promote $sp^3$ bonding, facilitating the densification of the deposited DLC coatings.

## 3.4 Mechanical properties

Fig. 8a shows load-depth nanoindentation curves for DLC coatings deposited without and with different pulse voltages as measured when indentations were performed using a load of 7 mN. It is observed that the application of the positive pulse voltage during deposition has an influence both on the maximum penetration depth and on the elastic recovery of the deformed coatings. The maximum penetration depth was ≈ 190 nm for the DLC coating deposited when no pulse was applied, while penetrations under 140 nm were measured for DLCs deposited with positive pulses. Moreover, the smaller area inside the curves for higher voltage pulses indicates higher elastic recovery of the deformed coatings with less energy dissipated during deformation. No substrate effect was found at this indentation depth.

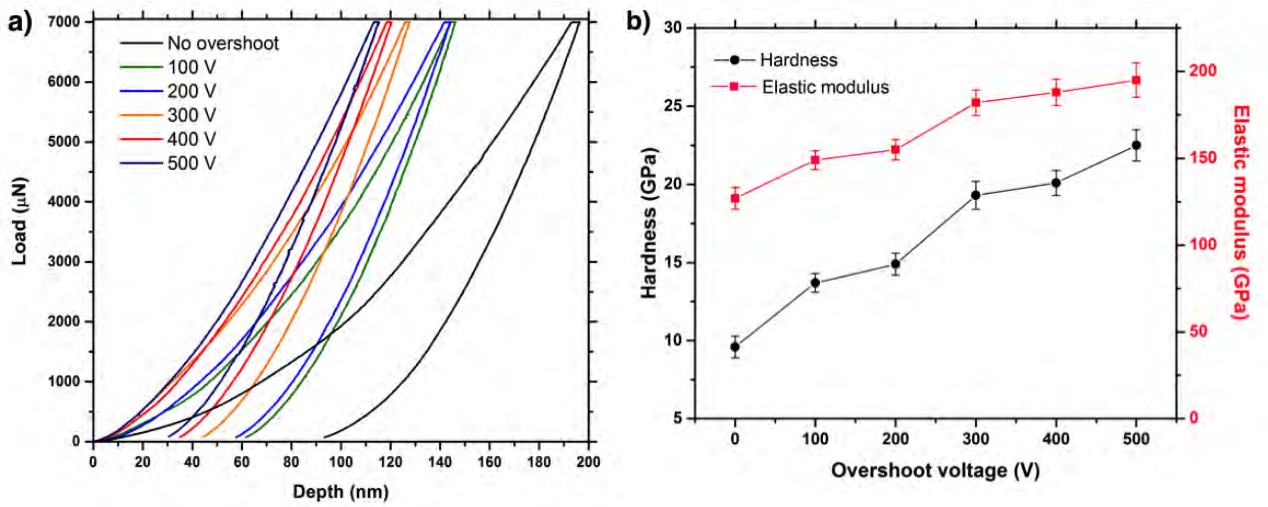


**Figure 8.** *a) Load-depth curves for DLC samples deposited without and with different pulse voltages as measured by nanoindentation. b) Evolution of hardness and elastic modulus as a function of applied pulse voltages.*

Hardness, H, and reduced elastic modulus, $E_r$, calculated from data shown in Fig. 8a following the Oliver-Pharr method, for all deposited DLC coatings are shown in Fig. 8b. An increase in both H and E is observed when the pulses voltage was increased from V+=0 V (H= 9.6 GPa; E= 124 GPa) to V+=500 V (H= 22.4 GPa; E= 192 GPa). The hardness increase for higher pulse voltages, particularly from 300 V and above, is correlated with a significant increase in the $Ar^+$ and $C^+$ ion energy. As previously described, the maximum total ion energies were increased from 40 to 520 eV when the positive pulse was increased from 0 V to 500 V (see Fig. 4b). This controlled ion energy bombardment can effectively increase adatom mobility and generate more orderly carbon structures, as observed in the Raman spectra analysis described in section 3.3. Moreover, the energy of the incoming $C^+$ ions is large enough to penetrate into the subsurface coating level [19, 34], thus increasing the density of the films and promoting the formation of $sp^3$ bonds, which is essential for optimal mechanical properties of carbon coatings [2, 30].

The ratio of hardness to elastic modulus (H/E) is valued as an important parameter for the mechanical and tribological behavior of hard coatings [35]. The H/E ratio is progressively enhanced from 0.077 with no positive pulse to 0.117 with a positive pulse of 500 V. The H/E enhancement is observed in Fig. 88a as a reduction of

the area between the loading and unloading curve and an increase of the area under the unloading curve. While the area between the loading and unloading curve represents the energy dissipated in the coating due to plastic deformation, the area under the unloading curve represents the elastic energy for deformation [36]. Therefore, the enhancement of the H/E ratio in the films with increasing intensity of the positive pulse voltage is a good indication of the improved toughness and tribological behaviour of the obtained coatings, which is of special relevance for superior abrasion resistance.

## 4. Conclusions

DLC coatings were deposited using a novel HiPIMS technique where positive pulses with different voltage amplitudes (between 100 and 500 V) are applied to a regular HiPIMS discharge right after the cathode voltage is switched off. Mass spectroscopy measurements revealed that species often difficult to ionize such as $C^+$, $Ar^{2+}$ and $C_2^+$ are present in the plasma. The IEDF analysis of the $Ar^+$ and $C^+$ indicated a substantial increase in the mean ion energy as higher positive voltages are applied. Higher pulse voltages create highly energetic growing conditions for DLCs, which is reflected in higher compressive residual stresses, reduced deposition rates and higher $sp^3/sp^2$ ratios found on the deposited DLC films.

DLCs hardness and elastic modulus are enhanced when higher pulse voltages (> 300 V) are applied. The increased presence of highly energetic $C^+$ ions is fundamental for the improvement of mechanical properties of the DLCs, which are denser and present a more ordered structure. The application of positive pulses is not only limited to carbon plasmas but can also offer great benefits for optimizing other coatings systems like hard carbides and nitrides.

References

[1] J. Robertson, Surface and Coatings Technology 50 (1992) 185-203

[2] A. C. Ferrari et al., App. Phys. Lett. 75 (1999) 1893

[3] A. C. Ferrari et al., Phys. Rev. B. 62 (2000) 11089

[4] R. Wei, Surface and Coatings Technology 204 (2010) 2869-2874

[5] N. Matsunami et al., At. Data Nucl. Data Tables 31 (1984) l–80

[6] J. Lin et al., Surface and Coatings Technology 258 (2014) 1212–1222.

[7] K. Sarakinos et al., Surface and Coatings Technology, 206 (2012) 2710–2716.

[8] M. Lattermann et al., Diamond and Related Materials 20 (2011) 68-74

[9] M. Hiratsuka et al., Surface and Coatings Technology 229 (2013) 46-49

[10] J.A. Santiago et al., Surface and Coatings Technology 349 (2018) 787-796

[11] U. Helmerson et al., Thin Solid Films 513 (2006) 1-24

[12] A. Aijaz et al., Diamond Related Materials 23 (2012) 1-4

[13] J. H. Greiner and A. Halperin, IBM Technical Disclosure Bulletin P.2173, Vol. 17 No. 7 December 1974

[14] Jeff Sellers, Surface and Coatings Technology, 98 (1998) 1245-1250

[15] E.H.A. Dekempeneer et al., Surface and Coatings Technology 120–121 (1999) 692–696

[16] M. Astrand et al., Surface and Coatings Technology 189 (2004) 186-192

[17] J.W. Bradley et al., Plasma Sources Sci. Technol. 11 (2002) 165

[18] C.V. Budtz-Jorgensen et al., Surface and Coatings Technology 137 (2001) 104-110

[19] A. Anders et al., Surface and Coatings Technology 201 (2007) 4628-4632

[20] A. Anders et al., J. Phys. D: Appl. Phys. 45 (2012) 012003

[21] J. Capek et al., J. Appl. Phys. 111 (2012) 023301

[22]

[23] J. T. Gudmundsson et al., J. Vac. Sci. Technol. A 30 (2012) 030801

[24] N. Brenning N et al., J. Phys. D: Appl. Phys. 46 (2013) 084005

[25] J. Robertson, Materials Science and Engineering: R: Reports, 37 (2002) 129-281

[26] A. Anders, Some applications of cathodic arc coatings, Springer, N. York, 2008, 1-62

[27] J. Robertson, Diamond and Related Materials, 2 (1993) 984-989

[28] A.C. Ferrari et al., Diamond and Related Materials 11 (2002) 994-999

[29] S. Zhang et al., Surface and Coatings Technology 122 (1999) 219–224

[30] J. Schwan et al., Journal of Applied Physics 80 (1996) 440

[31] J. Schwan et al., Journal of Applied Physics 79 (1996) 1416-1422

[32] A. C. Ferrari et al., Phys. Rev. B. 62 (2000) 11089

[33] A.C. Ferrari, J. Robertson, Phys. Rev. B. 64 (2001) 075414

[34] C.A. Davis, Thin Solid Films 226 (1993) 30

[35] J. Musil et al., Surface and Coatings Technology 154 (2002) 304–313

[36] Y.W. Bao et al., Acta Materialia 52 (2004) 5397–5404

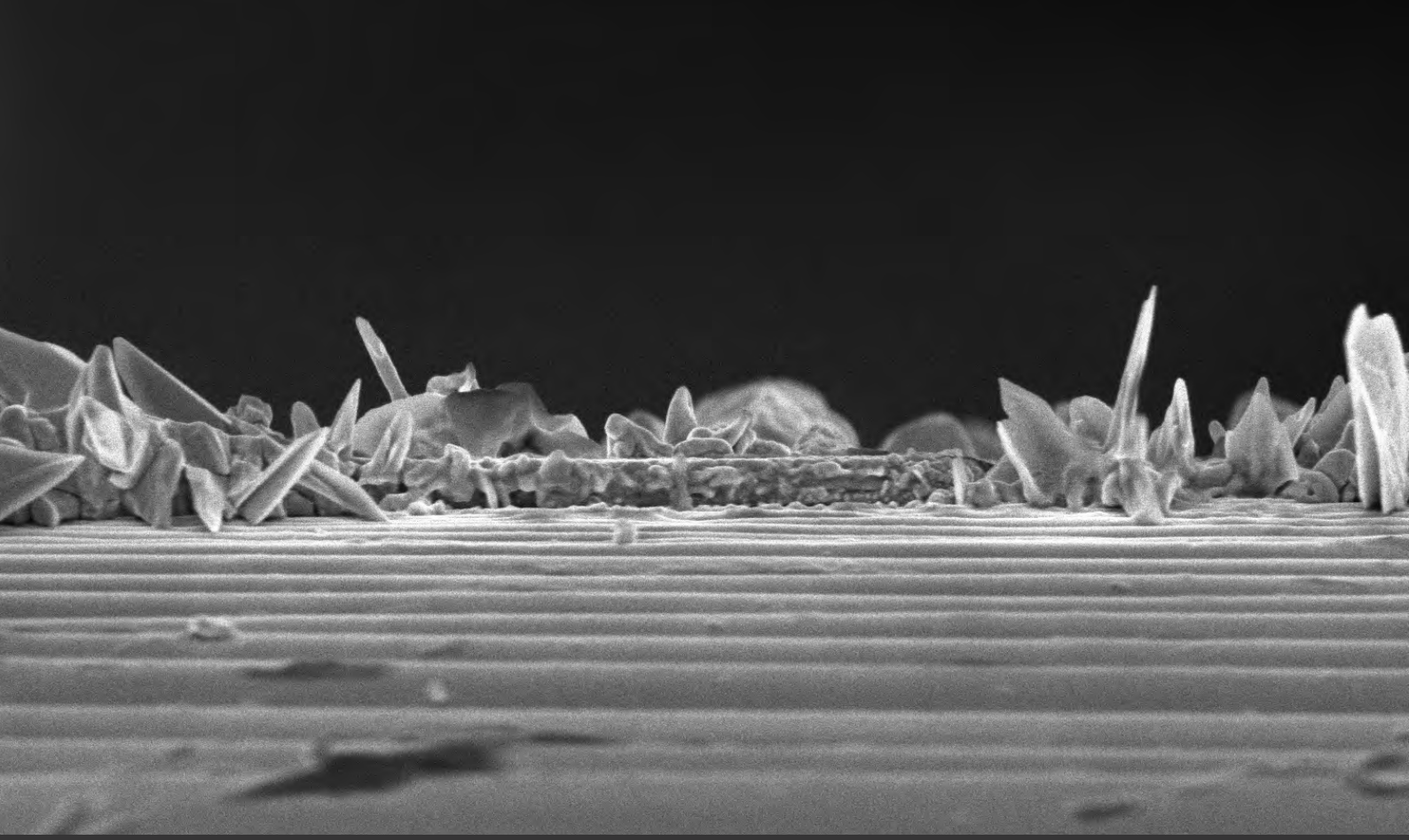

*"All is beautiful and unceasing, all is music and reason, and all, like diamond, is carbon first, then light" Jose Marti*

# Chapter 5

# Optimization of hard DLC coatings deposited by magnetron sputtering techniques

The optimization of hard DLC coatings is mainly linked to the potential increase of their C-C $sp^3$ content, as presented in Chapter 4. High fractions of $sp^3$ bonds (between 85 and 90%) can be realized in amorphous carbon films, in the so called tetrahedral amorphous carbon or ta-C, under selected deposition conditions, using Pulsed Laser Deposition (PLD), Ion Beam Deposition (IBD) or Filtered Cathodic Vacuum Arc (FCVA) [1-4]. Under more conventional conditions, the fraction of tetrahedral bonding is lower, with a corresponding decline of the diamond-like character.

# 1. Introduction

For most industrial applications, moderate levels of tetrahedral bonding are normally tolerable or even favorable because of economic reasons. Coatings with $sp^3$ contents of around 50% are acceptable, as found in tribological hard DLC coatings of industrial relevance [5].

The "subimplantation-relaxation model" introduced by Lifshitz et al.[6] described the formation of C-C bond in $sp^3$ configuration by a local densification of the C network during ion bombardment with considerable high energies between 30 eV and 100 eV [6, 7]. Magnetron sputtering techniques provide energies in the range of few tens eV, thus it becomes necessary to optimize several process parameters in order to obtain denser coatings with higher $sp^3$ contents. In this regard, we have identified some key factors inherent to the sputtering method which need to be properly considered, namely: (1) H incorporation into the film during the deposition from the residual gas in the chamber, (2) deposition temperature and (3) substrate bias voltage.

In this chapter, we investigate the influence of the sputtering mode and associated parameters on the structural and mechanical properties of DLC coatings with the ultimate goal of defining the process conditions leading to improved mechanical performance. Firstly, we study the influence of the deposition method by comparing samples deposited by sputtering in different modes: DC, HiPIMS, HiPIMS with positive pulses (HiPIMS $V^+$) and DC-pulsed with positive pulses (DC-pulsed $V^+$). Then, for those coatings deposited by DC-pulsed $V^+$ we study the influence of diverse deposition parameters (hydrogen incorporation, deposition temperature and substrate bias) on the structural and mechanical properties of the samples. Finally, molecular dynamics simulations of a nanoindentation process are used to identify the atomic scale mechanism of deformation of DLC films with different $sp^3$ concentrations, stressing the role of $sp^3$ bonding on mechanical properties.

# 2. Experimental methods

Various DLC coatings were deposited by magnetron sputtering onto (100) Si substrates. Prior to deposition, the substrates were thoroughly cleaned following a sequence of steps consisting of ultrasonic washing with alkaline detergents, rinsing with de-ionized water, cleaning with isopropanol and air-drying.

Magnetron sputtering deposition was carried out in the setup described in the Chapter 2. In order to ensure a good coating-substrate adhesion, the adhesion enhancement process described in Chapter 3 was used. The carbon deposition process is highlighted in each section, emphasizing on the main parameters of influence in the optimization study.

It is well known that the maximum $sp^3$ content achievable by the sputtering method is around 40% [8, 9] and in order to further increase the $sp^3$ content one has to make use of more energetic deposition techniques such as PLD. Therefore, in order to compare with our sputtered deposited DLC coatings, we have also evaluated the mechanical performance of a DLC sample deposited by PLD (see table 1). This sample was deposited by Dr. Diaz-Nuñez at the CLUR/UCM. The PLD set up consists of a stainless steel chamber connected to a Nd:YAG laser. The sample was deposited on a (100) Si substrate from a graphite target located in a rotating holder to avoid crater formation due to laser ablation. Deposition took place at a pressure of $8.6 \times 10^{-4}$ Pa and at room temperature. The distance between the cathode and the substrate was 4 cm. The laser was operated using 266 nm laser pulses (fourth harmonic of a Nd:YAG laser, Continuum Surelite), with a repetition rate of 10 Hz, a pulse duration of 6 ns, and an applied pulse energy of 20 mJ. The laser beam was focused on the target with a 35 cm focal length lens with an angle of about 35°. The deposition time was set to 2 hours.

Raman and EELS spectroscopy were used for structural characterization of the samples. The analysis of the elemental composition was performed by RNRA with special attention to the hydrogen concentration. The mechanical properties were characterized by nanoindentation, following the methodology described in Chapter 2. The indentations were carried out under load control, using loading, holding and unloading times of 5, 5 and 2 s, respectively and peak loads of 7 and 12 mN.

# 3. Computer simulation method

In order to have a deeper understanding about the atomic scale deformation mechanisms, with focus on the $sp^3$ concentration, computer simulations of the nanoindentation process were performed by using Molecular dynamics.

MD simulations were performed by Dr, Valencia, Dr. Gonzalez Valdes from the Universidad Mayor in Chile and Dr. Bringa from the Universidad Nacional de Cuyo in Argentina. Our contribution to their work was related to the fabrication of appropriate samples, their experimental characterization and the discussion of the results. The computer simulations of nanoindentation tests were carried out with the LAMMPS code [11] for amorphous carbon samples with different $sp^3$ content (10, 15, 20, 25, 30, 35, 40 and 55%). Carbon bonding was defined based on a coordination criterion. A carbon atom is $sp^2$ bonded if it has 3 carbon atoms within 2.0 Å cutoff radius, and $sp^3$ bonded if it has 4 carbon atoms within the same cutoff radius. The C-C interaction was simulated using the Environment-Dependent Interatomic Potential EDIP [12], since it reproduces the amorphous carbon density and $sp^3$ composition in good agreement with experimental and DFT results [13, 14]. Every amorphous carbon sample was prepared following the thermal treatment proposed by Thomas et al. [13]. Once the DLC with the desired density is achieved, periodic boundary condition in z direction are removed, and the sample is relaxed during 50 ps to allow surface reconstruction. Nanoindentation was performed in a micro-canonical ensemble and system temperature was controlled by means of a Langevin thermostat which is coupled to a 1 nm thickness region on the xy simulation box borders following the procedure discussed by Ruestes et al. [15, 16].

The indenter consists of a spherical tip of 2.5 nm radius and the interaction indenter-substrate is described by means of a harmonic potential of the form

$$U(r) = K(r - r_0)^3$$

Where $r_0$ is the indenter radius and K=10 $e$V/Å$^3$ is a constant which describes the indenter stiffness. The tip velocity of 10.0 (m/s) was selected to ensure reliable results for the determination of elastic properties [15]. The indenter was inserted 2 nm and then held during 20 ps before being removed. Indenter contact atoms were computed following the rule proposed by Ziengenhain et al. [17], which consider an atom in contact with the indenter if $|r-r0| < 0.2$ Å . The applied load ($F$) with the indenter depth ($d$) are related by the Hertz model by means of

$$F = \frac{4}{3} E_r R^{1/2} d^{3/2},$$

Where $E_r$ is called the reduced elastic modulus.

# 4. Results and discussion

## 4.1 Optimization of hard DLC coatings by magnetron sputtering

This section summarizes the influence of the deposition conditions on the structure and on the mechanical properties of the sputtered amorphous carbon films deposited by magnetron sputtering. For this study, four basic deposition parameters are considered: (i) sputtering mode, (ii) hydrogen incorporation during carbon deposition, (iii) deposition temperature and (iv) substrate bias voltage.

It is important to mention that because of the inherent intercorrelation of the deposition parameters, the study of the influence of each individual parameter can be a formidable task. Therefore, the main aim of the study presented in this section is more oriented to find out optimal deposition conditions leading to coatings with improved mechanical properties rather than to study from a fundamental point of view the influence of every individual parameter on the coating properties.

### 4.1.1 Sputtering mode

In this section we investigate the influence of the sputtering mode on the structural and mechanical properties of the samples. To do that, we compare the properties of samples sputtered by using four different modes: DC, HiPIMS, HiPIMS with positive pulses (HiPIMS $V^+$) and DC-pulsed with positive pulses, (DC-pulsed $V^+$). In order to achieve comparable results, the target voltage, the working pressure and the bias voltage were the same in all cases. Special attention is paid to the hydrogen incorporation to the coating from the residual gas in the deposition chamber since it could also influence the coating performance.

A schematic overview of the deposition parameters is given in Table 1.

**Table 1.** *Overview of the deposition parameters for DLC coatings sputtered in different modes: DC, HiPIMS, HiPIMS with positive pulses (HiPIMS V+), and DC-pulsed with positive pulses (DC-pulsed V+).*

| Sample | **DC** | **HiPIMS** | **HiPIMS_V+** | **DC-pulsed_V+** |
|---|---|---|---|---|
| **Target power (W)** | 600 | 600 | 600 | 600 |
| **Working Pressure (Pa)** | 0.56 | 0.56 | 0.56 | 0.56 |
| **Target voltage (V)** | -1050 | -1020 | -1045 | -1050 |
| **Target peak current (A)** | 0.57 | 200 | 350 | 1.39 |
| **Frequency (Hz)** | --- | 250 | 160 | $1.5x10^5$ |
| **Pulse time (µs)** | --- | 45 | 45 | 2.7 |
| **Duty cycle (%)** | 100 | 1.2 | 72 | 40 |
| **Positive pulse amplitude (V)** | --- | --- | 400 | 500 |
| **Substrate voltage bias (V)** | 50 | 50 | 50 | 50 |
| **Hydrogen content (at. %)** | 5 | 30 | --- | 12 |
| **Deposition rate (nm/h)** | 292 | 232 | 207 | 245 |

Firstly, we comment on the diverse deposition conditions (peak currents, deposition rates...) at which the coatings are grown, resulting from each sputtering mode. As shown in table 1, we observe that the largest target peak currents are obtained when using HiPIMS both without (200 A) and with positive pulse (350 A). This value is orders of magnitude higher than that for DC-pulsed (1.39 A) and for DC (0.57 A). This is because, the high peak powers delivered by HiPIMS power supplies allow sustaining much higher current glow discharges.

The deposition rate also depends on the sputtering mode, being lower for the coating deposited by HiPIMS (232 nm/h) than for the coating deposited by DC (292 nm/h). There are two reasons for that: on one hand, when using HiPIMS, a larger fraction of sputtered atoms is ionized, in such a way that many of the newly formed ions return to the target instead of being incorporated to the deposited film. On the other hand, the high current densities during the HiPIMS plasma discharge leads to higher densification of the coatings thus, reducing the deposition rates.

From the data shown in table 1 we also observe that the introduction of positive pulses reduces the coatings' deposition rate in both DC and HiPIMS modes. The deposition rate for HiPIMS $V^+$ is 207 nm/h and that for DC-pulsed $V^+$ is 245 nm/h. Such a reduction in the deposition rate is also related to the densification of the carbon structure, as demonstrated in Chapter 4.

The deposition mode does not only affect the deposition parameters but also the incorporation of hydrogen from the residual gas to the coating. Pulsing during deposition leads to samples with a larger H content. The largest H content was measured for the sample deposited by HiPIMS (30 at. %). This is so because hydrogen present in the residual gas is preferentially incorporated into the gas mixture while pulses are off, thus increasing the occurrence of reactive sputtering. The high reactivity of hydrogen with carbon leads to the formation of thin hydrocarbon compound layers on the target surface that will be further incorporated into the coating.

Fig. 1 shows Raman spectra for the coatings sputtered by diverse modes. Characteristic D and G bands of carbon were identified for all samples at around 1360 $cm^{-1}$ and 1540 $cm^{-1}$(by fitting the Raman spectra using two Gaussian functions). The Raman spectra for all coatings exhibit broadening and overlapping of the two bands, indicating a disordered amorphous carbon structure [18].

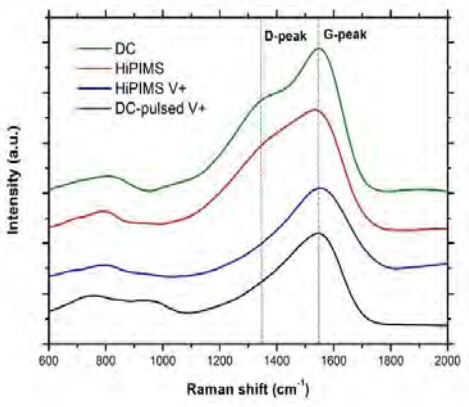


**Figure 1.** *Raman spectra measured for DLC coatings deposited by using different modes of magnetron sputtering: DC (green), HiPIMS (red), HiPIMS V+(blue), and DC-pulsed V+(gray).*

The $I_D/I_G$ ratio has been used as an indicator for the structural differences of the carbon coatings. The H content together with the most representative Raman structural parameters ($I_D/I_G$ ratio and G position) and mechanical properties for samples sputtered in different modes are illustrated in Table 2 [18, 19]. The sample sputtered by DC shows a high $I_D/I_G$ ratio (1.25) together with a clear transition between D- and G- peaks. The use of HiPIMS smooths the transition and reduces the $I_D/I_G$ ratio (0.92). The introduction of positive pulses (HiPIMS $V^+$ and DC-pulsed $V^+$) has a major impact on further lowering the $I_D/I_G$ ratio (0.33 for HiPIMS $V^+$ and 0.37 for DC-pulsed $V^+$), as demonstrated in Chapter 4.

**Table 2.** *Hydrogen content, $I_D/I_G$ ratio, G position, Hardness and Modulus of DLC coatings sputtered in different modes (DC, HiPIMS, HiPIMS with positive pulses (HiPIMS V+), and DC-pulsed with positive pulses (DC-pulsed V+)).*

| Sample | DC | HiPIMS | HiPIMS_V+ | DC-pulsed_V+ |
|---|---|---|---|---|
| **H content (at. %)** | 5 | 30 | --- | 12 |
| **$I_D/I_G$ ratio** | 1.25 | 0.92 | 0.33 | 0.37 |
| **G position ($cm^{-1}$)** | 1556 | 1538 | 1545 | 1542 |
| **Hardness (GPa)** | 8.9±0.5 | 9.7±0.6 | 20.1±1.0 | 26.6±1.2 |
| **Reduced elastic modulus (GPa)** | 126±6 | 131±5 | 188±8 | 210±10 |

The calculated G position (around 1540 $cm^{-1}$) and $I_D/I_G$ ratios suggest that all studied coatings are either in a stage 2 (a-C) or in the transition to stage 3 (ta-C) of the Ferrari´s three stage model for a 514 nm excitation wavelength [18].

Fig. 2 shows load-depth nanoindentation curves for the DLC coatings sputtered in different modes measured at an indentation load of 7 mN. The maximum penetration depth was observed for the DLC coatings deposited by DC (≈ 210 nm), followed by HiPIMS (≈ 190 nm), while much lower depths (< 135 nm) were measured for DLC coatings deposited with positive pulses (HiPIMS $V^+$ and DC-pulsed $V^+$). The fact that the area inside the load-depth curves is smaller for the DLCs deposited with positive pulses (HiPIMS $V^+$ and DC-pulsed $V^+$) than for those which have been deposited without applying any positive pulse, indicates that the application of positive pulses leads to samples that have a higher elastic recovery with less energy dissipated during deformation.

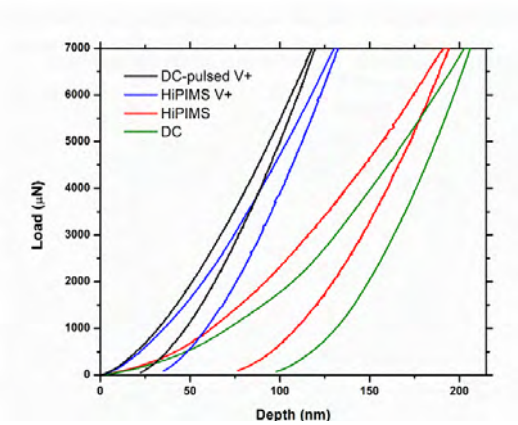


**Figure 2.** *Load-depths curves measured at an applied load of 7 mN for different DLC samples sputtered in diverse modes: DC (green), HiPIMS (red), HiPIMS V+ (blue) and DC pulsed V+ (black)*

The hardness and modulus calculated from the curves shown in Fig. 2 are given in Table 2. In agreement with the data shown in chapter 4, we observe that the addition of positive pulses during the pulsed sputtering discharges has a significant impact on the mechanical properties. DLC coatings deposited in DC and HiPIMS modes have lower hardness and reduced modulus than those deposited by HiPIMS $V^+$ and DC-pulsed $V^+$. Disregarding the H content, which according to literature may not have a significant influence on the mechanical properties for contents below 30 at.% [1,18], and considering that the mechanical properties for the sample sputtered in HiPIMS mode (largest H content of 30 at. %) are much lower than those sputtered by DC-pulsed $V^+$, we can conclude that the observed improvement of the mechanical properties when introducing positive pulses during deposition can be explained on the basis of the subimplantation-relaxation model [6, 7].

This model sets out a relationship between the energy of the depositing species and the probability to increase or decrease $sp^3$ bonding contents. There is an energy, here termed as penetration energy ($E_p$), which is required for an atom to penetrate within the growing film. This energy is required to displace an atom and form a vacancy-interstitial pair. When the energy of the incoming atoms ($E_{inc}$) is lower than $E_p$, the atoms will remain at a surface in a low energy configuration, forming $sp^2$ chains. However, if the energy of the incoming atoms is high enough ($E_{inc} > E_p$), they will be able to penetrate through the surface (a process known as subimplantation). This results in an increase of the interstitial-vacancy pairs that ultimately lead to a densification in the subsurface region, thus promoting $sp^3$ bonding configurations. If incoming energies are too high, the subimplantation processes generate a thermal spike. This excess of energy in the form of heat induces the relaxation of the $sp^3$ structure back to $sp^2$.

In the densification regime, the film density, the $sp^3$ content and therefore the mechanical properties increase with rising carbon ion energies (within the range: 5 eV<$E_{inc}$<100 eV). Nevertheless, the energies involved during magnetron sputtering processes are usually in the low range (few tens eV), still far below the optimum values observed in the transition from densification to relaxation (~100eV). Even though positive pulses configuration allows increasing depositing energies, new sputtering configurations and the optimization of other factors such as hydrogen incorporation, deposition temperature or substrate bias voltage need to be addressed in order to boost $sp^3$ content on the deposited carbon coatings.

In this thesis, we have selected DC-pulsed $V^+$ as the technique for further optimization of the deposition parameters as it offers good mechanical properties, reasonable deposition rates and more stable control over the hydrogen incorporation. Therefore, in the following sections, we will focus on the influence of different process parameters on the mechanical properties of samples sputtered in this mode.

## 4.2 Influence of the deposition parameters on properties for samples deposited by DC-pulsed V+

### 4.2.1 Hydrogen incorporation

In hydrogen-free DLC, the structural properties of the films are discussed using Raman analysis through the amorphization model proposed by Ferrari [18, 20]. A decrease of the $I_D/I_G$ ratio is linked to higher $sp^3$ content, density and mechanical properties, and therefore, the Raman spectra can also be correlated with mechanical properties and ultimately, with process conditions. This analysis still holds for amorphous carbon with H contents under 30 at. %. For coatings with H contents larger than 30 at. %., this model is not valid any more since the increase in the overall (C-C and C-H) $sp^3$ content would be solely due to the increase in the C-H $sp^3$ and not the C-C $sp^3$ content [18, 21].

The aim of this section is to further optimize the mechanical behavior of DLC coatings by increasing the amount of hydrogen within the carbon structure, investigating the influence of hydrogen on the structural order. To do that, we have deposited three different samples by keeping constant the target power (600 W), the working pressure (0.56 Pa) and the bias voltage (50 V), and only changing the hydrogen flux. Only residual gas was present for the a-C coating, while hydrogen fluxes of 5 sccm and 20 sccm were used for producing a-C:H coatings. Deposited coatings are denoted as a-C, a-C:H (low) and a-C:H (high) in reference to the selected hydrogen flux.

The synthesis conditions of these hydrogenated DLC coatings are summarized in the following table (3):

**Table 3.** *Process deposition parameters for DLC coatings sputtered by keeping constant the target power, the working pressure and the voltage bias, and varying hydrogen fluxes of 0, 5 and 20 sccm for a-C, a-C:H (low) and the a-C:H (high), respectively.*

| **Sample** | **a-C** | **a-C:H (Low)** | **a-C:H (High)** |
|---|---|---|---|
| **Target power (W)** | 600 | 600 | 600 |
| **Working Pressure (Pa)** | 0.56 | 0.56 | 0.56 |
| **Hydrogen flux (sccm)** | 0 | 5 | 20 |
| **Target voltage (V)** | -1050 | -985 | -745 |
| **Target current (A)** | 1.39 | 1.52 | 2.01 |
| **Substrate voltage bias (V)** | 50 | 50 | 50 |
| **Deposition temperature (ºC)** | 150 | 178 | 211 |
| **Deposition rate (nm/h)** | 245 | 267 | 340 |
| **Hydrogen content (at. %)** | 12 | 24 | 26 |

As in the previous section, the first thing to be addressed is the influence of H addition to the sputtering gas on the deposition conditions. As shown in table 3, by feeding the glow discharge with hydrogen, the plasma current increases from 1.39 A (0 sccm) to 2.01 A (20 sccm) and the target voltage consequently decreases. The current increase may be related with the formation of hydrogen ions and hydrogen containing ions such as $H^+$, $C_2H^+$, etc. [22]. It is worth noting that a fraction of these ions bombard the graphite target modifying the target composition. Moreover, as reported by Woods et al. [23] the hydrogen ion bombardment increases the secondary electron emission yield (SEEY) of a graphite target, resulting in more hot electrons being injected into the plasma volume which leads to an increase in the deposition temperature. In agreement with Woods et al., we observe that the deposition temperature increases when rising hydrogen fluxes. The maximum temperature during the deposition was 150ºC for the a-C, 178ºC for the a-C:H (low) and 211ºC for the a-C:H (high).

Next, we study the influence of the H content (hydrogen incorporated into the film) on the structure and mechanical properties of the samples. As shown in table 3, the hydrogen incorporated into the carbon structure ranges from 12 at. % for a-C (as a result of residual gas pick-up), to 24 at. % for a-C:H (low) and 26 at. % for a-C:H (high). We observe that changing the H flux from 5 to 20 sccm does not significantly modify the H incorporated into the film (it can be assumed that it is the same within the error margin). Thus, we can say that we have reached the so called saturation regime. Something similar has been observed for nitrides deposited by reactive sputtering [24].

Raman spectra of the hydrogenated DLC coatings are shown in Fig. 4. The calculated $I_D/I_G$ ratio together with the determined mechanical properties are shown in table 4.

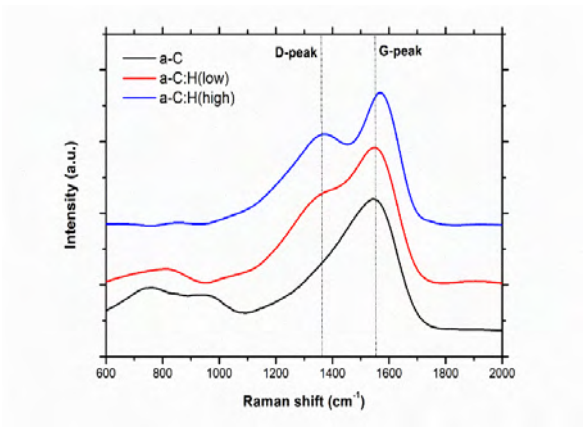


**Figure 4.** *Raman spectra of sputtered hydrogenated amorphous carbon coatings deposited keeping constant all sputtering parameters with the exception of the H flux. For the a-C only residual gas was present, while H fluxes of 5 and 20 sccm were used for a-C:H (low) and a-C:H (high), respectively.*

**Table 4.** *Evolution of $I_D/I_G$ ratio and mechanical properties with hydrogen content*

| Sample | a-C | a-C:H (Low) | a-C:H (High) |
|---|---|---|---|
| **$I_D/I_G$ ratio** | 0.37 | 1.05 | 1.95 |
| **Hardness (GPa)** | 26.6 | 18.4 | 8.2 |
| **Reduced elastic modulus (GPa)** | 210 | 162 | 95 |
| **H/E ratio** | 0.127 | 0.114 | 0.086 |

The $I_D/I_G$ ratio raises from 0.37 (a-C) to 1.05 (a-C:H (low)) which indicates an increase of the order and clustering in the $sp^2$ structure. These results agree quite well with those reported in literature which relate the introduction of hydrogen (up to 30 at. %) in amorphous carbon films with moderate $sp^3$ contents (>20%) to clustering effects, which are a result of the destabilization of the C-C $sp^3$ structure due to hydrogen incorporation [25]. Such structural effects lead to coatings with lower densities and reduced mechanical properties. In this case, hardness decreases from 26.6 GPa (a-C) to 18.4 GPa (a-C:H (low)) and the reduced elastic modulus drops accordingly from 210 GPa (a-C) to 162 GPa (a-C:H (low)).

It is worth noting the significant differences in $I_D/I_G$ ratios and mechanical properties for the a-C:H (low) and a-C:H (high) samples, particularly considering that the hydrogen incorporation is very similar in both samples. Such differences stand out that apart from the H incorporation, the presence of H in the sputtering plasma affects the deposition conditions and in particular, the deposition temperature (see Table 3). Therefore, we can conclude that the main difference between the two samples is related to the deposition temperature (178 and 211 ºC, respectively). At temperatures of 211ºC graphitization can occur, which could explain the high $I_D/I_G$ ratio (1.95) and the drastic decay in mechanical properties (H= 8.2 GPa; $E_r$= 95 GPa) observed for the a-C:H (high) sample. A more detailed study of the influence of the deposition temperature on the structural and mechanical properties of the samples is described in the following section.

### 4.2.2 Deposition temperature

According to literature, the deposition temperature has a negligible influence on the structure and mechanical properties of a-C coatings deposited with carbon ions in the right energy range (tens to few hundred eVs), as long as it does not exceed a certain critical temperature [4, 26]. Above the critical temperature, a transition can occur from an amorphous structure dominated by $sp^3$ bonds to another one where $sp^2$ bonds with strongly distorted graphitic structures prevail [4, 27], leading to a decay of the mechanical properties.

In order to study the influence of the deposition temperature on the structural and mechanical properties of the samples, a set of four DLC coatings was deposited at different powers while keeping constant the target voltage (-1050 V) and the substrate bias voltage (-50 V). Under such conditions, the increase in the power translates into an enhancement of the ion flux and thus, on the deposition temperature.

Table 5 summarizes the deposition power and temperature together with the $I_D/I_G$ ratio, hardness and modulus of the studied samples:

**Table 5.** *$I_D/I_G$ ratio, hardness and modulus of samples deposited at the same target voltage (-1050 V) and substrate bias (-50 V) and using different power (which translates in different deposition temperature).*

| Sample (power in kW) | a-C (0.6) | a-C (1.0) | a-C (1.4) | a-C (1.8) |
|---|---|---|---|---|
| **Power (W)** | 600 | 1000 | 1400 | 1800 |
| **Deposition temperature (ºC)** | 150 | 182 | 227 | 251 |
| **$I_D/I_G$ ratio** | 0.37 | 0.44 | 1.25 | 2.27 |
| **Hardness (GPa)** | 26.6 | 24.3 | 13.3 | 6.7 |
| **Reduced elastic modulus (GPa)** | 210 | 195 | 128 | 71 |

The temperature dependence of the $I_D/I_G$ ratio and reduced modulus is shown in Fig. 5

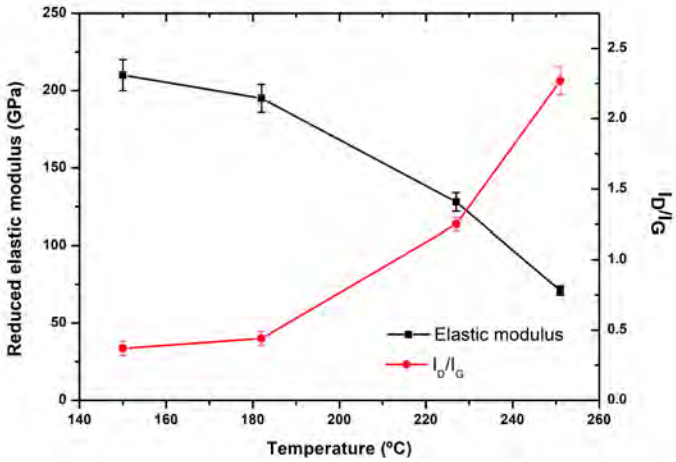


**Figure 5.** *Dependence of the $I_D/I_G$ ratio and reduced elastic modulus on deposition temperature*

In table 5 and in Fig. 5, we observe that the $I_D/I_G$ ratio strongly increases for deposition temperatures higher than about 200ºC, at which graphitization starts to occur. Such graphitization is also responsible for the strong decay of hardness and reduced elastic modulus. In particular, the clearest fingerprint indicating that graphitization has taken place in the coating is the observed large drop in modulus, whose value reflects a graphitized structure mainly governed by layered 2-D clusters of C-C $sp^3$ bonding. These results illustrate that in order to achieve DLC coatings with good mechanical properties, the deposition temperature should be kept low (under 200ºC) through adequate control of the input power, to keep ion impacts and therefore, heating of the surface, low.

These results evidence that the necessity of using low deposition temperatures during the deposition of DLC while keeping the ion energy high is a challenging task from the technological point of view. This is also important for the deposition of DLC for tribological applications, since it has to be deposited on temperature-sensitive substrate materials, like heat-treated steel, which are often limited to process temperatures below 250º. In order to avoid overheating, programmed process interruptions can be introduced, which allow intermediate cooling of the growing DLC coating.

### 4.2.3 Substrate bias

As reported by many authors, the application of a substrate bias voltage is of key importance for the mechanical behavior improvement of DLC coatings [28, 29], since the ion energy during carbon deposition depends on it according to the following equation [30]:

$$E \propto \frac{V_b}{p^{1/2}}$$

Where, E, V and p are the ion energy, bias voltage and process pressure, respectively.

Based on this knowledge, in this section we aim to study the influence of the substrate bias on the mechanical properties of the coating. To do that, we have deposited a set of seven samples using various bias voltages (from 0 to 300 V, in steps of 50 V). Table 6 shows the name given to the samples deposited at different bias voltages along with the $I_D/I_G$ ratio, hardness and elastic modulus.

**Table 6.** *$I_D/I_G$ ratio, hardness and modulus of samples deposited at the same power (0.6 kW) but varying the substrate bias (V)*

| **Sample** | **a-C (0)** | **a-C(50)** | **a-C (100)** | **a-C (150)** | **a-C (200)** | **a-C (250)** | **a-C (300)** |
|---|---|---|---|---|---|---|---|
| **Substrate bias (V)** | 0 | 50 | 100 | 150 | 200 | 250 | 300 |
| **Hardness (GPa)** | 16.6 | 26.6 | 27.2 | 29.1 | 29.2 | 23.6 | 20.2 |
| **Red. elastic modulus (GPa)** | 159 | 210 | 215 | 236 | 235 | 190 | 175 |
| **$I_D/I_G$ ratio** | 0.88 | 0.37 | 0.32 | 0.16 | 0.20 | 0.52 | 0.74 |

The hardness and reduced modulus of the DLC coatings as a function of substrate bias voltage are shown in Fig. 6.

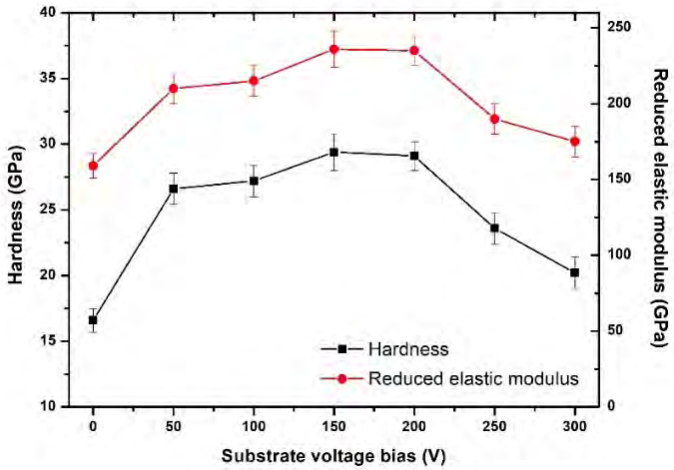


**Figure 6.** *Evolution of mechanical properties with substrate bias voltage.*

As expected, the mechanical properties for the sample deposited at a substrate bias of 50 V are significantly higher than those for the sample deposited without any substrate bias (26.6 GPa of hardness versus 16.6 GPa). For substrate bias between the 50 and 200 V, the mechanical properties further improve with increasing the substrate bias up to 200 V, reaching peak hardness and modulus of ~29.1 GPa and ~235 GPa, respectively. Then, for substrate bias voltages higher than 200 V, both hardness and modulus decrease substantially. The two regions observed in the dependence of mechanical properties on substrate bias in Figure 6 can be described considering the effect of substrate heating. The first region (at bias < 200V) would correspond to densification. As bias is increased, so does the collected ion current, promoting ion bombardment and further densification of the growing DLC, until bias equals 200V, signaling the onset of the second region. In the second region (at bias > 200V) graphitization takes over, since ion currents in the substrate are large enough to produce thermal spikes that destabilize the $sp^3$ bonding [31].

## 4.3 Structural evolution of $sp^3/sp^2$ bonding: numerical simulations and experimental results

A deeper understanding of the effect of DLC´s microstructure (in particular on the $sp^3$ concentration) on DLC´s mechanical properties requires an atomistic description of the mechanism that leads to the outstanding mechanical properties of DLC. Because of the lack of crystalline order, nanoindentation tests, even when performed in situ inside a SEM, cannot show deformation behavior that could be related to deformation mechanism modes of the different type of bonds; other characterization techniques such as Raman or electron energy loss spectroscopy fail to detect local changes in the indented regions. In this frame, Molecular Dynamics (MD) simulations stand up as a suitable tool to describe the atomic level mechanism involved in the nanoindentation process of amorphous carbon materials, contributing to clarify the mechanisms governing their mechanical properties. Indeed, MD simulations have been considered as an in-situ computational microscopy technique [29].

In this thesis, MD simulations have been performed to complement experimental data showed so far and to get a deeper understanding of the atomic mechanism governing the mechanical properties.

For this study, three samples were deposited by magnetron sputtering (a-C_1, a-C_2, a-C_3) and a fourth one (a-C_4) was deposited by PLD. In order to obtain different $sp^3$ contents, the ion energies were adjusted with increasing bias voltages: 0V for a-C_1, 50V for a-C_2 and 150 V for a-C_3. PLD has been included in the study because this deposition technique allows increasing the deposition energy while preventing excessive heating and graphitization effects, thus obtaining a sample with higher $sp^3$ content (a-C_4).

A summary of the structural and mechanical properties of the samples deposited for this study is shown in table 7:

**Table 7.** *Summary of the structural and mechanical properties of the studied samples*

| Sample | a-C_1(MS) | a-C_2 (MS) | a-C_3 (MS) | a-C_4 (PLD) |
|---|---|---|---|---|
| **$sp^3$ (%)** | 20 | 30 | 35 | 55 |
| **$I_D/I_G$ ratio** | 0.88 | 0.37 | 0.16 | 0.05 |
| **Hardness, *H*, (GPa)** | 16.6 ± 0.9 | 26.6 ± 1.2 | 29.1± 0.9 | 40.2 ± 2.7 |
| **Reduced elastic modulus, *E*, (GPa)** | 159 ± 8 | 210 ± 10 | 236 ± 12 | 274 ± 16 |
| **$H^3/E^2$** | 0.18 | 0.43 | 0.44 | 0.86 |

EELS spectra used for the evaluation of the $sp^3$ fraction of the studied coatings are presented in Fig. 7a. The EELS spectrum for a graphite sample is also shown for comparison. All studied coatings show similar fine-structures: a π* peak is clearly visible around 285 eV, with a transition region between 285 and 290 eV and finally, a high plateau between 290 and 305 eV.

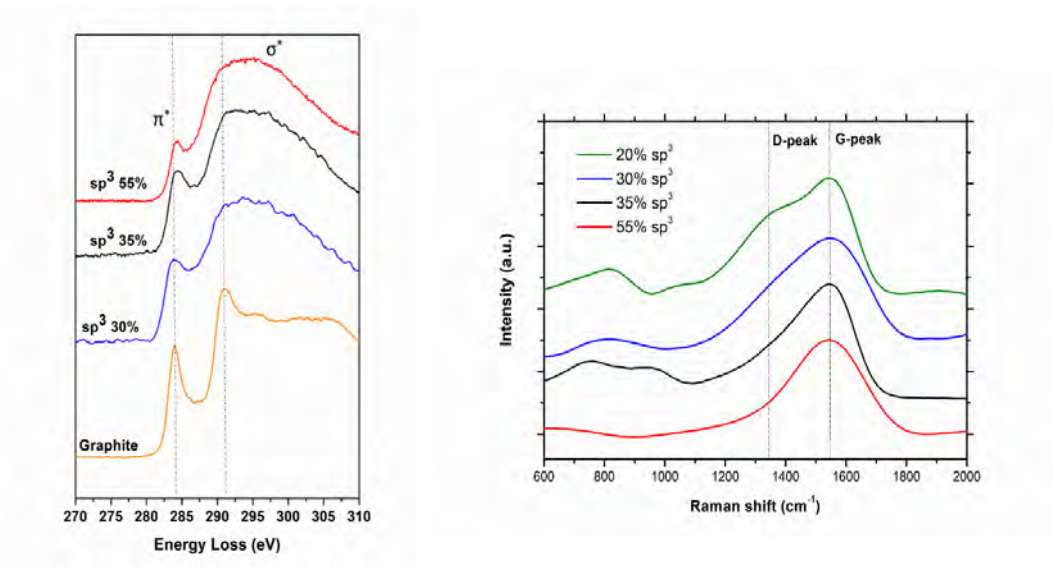


**Figure 7.** *a) EELS and b) Raman spectra for deposited DLCs (a-C_1, a-C_2, a-C_3 and a-C_4) containing varying sp3 content. The graphite reference EELS spectrum is also included for comparison.*

The intensity of the $\pi^*$ peak for all the DLC coatings is lower than that for the graphite reference sample. For the DLC coatings it reduces when increasing the $sp^3$ fraction. These results agree with previous studies which show that the presence of $\pi^*$ electrons has been associated to a rather graphitic character of the material as a result of less energetic deposition processes [18, 21]. A similar trend is observed in the Raman analysis (Fig. 7b). The reduction in the intensity of the D-peak with increasing $sp^3$ content is due to the fact that the π states become increasingly localized on olefinic chains. Olefinic bonds are shorter than aromatic bonds and have higher vibration frequencies which results in $I_D/I_G$ ratios close to zero (as shown in Table 7).

The measured (under load control) and the calculated (under displacement control) indentation load-penetration curves for DLC samples with different $sp^3$ content are shown in Fig. 8a and 8b, respectively. The deformation under load and the area inside the curves are reduced for samples with higher $sp^3$ contents, which is indicative of enhanced mechanical properties [32]. It is also worth noting how the plasticity index ($H^3/E^2$) decreases with increasing $sp^3$ content (see table 6). This observation is relevant since amorphous carbon presents a disordered atomic structure and plasticity could be difficult to observe. While irregularities or fluctuations in the load-depth curves have been reported and associated with the onset of plasticity in materials such as graphite [33], diamond [34], or even in metals, no such observations have been found in diamond-like carbon coatings. A curve inspection shows that amorphous carbon structures do not usually nucleate shear bands around the indented regions, as reported by Jungkt et al. [35] in samples with higher $sp^3$ contents where plasticity was only observed at indentation depths of ~200 nm.

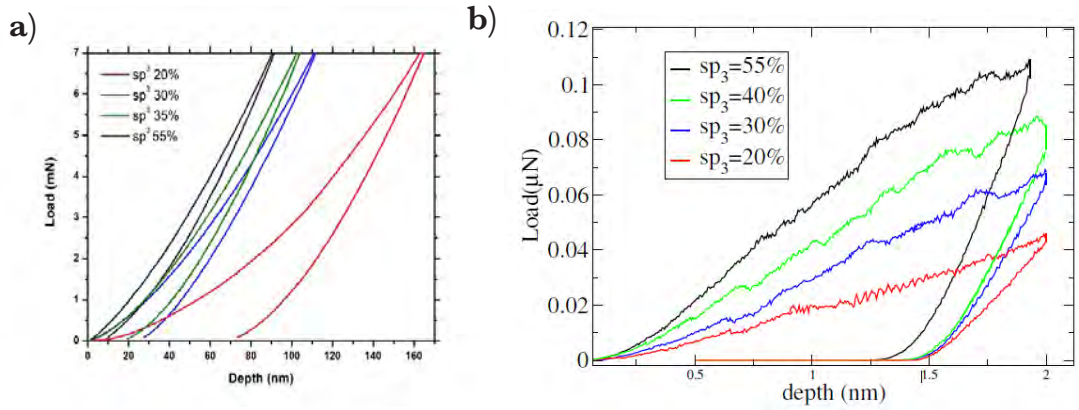


**Figure 8.** *Load vs depth curves for a-C_1, a-C_2, a-C_3 and a-C_4 (a) experimental and (b) simulated*

Simulated and experimental load-depth curves shown in Fig. 8 agree qualitatively but not quantitatively. The reason for this discrepancy is related to the differences in size and time scale between experiments and MD simulations. MD can simulate samples of the order of tens of nanometers in sample size, indenter diameter, and penetration depth, generally using spherical indenters, while experiments probe micrometer-scale samples to a penetration depth of the order of hundreds of nanometers, and use a variety of indenter shapes. Moreover, MD simulations takes a few nanoseconds for a test that a commercial nanoindenter would perform in several seconds. Despite these differences, the simulated values for hardness and elastic modulus in particular, for samples with different $sp^3$ contents, correlate quite well with experimental results, as shown in Figs. 9a and 9b.

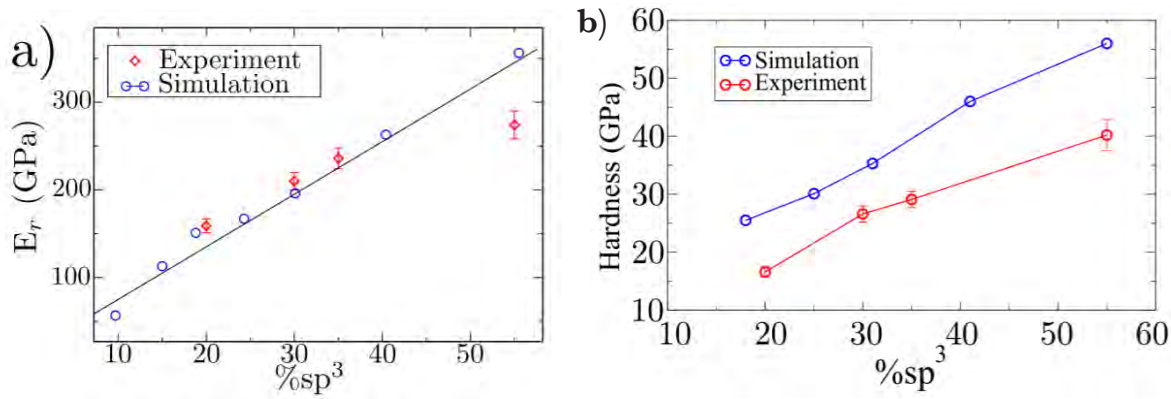


**Figure 9.** *a) Elastic modulus and b) Hardness values for samples with different $sp^3$ content: red and blue symbols represent experiments and simulations respectively.*

As shown in Fig. 9a the dependence of the measured and simulated Young modulus on the $sp^3$ fraction can be linearly fitted in the studied $sp^3$ range. Fig. 9b shows measured and simulated hardness dependence on $sp^3$ content. As expected the hardness linearly increases with rising the $sp^3$ content. It is worth noting that simulated hardness values follow the same trend as the experimental results, and for larger $sp^3$ values simulations results are in line with other experiments for ta-C [36]. The difference in the absolute simulated and measured values is related to the differences in the contact area at a given depth used in the simulation and in the experiments. Using the geometric area of the indenter usually gives a larger contact surface, and therefore a lower value of hardness in comparison with calculations which take into account the discreteness of atomic contacts. In our particular case, for the simulations, we have used the approach by Ziegenhaim [17] which gives a smaller contact area, leading to larger hardness values.

An atomistic description of the nanoindentation process is illustrated in Fig. 10. Every C atom is colored according to its shear strain, which is reflected in the plots from 32 to 55 % $sp^3$ at different indenter depths. At low %$sp^3$, shear is not only observed in the contact region, but also in regions far from the indenter. The background shear

as a function of the penetration suggests that in $sp^2$-rich samples, there is a long-range collective response, so that atoms near the tip are less constrained, and as a result, the deformation can spread outwards more easily, leading to a softer material´s response (increased plasticity). On the other hand, the sample with 55% $sp^3$ shows almost zero shear strain far from the indentation site and exhibits a high concentration of highly strained atoms in contact with the indenter tip. The difference between the two samples is attributed to the C-C hybridization: the rigid tetrahedral arrangement of $sp^3$ bonds avoids atomic displacement far from the tip, leading to the observed large increase in hardness and modulus for the sample with 55% $sp^3$ (plasticity is very much constrained near the tip).

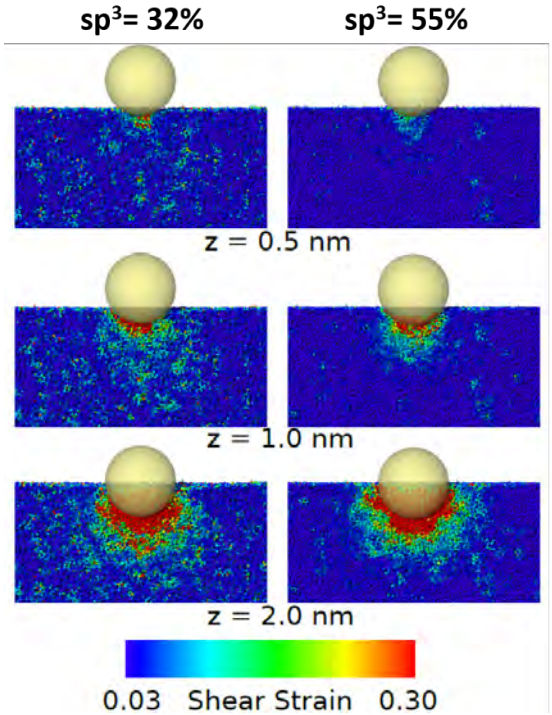


**Figure 10.** *Indentation simulation for amorphous carbon samples with $sp^3$ contents of 32 and 60%. Every picture corresponds to a half cut of the sample. Color code illustrate the shear strain of every atom*

## 5. Conclusions

This chapter evaluates the optimization of DLC coatings by establishing the influence in their structural and mechanical properties of four key factors: sputtering mode, hydrogen content, deposition temperature and substrate bias.

Pulsed modes that incorporate positive pulses have been associated with higher energetic processes, thus enhancing $sp^3$ bonding and mechanical properties. The introduction of hydrogen into the carbon structure promotes clustering effects and destabilization of $sp^3$ bonding. Clustering effects and hydrogen incorporation are difficult to control in sputtering pulsed modes, since the introduction of low hydrogen fluxes (5 sccm) during the deposition lead to coatings with high hydrogen contents (25 at.%). Besides, hydrogen assists reactive sputtering processes by enhancing the generation of hot electrons, thus increasing the deposition temperature. Graphitization effects have been observed at deposition temperatures larger than 200ºC, which are associated to substrate bias higher than 200 V. The ion current in the bias is increased with higher substrate bias, generating a local heating which reduces the mechanical properties of DLC coatings.

Molecular dynamics simulations show a good agreement with experimental results for modulus and hardness as a function of $sp^3$. At the nano-scale, the simulation of the indentation test do not show evidence of crack, shear bands or dislocations; however, the high stress introduced by the indenter tip is observed to induce increased plasticity for low %$sp^3$ (32%), as the shear stress is observed to extend outside the region closest to the tip, while for 55% $sp^3$, the density of rigid tetrahedral $sp^3$ bonds do not allow atomic displacement, only atomic rearrangement and some porosity compaction are observed, resulting in increased hardness and modulus.

*References*

*[1] Tribology of Diamond-Like Carbon films: Fundamentals and Applications, Springer, N. York, 2007*

*[2] J. Vetter, Surface & Coatings Technology 257 (2014) 213-240*

*[3] PJ Fallon et al., Phys. Rev. B 48 (1993) 7*

*[4] Y. Lifshitz et al., Diam. Relat. Mater. 4, 318–323 (1995)*

*[5] A. Grill, B.C. Meyerson, Development and status of diamondlike carbon, in Synthetic*

*Diamond: Emerging CVD Science and Technology, ed. by K.E. Spear, J.P. Dismukes (Wiley,*

*New York, 1994), pp. 91–141*

*[6] Y. Lifshitz et al., Phys. Rev. Lett. 68, 620 (1989).*

*[7] J. Robertson, Diam. Relat. Mater. 3, 361 (1994).*

*[8] J.J. Cuomo et al., J. Appl. Phys. 70, 1706–1711 (1991).*

*[9] Bernd Schultrich, Tetrahedrally Bonded Amorphous Carbon Films I, Basics, Structure and Preparation, Springer Series in Materials Science 263*

*[10] W.C. Oliver and G.M. Pharr, Journal of Materials Research, 7 (1992) 1564-1582*

*[11] S. Plimpton, Journal of computational physics 117 (1) (1995) 1-19.*

*[12] N. Marks, Phys. Rev. B 63 (3) (2000) 035401.*

*[13] C. de Tomas et al., Carbon 109 (2016) 681-693.*

*[14] N. Marks et al., Phys. Rev. B 65 (7) (2002) 075411.*

*[15] C. Ruestes et al., Molecular dynamics modeling of nanoindentation, Applied nanoindentation in advanced materials. Wiley, Chichester 315.*

*[16] C. J. Ruestes et al., Crystals 7 (10) (2017) 293.*

*[17] G. Ziegenhain et al., Journal of Applied Physics 107 (6) (2010) 061807.*

*[18] A. C. Ferrari et al., Phys. Rev. B. 62 (2000) 11089*

*[19] J. Robertson, Materials Science and Engineering: R: Reports, 37 (2002) 129-281*

*[20] A. C. Ferrari, J. Robertson, Phys. Rev. B, 64, 075414 (2001)*

*[21] G. Fanchini, A. Tagliaferro, Appl. Phys. Lett. 85, 730 (2004)*

*[22] K. Sarakinos et al., Surface & Coatings Technology 206 (2012) 2706–2710*

*[23] M E Woods et al., Journal of Physics D: Applied Physics, Volume 20, 1987 Number 9*

*[24] N. Gordillo et al., Journal of Crystal Growth 310 (2008) 4362–4367*

*[25] B. Kleinsorge et al., Diam. Relat. Mater. 10 (2001) 965.*

*[26] Y. Lifshitz et al., Diam. Relat. Mater. 2 (1993) 285–290*

*[27] W.M. Lau et al., J. App. Phys. 70, (1991) 5623–5628*

*[28] F. Ferreira et al., Surface and Coatings Technology Volume 336, 25 (2018) 92-98*

*[29] D. Sheeja et al., Wear 249 (2001) 433–439*

*[30] S. Zhang et al., Surface and Coatings Technology 167 (2003) 137–142*

*[31] PJ Kelly et al., Surface and Coatings Technology 142-144 (2001) 63-641*

*[32] Y.W. Bao et al., Acta Materialia 52 (2004) 5397–5404*

*[33] A. Richter et al., Diamond and Related Materials 9 (2) (2000) 170-184*

*[34] N. H. Faisal et al., Surface and coatings technology 242 (2014) 42-53*

*[35] J. Jungk et al., Acta materialia 54 (15) (2006) 4043-4052.*

*[36] C. Charitidis, International Journal of Refractory Metals and Hard Materials 28 (1) (2010) 51-70.*

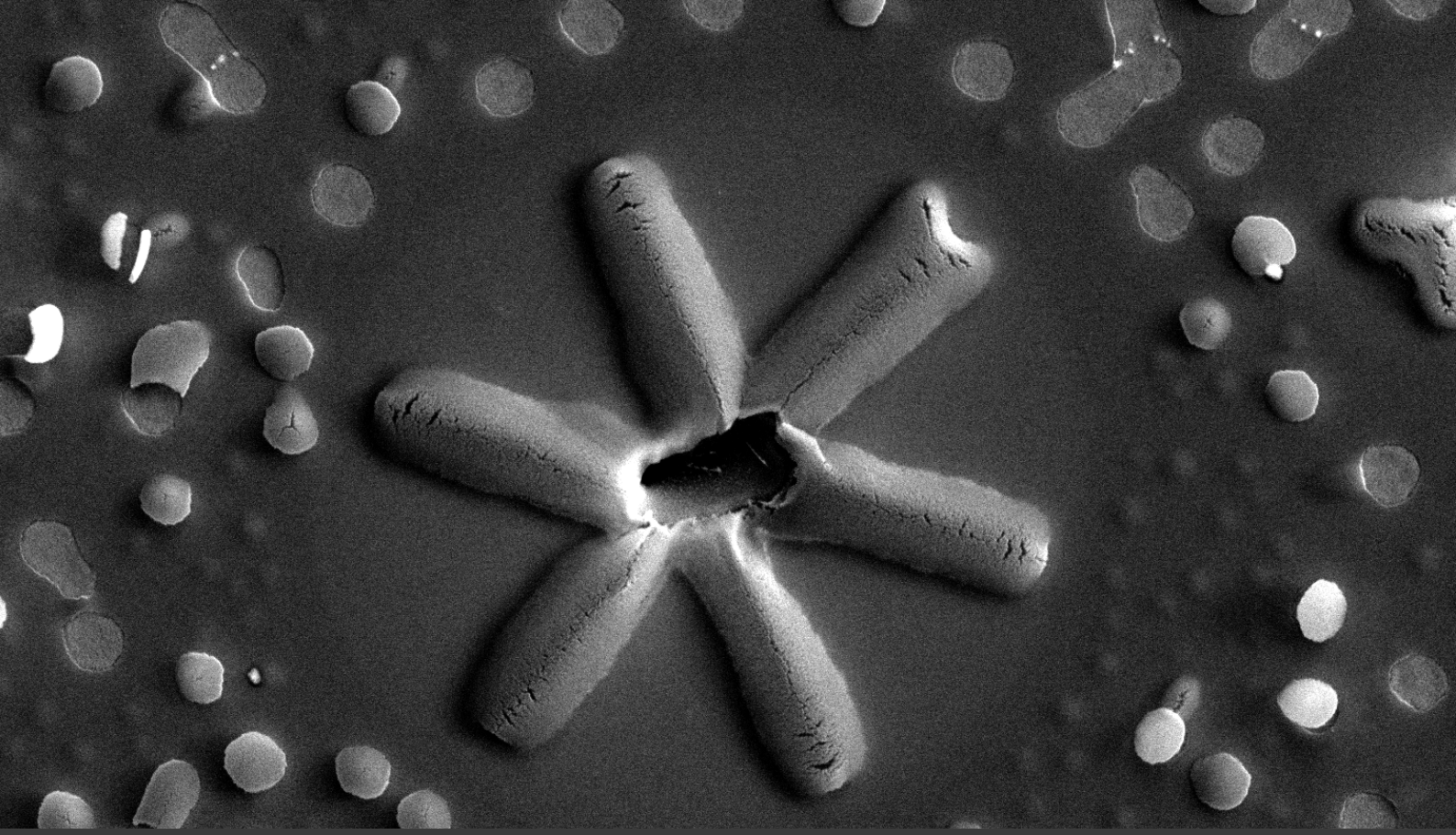

*"Better a diamond with a flaw than a pebble without" Confucio*

# Chapter 6

## Hard Cr-doped DLC coatings deposited by low-frequency HiPIMS for enhanced high-temperature tribomechanical behaviour

DLC coatings present some undesirable properties which prevent their wider use in industry. These are mainly poor adhesion (discussed in Chapter 3), which results from the high internal stress levels developed during the energetic deposition process, and low thermal stability, since their $sp^3$-$sp^2$ structure undergoes a graphitization process at high temperatures, deteriorating both hardness and coefficient of friction [1-4].

# 1. Introduction

One common strategy to overcome these handicaps is doping the DLC coatings with metal species, mainly carbide former elements such as Ti, W, Nb, Mo and Zr [5-8]. By adjusting the concentration of these metals into the carbon matrix, it is possible to form carbide nanoclusters that can restrict dislocation mobility and crack propagation. However, the formation of Me-C bonding reduces the availability of free carbon needed to generate lubricious graphitic tribolayers that improves friction and wear resistance [9]. Non-carbide formers metals such as Ag and Al have also been studied as an alternative for doping DLC coatings [10, 11]. These metals promote the formation of ductile phases that support plastic deformation of the coating, thus improving toughness and releasing internal stresses. However, the stress relaxation usually destabilizes the $sp^3$ bonding structure in the DLC matrix, which causes a decrease of the hardness of the coatings [12, 13].

Conventional magnetron sputtering techniques have been primarily used for the synthesis of metal-containing DLC coatings, often leading to low-density microstructures and poor mechanical properties because of the rather low degree of ionization for metal and gas species [14, 15]. As compared to conventional magnetron sputtering technique, HiPIMS provides larger fractions of ionized atoms in argon-metal discharges combined with high plasma densities [16, 17].

In this thesis, by synthetizing metal-doped DLC with the aid of highly ionized HiPIMS metal plasma discharges, we aim to maintain the high hardness and the low coefficient of friction values of the undoped DLC coatings, while reducing their internal stresses and improving their high temperature tribomechanical behaviour. We have explored different potential candidates to enhance the tribological behavior such as W, Ti and Cr. Among all candidate DLC-doping metals, we selected Cr for further investigation as it can provide high resistance to wear at high temperatures by promoting the formation of stable tribolayers at contact points [18, 19]. Moreover, due to its small size and tenacity, it can also improve the ability of the coating to better distribute the loads supported during service and to reduce its internal compressive stress. Cr-doped DLC coatings have been previously deposited with PVD techniques such as cathodic arc evaporation [20], magnetron sputtering [19] and linear ion beam technique [21, 22], showing in all cases a more severe graphitization of the carbon structure when Cr was introduced into the carbon matrix.

In particular, we study the influence of the Cr content and deposition parameters on the microstructure, mechanical and tribological properties of the Cr-doped coatings at different temperatures. Finally, Cr-doped DLC coatings are compared with W- and Ti-doped DLCs coatings deposited by HiPIMS, explaining their tribomechanical behaviour in terms of the different processing conditions and resulting microstructure.

# 2. Experimental methods

Me-(Cr-, Ti- and W-) doped DLC coatings with thickness ranging from 800 to 110 nm were deposited onto square (20x20 $mm^2$) M2 mirror polished steel substrates for structural and mechanical characterization. Circular SS304 stainless steel substrates with a diameter of 25 mm and a thickness of 200 µm were also used for residual stress measurements. Prior to any plasma treatment, the substrates' surfaces were thoroughly cleaned following a sequence of steps consisting of ultrasonic washing with alkaline detergents, rinsing with de-ionized water, cleaning with isopropanol and air-drying.

The depositions were carried out in the sputtering system described in the Chapter 2. Optimum coating-substrate adhesion was achieved by the following steps: 1) argon etching using a DC-pulsed substrate bias voltage of -500 V and a frequency of 150 kHz; 2) HiPIMS metal ion etching pretreatment with Cr ions using a target voltage of 1100 V, a substrate bias voltage of 750 V, a pulsing time of 100 µs and a frequency of 100 Hz; and 3) deposition of a WC interlayer in the DC-pulsed mode with a power density of 1.5 $W/cm^2$, a peak voltage of 1050 V, a pulse width of 2.7 µs and a frequency of 150 kHz . More details about the engineered interface for adhesion enhancement are provided in Chapter 3. The Cr-doped DLC coatings were deposited using a combination of HiPIMS and DC-pulsed magnetron sputtering technique at a working pressure of 0.65 Pa in a non-reactive Ar atmosphere. The graphite target was connected to an Enerpulse EN10 DC-Pulsed power supply operating at a power density of 1.5 $W/cm^2$, a peak voltage of 1200 V, a pulse width of 2.7 µs and a frequency rate of 150 kHz. The chromium target was connected to a hip-V 6 kW power supply operating under HiPIMS

mode. The power applied to the Cr magnetron and the pulsing frequency were varied to obtain different chemical compositions and microstructures. Further details on Cr deposition conditions are given in section 3.1.

For plasma characterization, voltage and current waveforms of the pulses applied on the Cr, Ti and W target were measured using a high voltage differential probe (100:1 attenuation) and a PEM Rogowski probe sensor connected to a Tektronix TPS 2012 oscilloscope.

The elemental composition of the samples was characterized by XPS and RBS. The morphology and thickness were investigated by scanning electron microscopy (SEM). The residual stress ($\sigma_f$) was measured using the substrate curvature method presented in Chapter 2.

X-ray photoelectron spectroscopy (XPS) was used to evaluate the Cr content of the coatings and the potential formation of carbides. Rutherford backscattering spectroscopy (RBS) was used to verify the chemical composition of the films.

The microstructural properties of the coatings were evaluated by Raman spectroscopy in combination with transmission electron microscopy (TEM) and scanning transmission electron microscopy - high angle annular dark field (STEM-HAADF). Electron energy loss spectroscopy (EELS) spectra were measured to evaluate $sp^3$ content of the carbon structure.

Room and high temperature (in the range 25 - 425ºC) mechanical properties were obtained by nanoindentation, following the approach described in Chapter 2. The tribological properties were measured in a pin-on-disk setup, as described in Chapter 2. Sliding tests were carried out in ambient air at different temperatures (room temperature, 100, 125, 150, 175 and 200ºC).

The reported volumetric wear rates correspond to the mean values obtained from tests run for 5000 revolutions at each temperature. The wear tracks generated on the Cr-DLC coatings and the transfer layers formed on the $Al_2O_3$ counterface surfaces during the sliding contact were examined by Raman spectroscopy and SEM with an energy dispersive spectroscopy (EDS) detection system. Some tribological tests were interrupted during the running-in period in order to carry out Raman analysis at this initial stage.

# 3. Results and discussion

## 3.1 Enhanced ionization of chromium by HiPIMS co-deposition

Fig. 1 shows the temporal evolution of the target voltage and current during Cr-doped DLC deposition for three different frequency and power conditions (see Table 1). The pulse shape obtained in all conditions remained unchanged. An initial current peak of several amperes was reached after approximately 10 μs from the beginning of deposition followed by a continuous current decay. The decrease in current after the initial peak is a common observation in non-reactive HiPIMS Cr deposition due to the displacement of working gas ions by metallic ions of the sputtered Cr target.

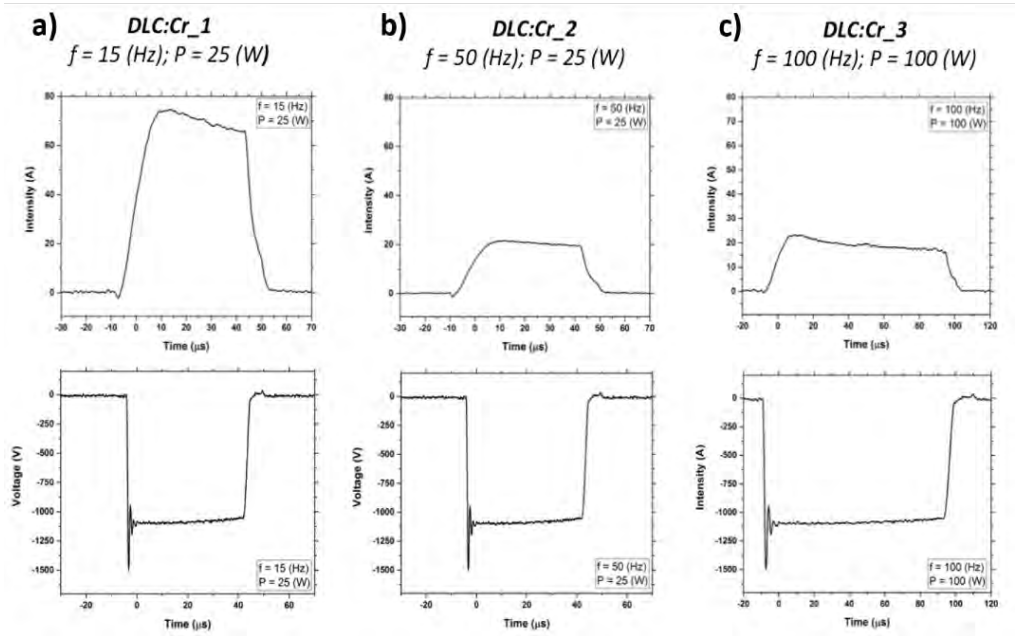


**Figure 1.** *V-I-t waveforms measured at a constant voltage of 1100 V during the deposition of a) DLC:Cr_1, b) DLC:Cr_2 and c) DLC:Cr_3 coatings*

The amplitude of the current peak during Cr-HiPIMS discharge at 1100V as a function of the working frequency is shown in Fig. 2. At frequencies higher than 50 Hz, current peak values remain constant. However, at frequencies lower than 50 Hz, a substantial increase in the current peak intensity is observed. The origin of this effect can be associated to the carbon contamination on the Cr target surface. At lower frequencies (<50 Hz), the HiPIMS pulse applied to the Cr target is mostly off and during this time thin carbon layers are formed on the surface of the Cr target, generating a light (C)-heavy (Cr) elements layered structure, which can amplify the sputter yield and the secondary electron emission by the so-called sputter yield amplification (SYA) effect [32, 33]. Heavier atoms in the target would behave as recoil centres, which would reflect the lighter atoms towards the target surface. This effect has been previously observed for carbon doped with Pt in order to increase the deposition rate of carbon-based coatings [34]. The low atomic mass of carbon favours the selection of suitable metals to achieve this effect, such as: Nb, W or, as in this case, Cr. It is worth noting that usually the increase in sputter yield is observed when the carbon target is contaminated by metal dopant atoms during a carbon plasma discharge. However, in our case, the origin of the SYA effect is the contamination of the Cr target by the deposition of C layers. The C-Cr layered structure present in the target due to contamination allowed igniting the discharge with a high current density, which remained high due to the intense secondary electron emission obtained during the first stage of the discharge. Further investigations are being carried out in order to clarify the principle of operation of this effect and its consequences.

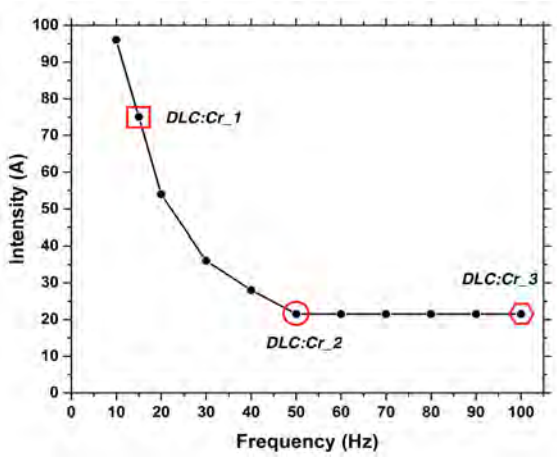


**Figure 2.** *Evolution of the HiPIMS current discharge with frequency for the diverse Cr DLC coatings.*

HiPIMS deposition parameters, Cr content, deposition rates and residual stresses of the studied coatings are summarized in Table 1.

**Table 1.** *DLC coatings deposition parameters, Cr content as estimated by XPS and RBS and residual stresses for the studied samples.*

| Sample | Power Cr (W) | Frequency (Hz) | Cr content (at. %) (XPS) | Cr content (at. %)(RBS) | Dep. rate (nm/h) | Residual stress (GPa) |
|---|---|---|---|---|---|---|
| **DLC** | --- | --- | --- | --- | 200 | -3,75 |
| **DLC:Cr_1** | 25 | 15 | 3 | --- | 210 | -2,75 |
| **DLC:Cr_2** | 25 | 50 | 9 | 9 | 235 | -1,5 |
| **DLC:Cr_3** | 100 | 100 | 20 | 18 | 265 | -1,25 |

Higher Cr target power led to higher Cr contents, with the highest Cr content (20 at.%) observed for the DLC:Cr_3 coating deposited at 100 W. However, when working at low frequencies, the carbon contamination produced when HiPIMS pulses are off played a significant role on reducing the amount of Cr incorporated to the DLC coating. For the same applied power (25 W), Cr contents of 3 at.% and 9 at.% were measured for low (15 Hz) and high (50 Hz) working frequencies corresponding to samples DLC:Cr_1 and DLC:Cr_2 respectively. As expected, deposition rates increased with power, while for the same power (25 W), lower deposition rates were found for the lower working frequency (DLC:Cr_1) as seen in Table 1. Higher currents obtained during the synthesis of DLC:Cr_1 led to higher metal ion energies during the coating deposition and increased bombardment of the growing coating surface, enhancing the peening effect and thus reducing the deposition rate. All the Cr-DLC films exhibit a residual stress lower than that of the undoped DLC sample. There are two main factors that explain the reduction of the residual stress level. Firstly, the Cr ion bombardment increases adatom mobility during the coating growth which contributes to the relaxation of the residual stress of the film [35], and secondly, the metal incorporation reduces the directionality of the C-C bond and promotes the generation of Me-C bonds. Such a distortion of the C-C bond structure reduces the compressive stress level as described in refs. [36, 37].

## 3.2 Microstructural characterization

Raman analysis was performed to obtain information on the nature of the carbon bonding structure. The Raman spectra presented in Fig. 3a are characterized by an asymmetric G band centred at ~1540 $cm^{-1}$ and an overlapping broader D band centred at ~1360 $cm^{-1}$. These two characteristic Raman active bands, usually observed in amorphous carbon films, are due to $sp^2$ sites since its Raman scattering cross section is 50 times larger than that of $sp^3$ sites [38]. The G band corresponds to the symmetric $E_{2g}$ C–C stretching mode in all $sp^2$ sites (both chains and rings), while the D band is a breathing mode of $A_{1g}$ symmetry involving only those $sp^2$ sites in rings [39]. A multiple Gaussian fit of the spectra into the G and D-peaks enables the analysis of the structural differences between coatings. Peak fitting was performed in the spectral range 800-2000 $cm^{-1}$ using Gaussian functions, as these functions give a better fit for disordered amorphous carbon films than Lorentzian functions. The D and G peaks intensity ratio ($I_D/I_G$) together with the variation of the G position for the undoped and Cr-doped DLC samples are shown in Fig. 3 (b). The calculated G position and $I_D/I_G$ ratios suggest that the presented coatings are in a stage 2 (a-C), in transition to stage 3 (ta-C) of the Ferrari´s three stage model for a 514 nm excitation wavelength [40].

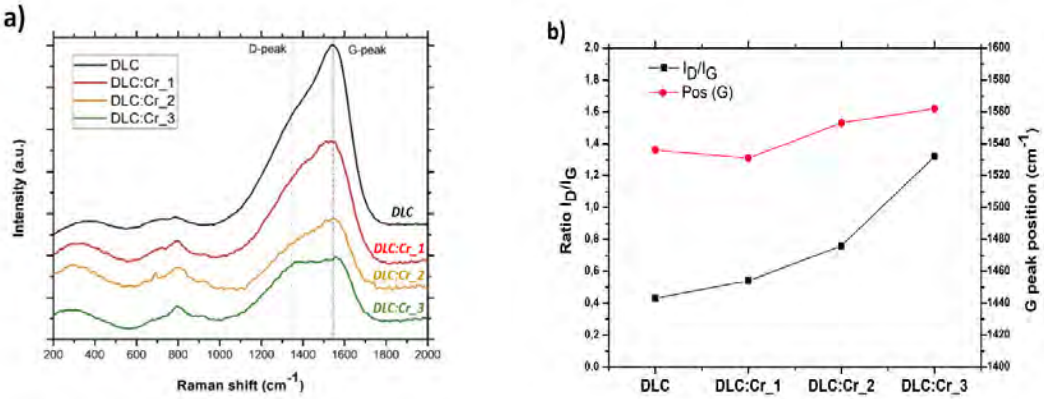


**Figure 3.** *(a) Raman spectra (b) $I_D/I_G$ ratio and G peak position for the studied undoped DLC and Cr-DLC coatings.*

It is worth noting the reduction in the intensity of the Raman signal when introducing even low amounts of Cr in the amorphous carbon matrix. This effect has also been observed in previous studies when doping with other metals such as V, Zr and W [41]. With the introduction of metal dopants, the light absorption capability of the DLC coatings is reduced, and consequently, a higher proportion of the laser beam is reflected from the surface, which cannot generate a Raman signal reaching the detector.

An important observation from Fig. 3b is that the metal addition generally increases the $I_D/I_G$ ratio, which is in accordance with previously reported studies [41]. In our particular case, the $I_D/I_G$ ratio increases from 0.43 (undoped DLC) to 0.62 (DLC:Cr_1), while for the highest Cr content (DLC:Cr_3), the $I_D/I_G$ ratio increases to 1.32. The $I_D/I_G$ ratio is proportional to the number and clustering of rings and is especially sensitive to the number of ordered rings in stage 2 to stage 3 transition [40]. A decrease in the intensity of the D-peak is associated to a gradual change in $sp^2$ sites from rings to chains and to the presence of $sp^2$ dimers embedded in the $sp^3$ matrix. The $\pi$ states become increasingly localized on olefinic chains. Olefinic bonds are shorter than aromatic bonds and have higher vibration frequencies which turns in $I_D/I_G$ ratios close to zero. This effect is more pronounced when higher $sp^3$ contents are present in the carbon structure [40].

Fig. 3b also shows that the G peak position moves to higher wavenumbers with increasing Cr content. For undoped DLC, the G-peak position is centred at 1541 $cm^{-1}$, for DLC:Cr_1 the position is slightly shifted towards lower values (1538 $cm^{-1}$), while for DLC:Cr_2 and DLC: Cr_3, the position is shifted towards more positive values (1551 $cm^{-1}$ and 1563 $cm^{-1}$ respectively). The G-peak position is also altered due to the change of the $sp^2$ configuration from rings to olefinic groups. The G skewness tends to decrease and moves towards lower wavelengths due to the more localized $sp^2$ chains [42].

Therefore, the reduction in $I_D/I_G$ together with the shift of the G-peak position towards lower values are indicative of increasing $sp^3$ fraction with decreasing Cr content. Further information on the $sp^3$ content of deposited coatings was obtained by TEM and EELS analyses, which can also provide evidence of the potential presence of carbides.

Fig. 4 shows HRTEM and HAADF-STEM micrographs representative of DLC, DLC:Cr_1 and DLC:Cr_2 samples. DLC and DLC:Cr_1 present a homogeneous microstructure characteristic of an amorphous material. However, the HAADF image of DLC:Cr_2 exhibits a nanocomposite microstructure, where the brighter grains of 2-5 nm size appear as having a composition consisting of heavier elements (higher Z), embedded in a matrix of darker contrast.

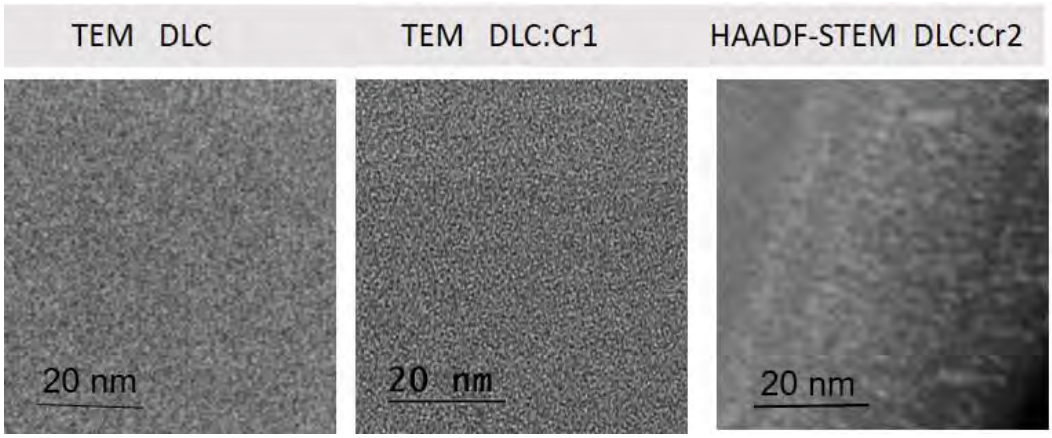


**Figure 4.** *HRTEM micrographs measured for the diverse coatings: (a) DLC and (b) DLC:Cr_1; (c) HAADF-STEM image measured for the DLC:Cr_2 coating.*

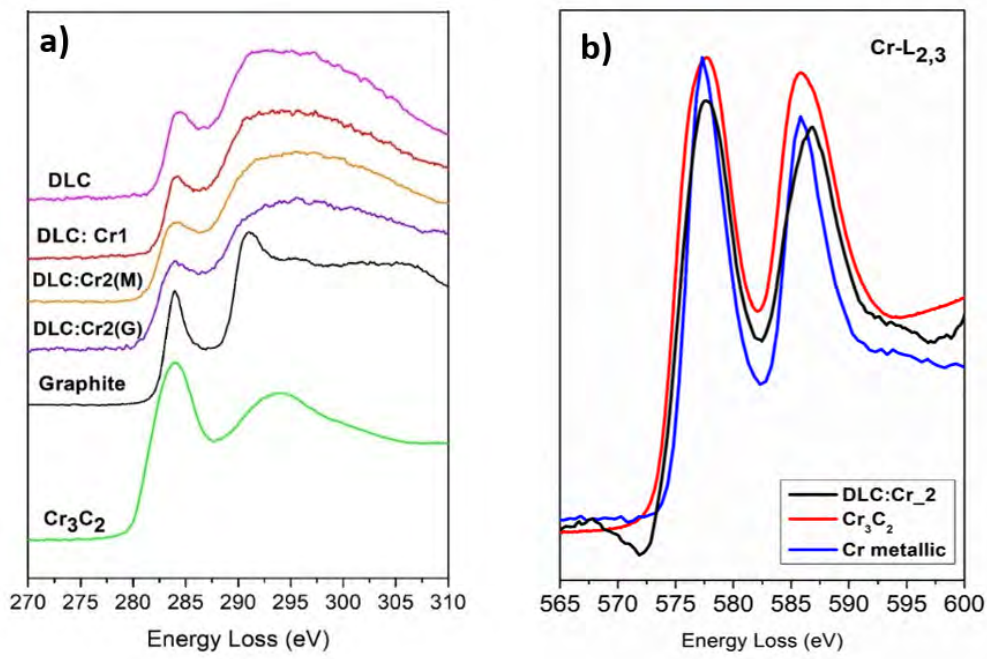


**Figure 5.** *a) C-K edge electron energy-loss spectra for DLC and Cr- DLC coatings. Graphite and $Cr_3C_2$ spectra are also shown for comparison. b) EELS of Cr L edge for the DLC:Cr_2 coatings and for reference $Cr_3C_2$ and metallic Cr samples.*

Fig. 5a shows representative EELS spectra for the same three coatings. In the case of DLC:Cr_2, the EELS spectra was measured in two different areas: within the carbon matrix (M) and within a grain structure (G). Also, a graphite and $Cr_3C_2$ spectra are presented as references for comparative purposes. The fine structure of the graphite spectrum presents two characteristic peaks, which correspond to the 1s » π* and 1s » σ* transitions occurring at ~ 284 and 291 eV respectively, while the chromium carbide presents a wider peak around 283 eV and a shoulder at 294 eV. The spectra of the DLC and DLC:Cr show similar fine-structures: A peak at 284 eV (π*peak) and a plateau between 290 and 300 eV. The intensity of π* peak at 292 eV differs from sample to sample highlighting the variations of the $sp^3$ fraction [43, 44].

The measured spectra for DLC, DLC:Cr_1 and DLC:Cr_2 (M) show very similar features, which is reflected in the estimated $sp^3$ contents of 27±3 %, 28±5 % and 24±3 % for DLC, DLC:Cr_1 and DLC:Cr_2(M), respectively. The absence of significant differences in the $sp^3$ values for the DLC:Cr_1 and the DLC:Cr_2 (M) in comparison with the undoped DLC sample indicate that the carbon atoms maintain their structural coordination in the network at these low levels of Cr incorporation (≤ 9 at.%). The spectra measured in the grain, DLC:Cr_2(G), presents a higher and wider π* peak, a decrease in the intensity of σ* peak and an increase in the intensity at energies above 294 eV. These changes can be attributed to the presence of C-Cr bonds. The spectrum can be therefore considered as a combination of DLC and chromium carbide phases. Thus, the brightest grains observed in the Fig. 4c of DLC:Cr_2 must correspond to chromium carbide grains formed inside the DLC matrix.

In Fig. 5b, the Cr-$L_{2,3}$ edge EELS spectra for DLC:Cr_2 is compared with those for metallic chromium and $Cr_3C_2$ references samples. Despite the noisy spectra for DLC:Cr_2, a difference in the ratio of the lines ($L_3$/$L_2$) can be observed. An intermediate value is obtained for DLC:Cr_2 indicating, in addition to the formation of chromium carbide, the presence of some metallic chromium $Cr^0$ atoms dispersed in the DLC matrix. For DLC:Cr_1 it was not possible to measure any Cr $L_{2,3}$ signal due to the high dispersion and low Cr content. But taking into account the above results for DLC:Cr_2 and the previous results for low Cr doped-DLC [45], the chromium in the DLC:Cr_1 sample must be distributed as metallic chromium through the carbon network. No results on $sp^3$ contents are presented for DLC:Cr_2(G) and DLC:Cr_3 because higher Cr doping contents lead to broader and overlapped peaks, which result in much more complex interpretations on the nature of the carbon structure [45, 46, 47].

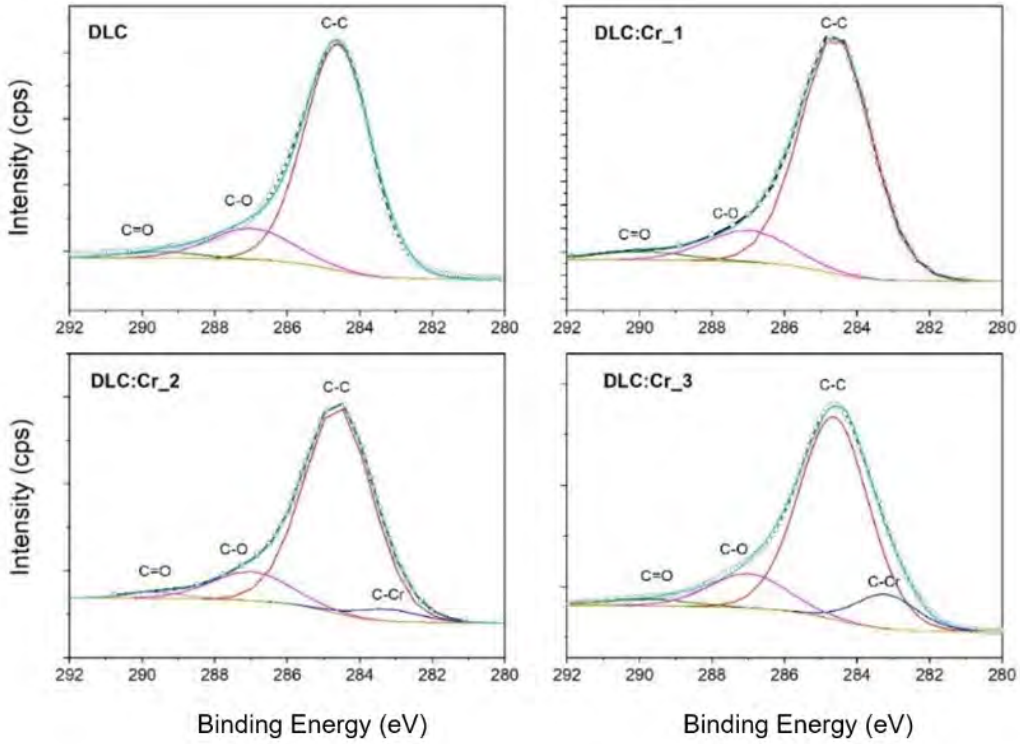


**Figure 6.** *C1s spectrum for the studied undoped DLC and Cr-DLC coatings.*

Further investigations on the formation of carbides was obtained from XPS measurements of the C1s peaks. C1s spectrum of the DLC and Cr-doped DLC coatings is shown in Fig. 6. The C1s spectrum was deconvoluted into four components centred at 283.3 eV, 284.8 eV, 286.5 eV and 288.4 eV, which correspond to C-Cr bonds, C-C bonds, C-O bonds and C=O bonds. The C-O and C=O signals are rather low and can be associated to adsorbed oxygen in the surface. There is no C-Cr peak present for DLC:Cr_1, which is expected as there is not enough Cr content for carbide formation. The intensity of the C-Cr peak increases with Cr content, but still remains very low compared to the most intense peak arising from C-C bonds.

Despite no crystalline chromium carbide phase has been found for low Cr contents, the catalytic activity during surface diffusion of the metal atoms could be responsible for promoting clustering of $sp^2$ hybridized carbon in aromatic rings [41]. In this regard, using highly energetic plasma discharges, as was the case for the DLC:Cr_1 deposition, may facilitate the introduction of Cr into the carbon network while maintaining the original carbon structure.

## 3.3 Mechanical properties

Fig. 7 shows load-depth curves for DLC coatings deposited with different Cr contents when indentations were performed using a load of 7 mN. The maximum penetration depth was ≈ 145 nm for DLC:Cr_3, while penetrations of less than 100 nm were measured for the undoped DLC sample. No substrate effect was found as maximum indentation depths were ≤ 10% of total film thickness and the results were similar to those found using a smaller load of 3 mN. Table 2 shows the hardness (H) and reduced elastic modulus ($E_r$) of the DLC and Cr-doped DLC films. DLC (H = 31.4 GPa) and DLC:Cr_1 (H = 29.2 GPa) samples exhibit hardness values that are almost twice those found for DLC:Cr_2 (H =17.6 GPa) and DLC:Cr_3 (H =15.4 GPa). The hardness and elastic modulus of hydrogen-free amorphous carbon films have been known to correlate with the carbon bonding configuration [48]. The decrease in hardness and elastic modulus of the coatings can be attributed to the formation of aromatic bonds induced by less energetic deposition processes due to increased Cr doping. This is in accordance with the Raman and EELS results presented earlier. Also, these results are in agreement with those presented in ref. [18] and [19] where the introduction of Cr led to the destabilization of the carbon structure and the subsequent hardness decay.

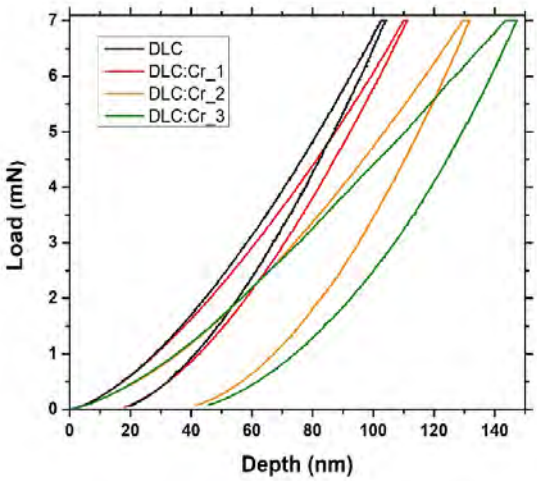


**Figure 7.** *Load-depth curves for the studied undoped DLC and Cr-DLC coatings measured by nanoindentation.*

The smaller area inside the curves for DLC and DLC:Cr_1 indicates higher elastic recovery of the coatings upon unloading as less energy was dissipated during deformation. The H/E ratio for DLC and DLC:Cr_1 is ≈ 0.125, higher than those found for samples DLC:Cr_2 and DLC:Cr_3 (H/E = 0.106), which suggests that DLC and DLC:Cr_1 coatings are able to better accommodate substrate deflections under higher loads, as the H/E ratio is related to elastic strain to failure [49]. Meanwhile, the $H^3/E^2$ ratio decreases with increasing Cr content from DLC ($H^3/E^2 = 0.516$) to DLC:Cr_3 ($H^3/E^2 = 0.176$). This ratio is an indicator of the material's ability to dissipate energy when under loading by plastic deformation [49, 50]. Thus, the addition of Cr enables the coatings to better accommodate deformation without cracking.

**Table 2.** *Mechanical properties measured for the studied DLC and Cr-DLC coatings*

| Sample | Hardness (GPa) *H* | Reduced elastic modulus (GPa) *E* | H/E | $H^3/E^2$ |
|---|---|---|---|---|
| DLC | 31.4 ± 2.7 | 245 ± 16 | 0.128 | 0.516 |
| DLC:Cr_1 | 29.2 ± 2.6 | 236 ± 14 | 0.124 | 0.447 |
| DLC:Cr_2 | 17.6 ± 1.4 | 166 ± 7 | 0.106 | 0.198 |
| DLC:Cr_3 | 15.4 ± 1.2 | 144 ± 7 | 0.106 | 0.176 |

Fig. 8 shows the evolution of mechanical properties with increasing testing temperature. Hardness values exhibit a slight steady drop for all four samples as the temperature is raised from RT to 300°C. Above 300°C, a sharp reduction in hardness is observed for DLC:Cr_3, while DLC:Cr_2 experiences a significant drop in hardness for T > 350°C. For samples DLC and DLC:Cr_1, the high hardness values are maintained for higher temperatures (> 400°C). The elastic modulus follows a similar trend, with modulus values remaining nearly constant up to 300°C, after the initial drop observed between RT and 100°C for samples DLC and DLC:Cr_1. The modulus values start to drop significantly for T > 400°C for DLC and DLC:Cr_1, while the modulus drop starts earlier and is more accused for DLC:Cr_2 (T > 350°C) and for DLC:Cr_3 (T > 300°C).

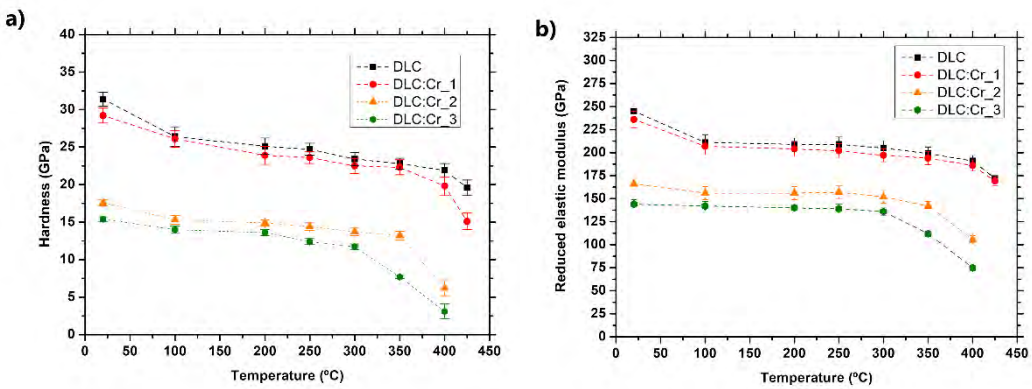


**Figure 8.** *Evolution of hardness and reduced elastic modulus with temperature for undoped DLC and Cr-DLC coatings.*

In principle, the hardness reduction during early stages of heating may be assigned to some degree of stress relaxation due to clustering of $sp^2$ sites in the films, as moderate temperatures up to 200 °C are not expected to have a noticeable effect on the fraction of $sp^3$ to $sp^2$ bonding [51]. Raman spectroscopy was used to evaluate the possible modifications on the $sp^2$ carbon film structure. Fig. 9 shows the Raman spectra of the different coatings after nanoindentation tests at 400°C.

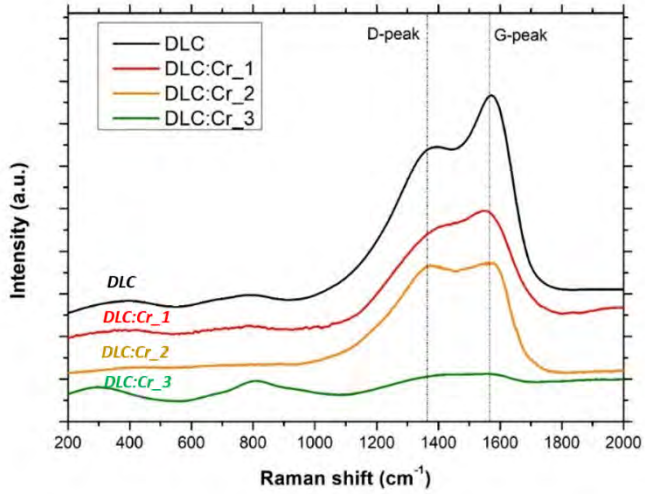


**Figure 9**. *Raman spectra for the DLC and Cr DLC coatings measured after nanoindentation at 400°C.*

After annealing at 400°C, the $I_D/I_G$ ratio rises and the G line shifts to higher wavenumbers for all samples. Table 3 shows the values of the ratio $I_D/I_G$ before and after the high temperature testing at 400°C. The largest increase in the $I_D/I_G$ ratio occurs for the samples DLC:Cr_2 and DLC:Cr_3. Also, the shift of the G peak position towards higher values is more notorious for these samples. As explained in section 3.2, the increase of the $I_D/I_G$ ratio is associated with the conversion of $sp^3$ bonds to $sp^2$ and the subsequent clustering of $sp^2$ sites [52]. The $sp^2$ site clustering leads to a reduction of compressive stresses, which is evident by the shift of the G peak position to higher wavenumbers [40].

**Table 3.** *Evolution of $I_D/I_G$ and roughness with temperature for the studied DLC and Cr-DLC coatings*

| Sample | $I_D/I_G$ @RT | $I_D/I_G$ @400°C | Roughness @RT | Roughness @400°C |
|---|---|---|---|---|
| **DLC** | 0.43 | 1.15 | 4.7 | 5.2 |
| **DLC:Cr_1** | 0.62 | 1.34 | 5.3 | 6.7 |
| **DLC:Cr_2** | 0.76 | 1.73 | 6.4 | 17.2 |
| **DLC:Cr_3** | 1.32 | 2.12 | 6.2 | 23.4 |

Also noteworthy are the changes in the surface roughness of the coatings after annealing at 400°C. The graphitization process associated with the rise in temperature starts in the near surface atoms before reaching the bulk of the coatings. The higher degree of $sp^2$ clustering at higher temperatures could be related with the appearance of small blisters (shown in the SEM image of the coating´s surface after the 450°C test). These defects probably generated during surface stress relaxation after graphitization and are the cause of the observed higher surface roughness, especially for the samples with higher $sp^2$ content, as well as the emergence of delamination spots.

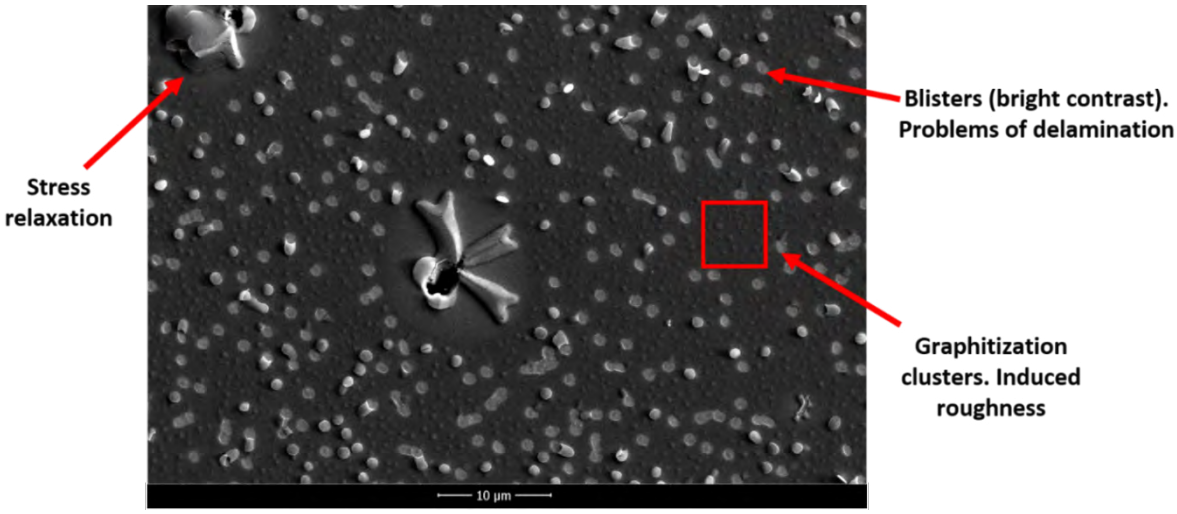


**Figure 10.** *SEM micrograph for the DLC coating after being annealed at 450°C. Graphitization process induces higher roughness and the formation of blisters and delamination spots due to stress relaxation.*

## 3.4 Tribological properties

Fig. 11a shows the coefficient of friction (COF) measured at room temperature (RT) as a function of the number of cycles for the undoped DLC and Cr-doped DLC coatings. At RT, the COF was relatively stable showing a distinguishable running-in period of less than 350 cycles, being the running-in time longer and the COF higher as the Cr content is increased. Raman analysis examined on wear tracks (Fig. 11b) revealed the presence of broad bands at 300 and 800 $cm^{-1}$ attributable to chromium oxides during the running-in period for Cr-doped DLC samples that could explain the transient increase in friction. After this initial period, the friction signal is reduced due to the formation of graphitic transfer layers, reaching a steady state with constant values that are maintained for the rest of the test. Low average values of COF were obtained during this stage: 0.16 for DLC, 0.12 for DLC:Cr_1, 0.12 for DLC:Cr_2 and 0.14 for DLC:Cr_3.

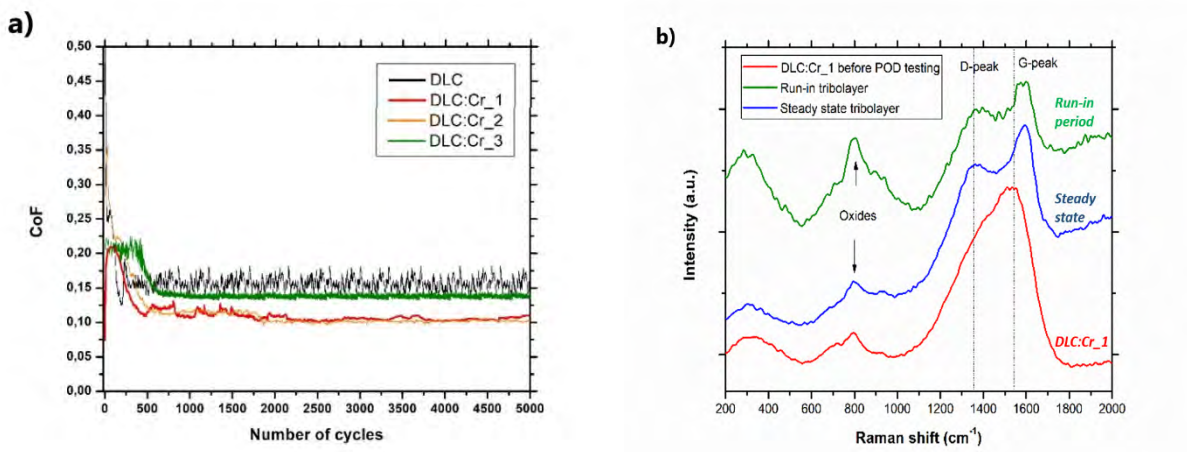


**Figure 11**. *(a) Coefficient of Friction (COF) evolution at room temperature as a function of the number of cycles for undoped DLC and Cr-DLC coatings, during a sliding test of up to 5000 cycles. (b) Raman spectra of DLC:Cr_1 coating before the test (red line), during the running-in period (green line) and at the steady state period (blue line)*

The evolution of steady state COF and wear rate values with temperature for all four samples is plotted in Figs. 12a and 12b respectively. The COF values were low at moderate temperatures up to 150°C. In this temperature range (RT-150°C), the COF decreases with increasing temperature because the graphitization process progresses relentlessly with temperature, weakening the shear strength of the surface and generating a transfer carbon tribo-layer at the sliding contact that reduces friction [2]. The temperature range where graphitization occurred during tribological testing was much lower than the one observed during mechanical testing.

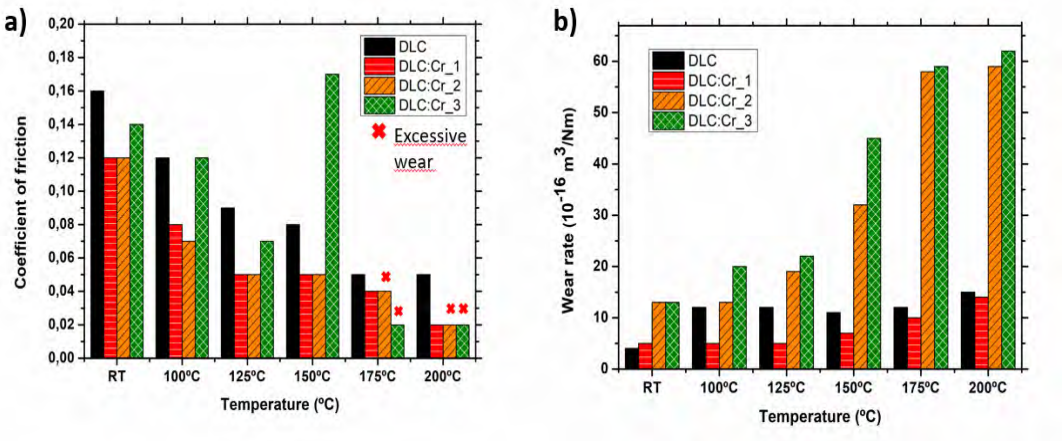


**Figure 12.** *Evolution of (a) COF and (b) wear rates with temperature for undoped DLC and Cr-DLC coatings*

Fig. 13a shows the micro-Raman spectra obtained from the wear tracks of DLC:Cr_1 at diverse temperatures (RT, 100, 150 and 200 ºC). The rise of the D-band peak intensity in the Raman spectra of the worn track surfaces indicates an increase in $sp^2$ bonds at high temperatures. These changes in the bonding structure are attributed to sliding and temperature induced graphitization [53]. Theories on graphitization of DLC, such as that proposed by Haque et al. [54], suggest that the high contact pressure exerted by debris generated during wear between sliding contacts facilitates the $sp^3$ to $sp^2$ transformation at lower temperatures than those found in quasi-static mechanical tests such as nanoindentation.

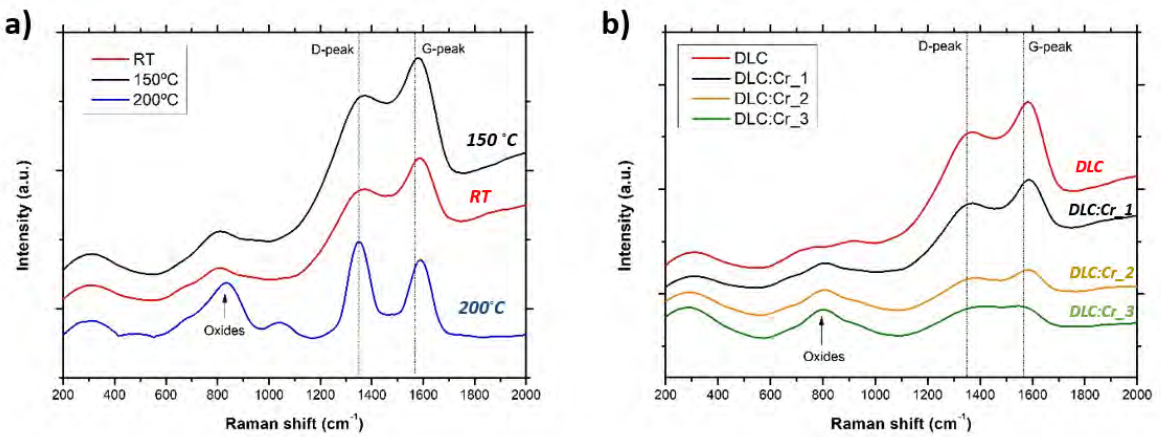


**Figure 13.** *(a) Raman spectra measured within the wear track at different temperatures for the DLC:Cr_1 coating.*
*(b) Raman spectra measured within the wear track for undoped DLC and Cr-doped DLC coatings after being tested at 150°C.*

Fig. 13b shows the Raman spectra analysed within the wear track of the samples after pin-on-disk testing at 150°C. The $I_D/I_G$ ratio was observed to increase for higher Cr contents, which indicates that the graphitization process is enhanced when higher levels of $sp^2$ sites clusters are initially present in the structure of the coatings. Graphitization is the main factor controlling the wear behaviour. Fig. 12b shows wear rates for all samples during tests performed at RT, 100, 125, 150, 175 and 200°C. DLC and DLC:Cr_1 exhibit significantly lower wear rates as compared with DLC:Cr_2 and DLC:Cr_3. A large increase in wear rates was observed for the DLC:Cr_2 and DLC:Cr_3 samples at T > 150°C, which is associated with a widespread graphitization process taking place in the coating´s surface. Severe wear is particularly visible in the scanning electron microscopy images shown in Fig. 14c-d for the samples DLC:Cr_2 and DLC:Cr_3, which were taken after tests performed at 175°C.

It is also worth noting the presence of delamination spots along the wear track on the undoped DLC coating (Fig. 14a). This brittle failure mode minimizes the amount of elastic energy stored by the large compressive stress ahead of the moving ball. The introduction of Cr into the DLC structure reduces the accumulated compressive stress within the film, preventing early adhesive failure (Fig. 14b). Small additions of Cr, as is the case for coating DLC:Cr_3 (containing 3 at.% Cr) confers optimum ductility to the loaded coating, making it more capable of distributing the load during the sliding test, and exhibiting the best sliding behaviour even at high temperatures.

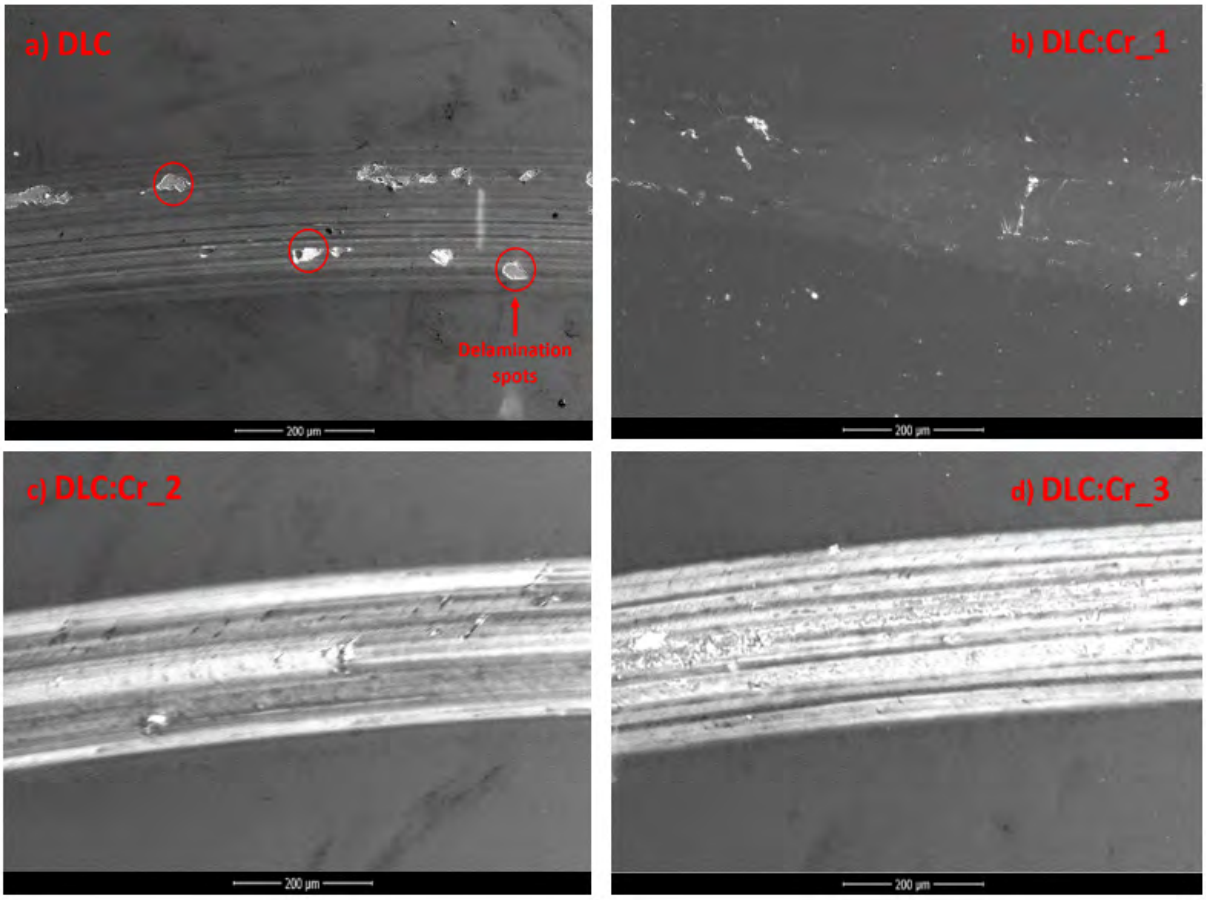


**Figure 14.** *Top view SEM micrographs for coatings after being tested at 175°C for coatings: a) undoped DLC, b) DLC:Cr_1, c) DLC:Cr_2, and d) DLC:Cr_3*

## 3.5 Comparison in tribological behaviour of Ti-,W- and Cr-doped DLC coatings

In this section, we evaluated the potential of two other metals, namely Ti and W, to replicate the unique conditions of high-density current observed during Cr-HiPIMS discharges. Besides, the structural modifications induced on the amorphous carbon matrix by the addition of Ti and W dopants was investigated and related to the tribological behaviour of the coatings.

In section 3.1, the higher current density observed during Cr-HiPIMS was associated to the sputter yield amplification (SYA) effect, which is more effective as frequency decreases. Fig. 15 shows the evolution of current with frequency for Cr, W and Ti.

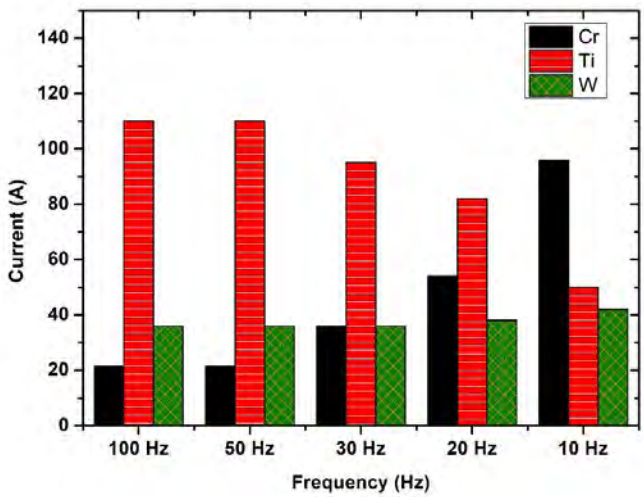


**Figure 15.** *Evolution of the HiPIMS current discharge with frequency for the DLC:Cr, DLC:Ti and DLC:W coatings.*

Fig. 15 shows that only in the case of Cr there is a clear current enhancement with decreasing frequency. For Ti, the discharge current is the highest at high frequencies, as reported in literature when no contamination effects are present [55]. Even though Ti has a sputter yield lower than many other metals (Cr and W included), the higher secondary electron emission of Ti allows reaching higher ionization levels ($Ti^{+}$, $Ti^{2+}$) and high current plasma discharges when the target is not poisoned by other elements. At lower frequencies, the contamination of the Ti target with carbon reduces significantly the current discharge due to the reduced secondary electron emission of present carbon layers.

The current obtained during W-HiPIMS and Cr-HiPIMS plasma discharges at high-medium frequencies is lower than in Ti-HiPIMS because the secondary electron emission is also much lower. When working at lower frequencies, the current increases slight ly for W-HiPIMS and notably for Cr-HiPIMS plasma discharges, which was attributed to the SYA effect (see section 3.1). This effect is not observed in the W-HiPIMS plasma discharge, even though the higher mass of W should promote this effect. In order to understand this phenomenon, further investigations are being carried out, which fall beyond the scope of this thesis.

Deposition process conditions, metal content and residual stresses for undoped DLC, DLC:Cr, DLC:Ti and DLC:W coatings are summarized in the following table:

**Table 4.** *Process parameters, metal content (obtained from XPS) and coatings' residual stress for undoped DLC, DLC:Cr, DLC:Ti and DLC:W coatings.*

| Sample | Metal content (at. %) | Power (W) | Frequency (Hz) | Current (A) | Dep. rate (nm/h) | Residual stress (GPa) |
|---|---|---|---|---|---|---|
| **DLC** | --- | --- | --- | --- | 200 | -3.75 |
| **DL-C:Cr_2** | 9 | 25 | 50 | 21.5 | 235 | -1.5 |
| **DLC:Ti** | 9 | 25 | 15 | 70 | 245 | -2.0 |
| **DLC:W** | 8 | 25 | 15 | 39 | 240 | -1.5 |

Even though DLC:Ti and DLC:W have been deposited using the same frequency as DLC:Cr_1, the metal content in these sample is very similar to that for the DLC:Cr_2. In order to study the influence of the selection of the doping metal on microstructural, mechanical and tribological properties, only samples with the same dopant content are considered (DLC:Cr_2, DLC:Ti and DCL:W).

As shown in table 4, the deposition rate for all doped samples is very similar. The residual compressive stress measured for DLC:W and DLC:Cr_2 coatings is similar (~1.5 GPa), and lower than for DLC:Ti (~2.0 GPa).

Fig. 16 shows the Raman spectra for samples doped with the same content of diverse metals. At wavenumber lower than 1100 cm-1 the Raman spectra for the DLC:W and DLC:Ti are very similar but different than that for the DLC:Cr coatings which exhibit a peak at 800 $cm^{-1}$, related the carbide formation . For wavenumbers larger than 1100 $cm^{-1}$, the Raman spectra for all samples are very similar, showing characteristic D and G bands of carbon at around 1360 $cm^{-1}$ and 1540 $cm^{-1}$. All Raman spectra exhibit broadening and overlapping of the two bands, indicating a disordered amorphous carbon structure. The $I_D/I_G$ ratios determined by Gaussian peak fitting (as previously described in chapter 2) for the diverse samples are 0.76 (DLC:Cr_2), 0.97 (DLC:W) and 1.08 (DLC:Ti).

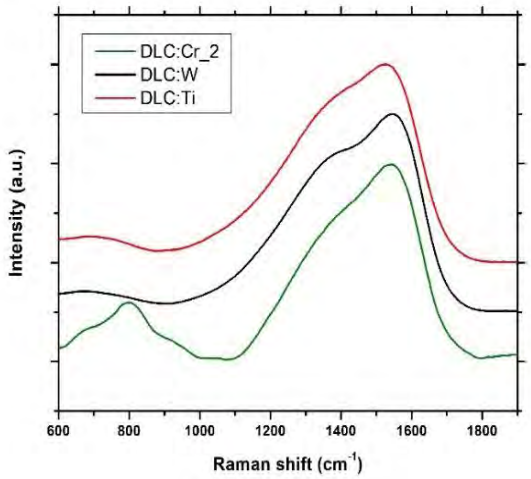


**Figure 16.** *Raman spectra for metal-DLC coatings with a doping content of around 8-9 at.%.*

The increase in $I_D/I_G$ ratio has been associated to reduced $sp^3$ contents and the incipient formation of Me-C bonds that distort the initial carbon bonding from chain-like to ring-like structures, as discussed in section 3.2. Ti is a strong carbide former, as reported in [56] because it is an element with a high number of electron vacancies in d-orbitals. W is also a good carbide former with an effective solubility slightly higher than Cr. The formation of carbides alters the $sp^3/sp^2$ bonding structure, turning the $sp^2$ configuration from aromatic bonds into olefinic groups.

The formation of metal carbides for the DLC:Ti has been directly observed by TEM, as shown in Fig. 17. In this image, two different areas can be observed: area 1 (bottom layer), corresponding to undoped DLC, which exhibits an amorphous structure and area 2 (top layer), corresponding to Ti-doped DLC, in which titanium carbide nanocrystals with a size in between 2-3 nm are embedded in an amorphous carbon matrix.

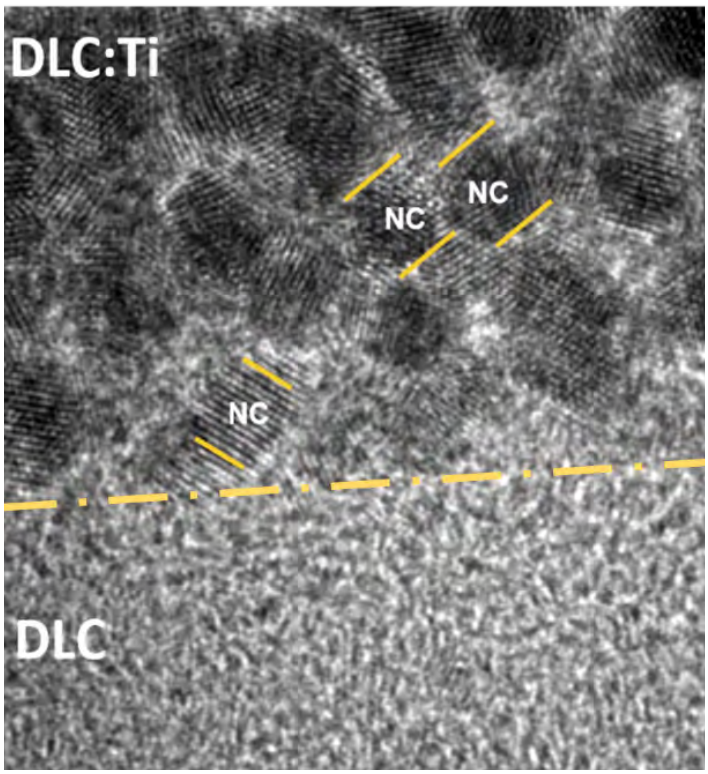


**Figure 17.** *TEM micrograph of the DLC:Ti coating showing two areas: Bottom (DLC), where no Ti-doping was observed, exhibiting an amorphous carbon structure. Top (DLC:Ti), where 2-3 nm nanocrystals (NC) of titanium carbide are embedded in an amorphous carbon matrix*

The formation of nanometric metal carbide crystals have been associated to an enhancement in the mechanical properties of the DLC coatings [6]. Table 5 shows the mechanical properties of the studied metal-doped DLC coatings.

**Table 5.** *Mechanical properties of metal-doped DLC coatings*

| Sample | Metal content (at. %) | Hardness (GPa) | Reduced elastic modulus (GPa) | H/E | $H^3/E^2$ |
|---|---|---|---|---|---|
| DLC | --- | 31.4 ± 2.7 | 245 ± 16 | 0.128 | 0.516 |
| DLC:Cr_2 | 9 | 17.6 ± 1.4 | 166 ± 7 | 0.106 | 0.198 |
| DLC:Ti | 9 | 12.6 ± 1.1 | 138 ± 7 | 0.091 | 0.105 |
| DLC:W | 8 | 15.3 ± 1.0 | 152 ± 7 | 0.100 | 0.155 |

The hardness and reduced elastic modulus are similar when comparing DLC:Cr_2, DLC:Ti and DLC:W. The formation of carbides and the destabilization of $sp^3$ bonding in Ti and W are more favorable than in Cr, leading to higher $I_D/I_G$ ratios and worse mechanical properties. The decay in $sp^3$ content is the key factor, not only for controlling the loss of hardness and elastic modulus, but also the tribological properties at high temperature.

Fig. 18 shows the tribological properties of coatings in the temperature from RT up to 200ºC for DLC, DLC:Cr_2, DLC:Ti and DLC:W.

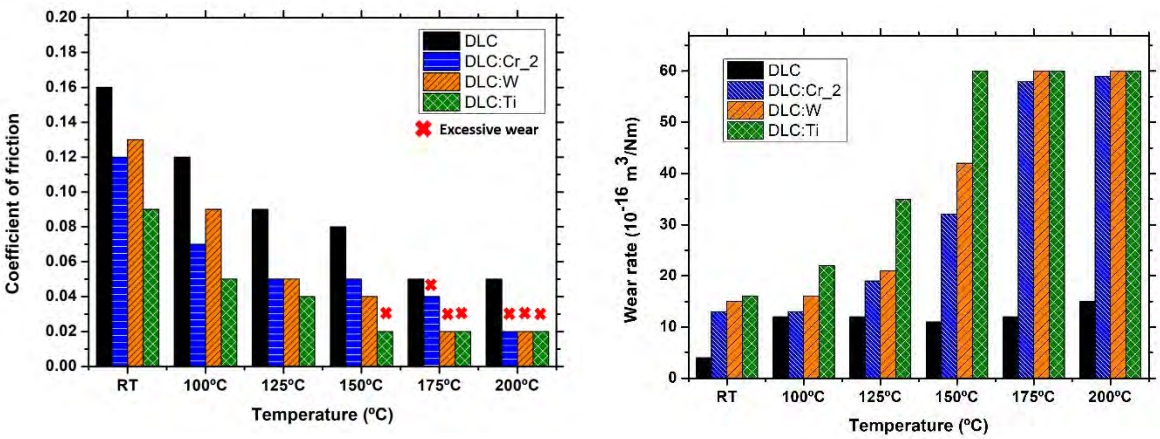


**Figure 18.** *(a) Friction coefficients of metal-doped DLC coatings at room and high temperature.*
*(b) Wear resistance of metal-doped DLC coatings at room and high temperature.*

The room temperature (RT) coefficient of friction is in all cases within the range of 0.09-0.13. The friction is governed by the formation of lubricious graphitic tribolayers. The behavior of DLC:W and DLC:Cr_2 are similar, exhibiting lower CoF than the undoped DLC. The lower $sp^3/sp^2$ bonding ratio observed for the DLC:Ti resulted in the lowest CoF value due to the greater ease of graphitizing the tribological contact.

At higher temperatures, graphitization intensifies leading to a decrease in the friction coefficients and an increase of wear rates. At 150ºC, the DLC:Ti coating experienced excessive wear, leading to test failure. The formation of titanium carbides neither help to increase the wear resistance nor contribute to increase the thermal stability of the coatings, as it has been reported for higher metal doping contents [6]. Both DLC:W and DLC:Cr_2, having similar $sp^3$ content, demonstrated higher thermal stability (up to 175ºC) than DLC:Ti (150ºC).

# 4.Conclusions

In this work, Cr-doped DLC coatings with different Cr content from 0 at. % up to 20 at. % were co-deposited using a HiPIMS technique under highly energetic conditions. The carbon-based structure (undoped DLC) was obtained using DC-pulsed mode, while the addition of Cr was controlled by the HiPIMS discharge by adjusting the pulse frequency and power. For the same power, very high-density current discharges (up to 4 $A/cm^2$) were obtained for low working frequencies (down to 15 Hz) on the Cr target, which was related to the SYA effect caused by carbon contamination on the Cr target. Under these conditions, Cr contents (up to 20 at. %) were introduced in the carbon structure without major disruption of the C-C $sp^3$ network as evidenced by Raman and EELS spectroscopy.

Room and high temperature hardness and elastic modulus values were found to be higher for the undoped DLC and for the DLC coating with the lowest Cr content (3 at. %) because of their chain-like carbon structure, which delays the graphitization process at high temperatures. The friction mechanism was found to be dominated by the formation of graphitic tribolayers as observed by Raman spectroscopy. The addition of low amounts of Cr (up to 3 at. %) into the carbon structure facilitates the formation of graphitic tribolayers at lower temperatures which provides reduced and more stable friction coefficients. Also, Cr-DLC coatings exhibit a more plastic behaviour, which prevents the early brittle failure mode observed for undoped DLC during wear testing.

Other doping strategies (using Ti and W as metal dopants), have been tested in order to achieve similar or even enhanced conditions. However, in both DLC:Ti and DLC:W cases, the high current densities observed at low frequencies Cr-HiPIMS discharges could not be reproduced. For Ti- and W-doped DLC coatings, the mechanical and tribological properties at high temperature are also governed by the stabilization of the C-C $sp^3$ structure. Both Ti and W have an increased tendency to destabilize $sp^3$ into $sp^2$, thus reducing the thermal stability and wear resistance of the coatings. Only under more energetic deposition process conditions, such as those presented in Cr-HiPIMS co-deposition at low frequencies (DLC:Cr_1), it is possible to achieve enhanced tribomechanical properties.

In summary, we successfully obtained a Cr-DLC coating that maintains the high hardness of undoped DLC while reducing compressive residual stress, extending the temperature range of operation found in existing DLC coatings, which can bring great benefits for novel high-temperature and high-load tribological applications.

References


[1] Y. Liu et al., Surface and Coatings Technology, 86-87 (1996) 564-568

[2] Y. Liu et al., Surface and Coatings Technology, 94-95 (1997) 463-468

[3] W.J. Yang et al., Thin Solid Films, 434 (2003) 49-54

[4] H. Ronkainen, K. Holmberg, Tribology of Diamond-Like Carbon Films, 155-200 (2008)

[5] J.C. Sánchez-López, A. Fernández, Tribology of Diamond-Like Carbon Films, 311-338 (2008)

[6] A.A. Voevodin et al., Thin Solid Films, 1-2 (1997) 107-115

[7] T. Vitu et al., Surface and Coatings Technology, 258 (2014) 734-745

[8] C. Corbella et al., Surface and Coatings Technology, 177-178 (2004) 409-414

[9] T.W. Scharf, I.L. Singer, Tribology Letters, 36 (2009) 43-53

[10] N.K. Manninen et al., Surface and Coatings Technology 232 (2013) 440-446

[11] S. Zhou et al., Applied Surface Science 257 (2011) 6971-6979

[12] R. Kalish, Y. Lifshitz, Applied Physics Letters, 74 (1999) 2936

[13] A.C. Ferrari et al., Diamond and Related Materials 11 (2002) 994-999

[14] U. Helmersson et al., Thin Solid Films 513 (2006) 1-24

[15] J.A. Santiago et al., Surface and Coatings Technology 358 (2019) 43-49

[16] D. Lundin et al., Plasma Sources Science and Technology, 18 (2009) 4

[17] K. Sarakinos et al., Surface and Coatings Technology 204 (2010) 1661-1684

[18] V. Singh et al., Thin Solid Films 489 (2005) 150-158

[19] C.W. Zou et al., Applied Surface Science 286 (2013) 137-141

[20] M.C. Chiu et al., Thin Solid Films 476 (2005) 258 – 263

[21] W. Dai et al., Surface and Coatings Technology 205 (2011) 2882-2886

[22] W. Dai et al., Vacuum 85 (2010) 231-235

[23] J.A. Santiago et al., Surface and Coatings Technology 349 (2018) 787-796

[24] CEN/TS 1071-11:2005: Advanced technical ceramics: Methods of test for ceramic coatings, Part 11: Determination of internal stress by the Stoney formula

[25] L. Yate et al., Surface and Coatings Technology 206 (2012) 2877-2883

[26] J.A. Leavitt and L.C. McIntyre, Jr., Nuclear Instruments and Methods in Physics Research B56/57 (1991) 734-739

[27] M. Mayer, SIMNRA, Max Planck Institut für Plasmaphysik, n.d.

[28] A.C. Ferrari et al., Physical Review B 62, 16 (2000) 11089-11103

[29] S. Urbonaite et al., Carbon 45 (2007) 2047-2053

[30] X. Zhang et al., Carbon 102 (2016) 198-207

[31] W.C. Oliver, G.M. Pharr, Journal of Materials Research 7 (1992) 1564-1583

[32] S. Berg, I. Katardijev, Surface and Coatings Technology 84 (1996) 353-362

[33] C. Nender et al., Radiation Effects and Defects in Solids 130-131 (1994) 281-291

[34] S. Berg et al., Journal of Vacuum Science and Technology A 10 (1992) 1592

[35] R. Daniel et al., Acta Materalia 58 (2010) 2621-2633

[36] C. Corbella et al., Surface and Coatings Technology 177-178 (2004) 409-414

[37] J.H. Choi et al., Journal of Physics: Conference Series 29 (2006) 155-158

[38] J. Schwan et al., Journal of Applied Physics 79 (1996) 1416-1422

[39] J. Schwan et al., Journal of Applied Physics 80 (1996) 440

[40] A.C. Ferrari, J. Robertson, Phys. Rev. B 61 (2000) 14095

[41] C. Adelhelm et al., Journal of Applied Physics 105 (2009) 033522

[42] S. Prawer et al., Diamond and Related Materials 5 (1996) 433-438

[43] R. Arenal, Appl. Phys. Lett. 91 (2007) 211903

[44] L. Lajaunie et al., Carbon 112 (2017) 149-161

[45] X. Fan et al., Appl. Phys. Lett. 75 (1999) 18

[46] C. Adelhelm et al., Surface and Coatings Technology 205 (2011) 4335-4342

[47] D.O.I. Kazuya et al., Mater. Res. Soc. Symp. 617 (2000) J7.8.1

[48] J. Robertson, Diamond and Related Materials, 5-7 (1993) 984-989

[49] A. Leyland, A. Matthews, Wear, 246 (2000) 1-11

[50] J. Musil et al., Surface and Coatings Technology 154 (2002) 304-313

[51] M. Rouhani et al., Carbon 130 (2018) 401-409

[52] Kalish et al., Appl. Phys. Lett., 74 (1999) 20

[53] T.B. Ma et al., 47 (2009) 1953-1957

[54] T. Haque et al., Wear 302 (2013) 882-889

[55] A. Anders et al., J. Appl. Phys. 102 (2007) 113303

[56] C.M. Sung, M.F. Tai, Int. J. of Refractory Metals & Hard Materials 15 (1997) 237-256

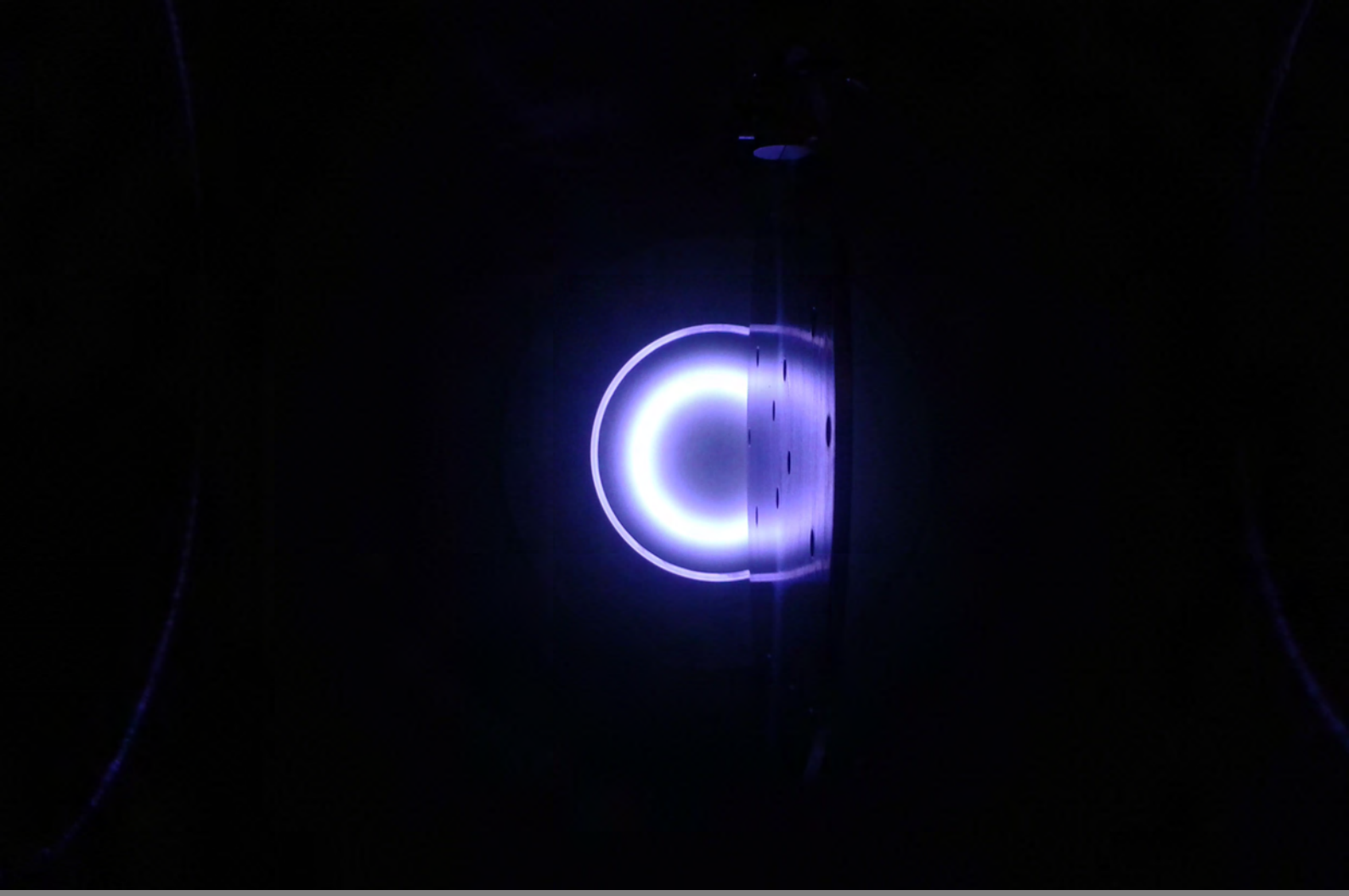

*"We shall find peace. We shall hear angels, we shall see the sky sparkling with diamonds" Anton Chejov*

# *Chapter 7*

# Conclusions and future work.

This thesis presents novel methods to harness the potential of HiPIMS technique for the deposition of DLC coatings with enhanced mechanical and tribological properties.

The **main conclusions** are summarized as follows:

- The adhesion of DLC coatings to steel substrates was enhanced by applying a newly developed pretreatment based on HiPIMS metal ion etching. The process, which makes use of Ti or Cr energetic ions, was optimized to achieve gradual and dense substrate-coating interfaces without impurities or contaminants. The study reveals the different effects on adhesion of using either Ti or Cr metal ions for the pretreatment process. Cr shows a greater ability to remove oxides and to generate a more compliant interface which results in optimal adhesion. The best adhesion has been observed when combining Cr ion etching with the use of multi-layered bonding layers. The proposed technological approach together with the scientific findings presented in Chapter 3 are of great interest to improve the adhesion of hard coatings to steel substrates for tribological applications.

- A new HiPIMS configuration with positive pulses at the end of regular HiPIMS pulses is presented, where the incorporation of positive pulses brings a substantial increase in the energy of $Ar^+$ and $C^+$ ions. This energy is directly related to the amplitude of the positive pulses. As a consequence, denser and harder carbon coatings with increased $sp^3$ contents are obtained. The application of positive pulses is not only limited to carbon plasmas but can also be applied for optimizing hard coatings such as carbides or nitrides.

- The criteria for the choice of most DLC coatings are high hardness, reduced stress, good adhesion and high density. In Chapter 5, the influence of multiple process parameters was studied and related to mechanical and tribological properties of deposited DLC coatings. Sputtering pulsed modes provided more energetic deposition conditions, which contributed to achieve harder coatings. Hydrogen is a key parameter for microstructural control, as it promotes clustering effects in the carbon structure and may destabilize C-C $sp^3$ bonding. DLC coatings microstructure is very sensitive to deposition temperature because it induces graphitization effects. Substrate bias is directly linked to the coating´s intrinsic stress and density. The essential role of $sp^3$ to enhance mechanical properties has been simulated with Molecular Dynamics in order to understand the underlying mechanisms that occur during nanoindentation. For higher $sp^3$ content, plasticity is highly constrained under the tip and only atomic rearrangement is observed, while for lower $sp^3$ content, plasticity extends beyond the highly strained area under the tip, leading to lower hardness and modulus.

- Cr-doped DLC coatings were co-deposited using HiPIMS technique under highly energetic conditions. Very high current densities (up to 4 $A/cm^2$) were obtained for low working frequencies (down to 15 Hz) on the Cr target. These singular process conditions could not be reproduced when doping DLC either at higher frequencies with Cr, or in all the frequency range with other metals such as Ti and W. When doping the carbon structure at low HiPIMS current densities, the metal dopant addition usually breaks up the diamond-like character by destabilizing C-C $sp^3$ bonding and promoting the formation of carbides. However, at high HiPIMS current densities and low Cr contents, it is possible to preserve the C-C $sp^3$ bonding structure with reduced stress, which produces doped DLC coatings with enhanced mechanical and tribological properties, particularly for high temperature conditions.

- The developments presented in the thesis have been technologically transferred to an industrial system (xPro4C) designed and manufactured by Nano4Energy and PVT companies.

Ongoing and **future research activities** include:

- To develop more energetic HiPIMS-based processes by using novel positive pulsing technology.

- To understand and take advantage of mechanisms such as the SYA effect reported during the codeposition of Cr-doped DLC coatings to produce denser and harder coatings.

- To analyze the microstructural changes produced by the mentioned deposition processes in further detail, with special focus on $sp^3$-$sp^2$ evolution.

- To combine experimental and computer simulations results to shed further light into the underlying mechanisms that govern the deformation behavior of DLC coatings, particularly at high temperatures, and to understand how these mechanisms affect the material properties measured experimentally using advanced micro and nanomechanical testing methods.

- To use the newly developed DLC coatings with optimized mechanical properties in tribological applications of industrial relevance under different lubrication modes and working conditions.

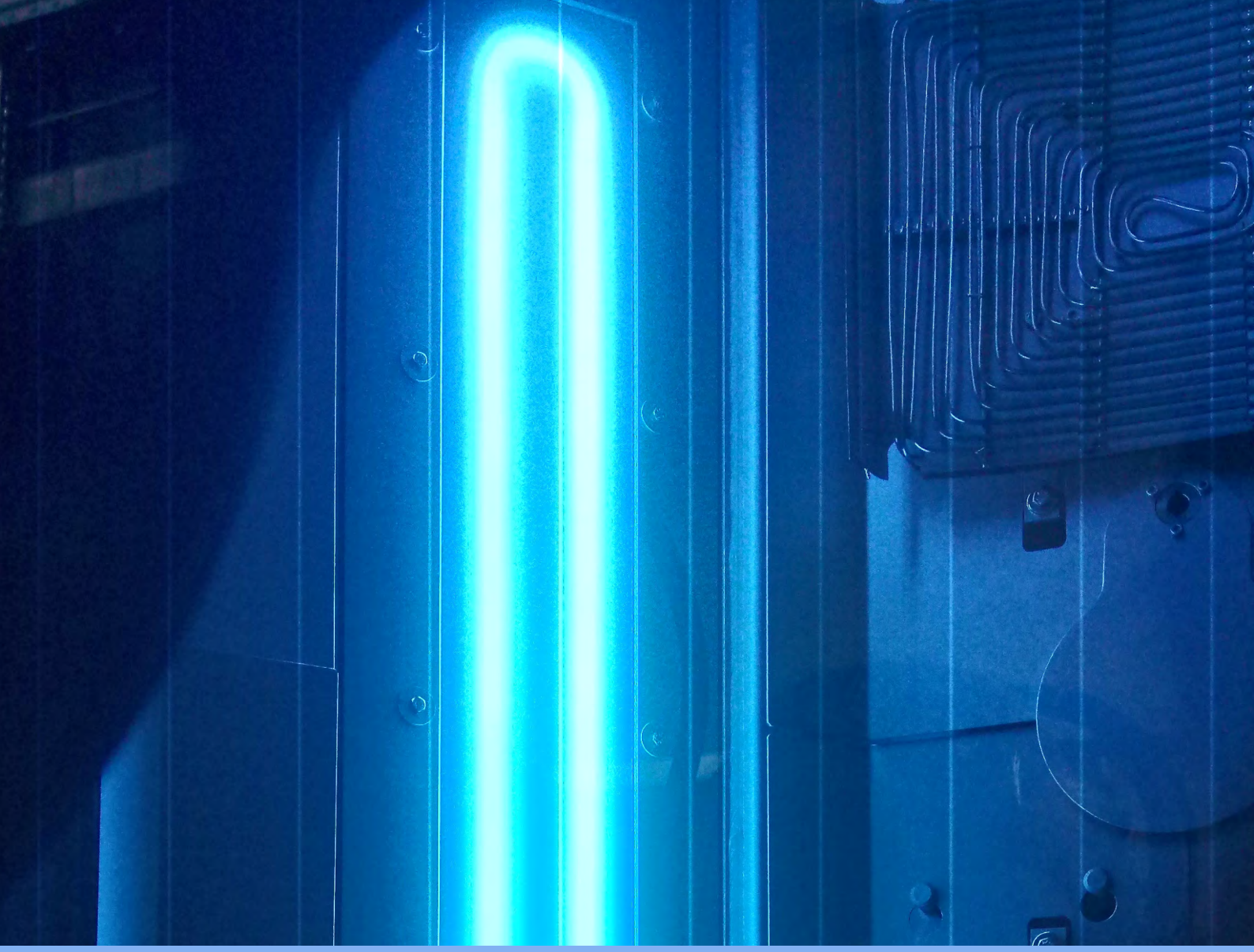

*"Whether we fall by ambition, blood, or lust, like diamonds we are cut with our own dust." John Webster*

# *Appendix*

## Industrial deposition of hard DLC coatings by HiPIMS and positive pulsed technology: from laboratory to an industrial-scale system (xPro4C)

The demand of highly sophisticated coatings for special tooling application is increasing rapidly. The most prominent example are DLC coatings [1-4]. Due to the emerging importance of such coatings in many tribological fields, the market for industrial systems is also growing very fast. In order to fulfil the future's demand in this field, efficient and reliable equipments are required.

This appendix aims to describe the industrial system designed and manufactured by Nano4Energy SL and PVT GmbH, incorporating different technological aspects that guarantee the production of high-end quality coatings. Main aspects include: 1) the engineering of the substrate/coating interface to improve the adhesion of hard coatings, 2) the study of the plasma distribution in the vacuum chamber to provide more energetic deposition conditions with the application of positive pulses, 3) tailoring the ion energies of the species with positive pulsing and 4) the hydrogen control with remote plasma gas analysis to guarantee the synthesis of hard and "hydrogen-free" amorphous carbon films.

## • Industrial system (xPro4C)

The experimental setup designed for DLC coatings' deposition at laboratory scale has been transferred to the industrial system xPro4C designed by PVT GmbH.


**Figure 1.** *General view of the xPro4C system manufactured by PVT GmbH for the deposition of DLC coatings*

The system integrates in a vacuum chamber of 0,51 $m^3$ (680 x 650 x 1150mm) four cathodes designed with adjustable magnetic field configurations. The plasma volume is 350 × 650 mm (Ø × H).

a) b)

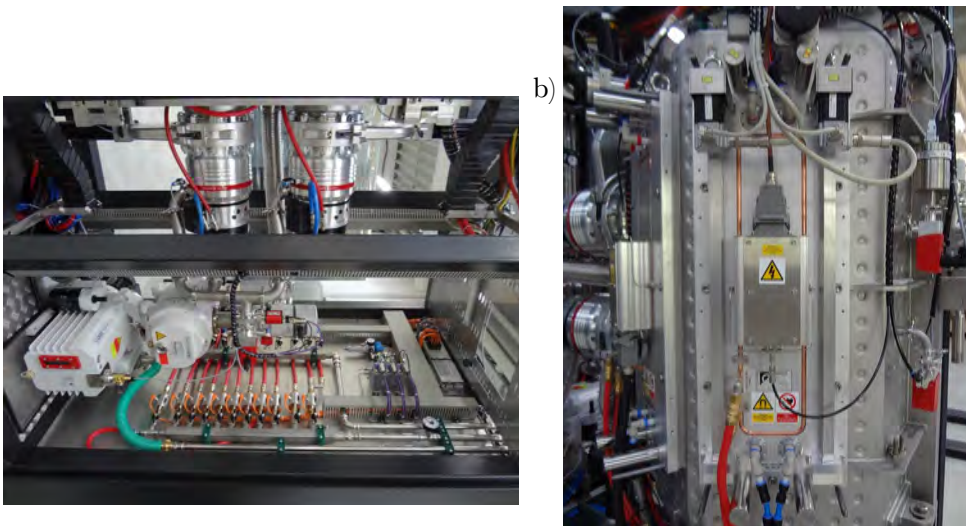

**Figure 2.** *a) General picture of pumping system used in xPro4C. b) External view of Gencoa's rectangular magnetrons with VT-ER technology.*

The chamber is evacuated by two turbomolecular pumps and two double stage rotary vane pumps (Fig. 2a). The four cathodes are incorporated in equidistance. For DLC coatings deposition, two of the cathodes are operated as unbalanced magnetrons (UBM) carrying graphite targets. The third cathode is used for depositing a WC interlayer with a balanced magnetron configuration carrying a binder-free WC target. The fourth cathode is operated in HiPIMS mode carrying a Cr target with a balanced magnetic field configuration. An schematic cross-sectional view of the chamber is presented in Fig. 3a.

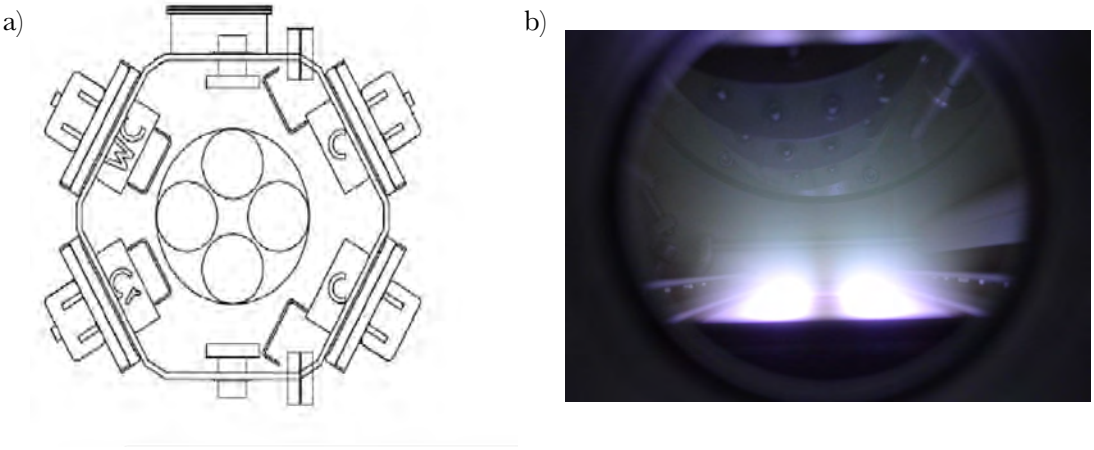


**Figure 3.** *(a) Schematic representation of the xPro4C chamber. (b) Top-view image of the carbon plasma discharge during HiPIMS deposition.*

## • Magnetic field configuration for increased ion assistance during deposition

For the deposition of hard DLC coatings, a tailored ion bombardment needs to be arranged in order to: 1) perform an efficient metal etching with HiPIMS, 2) take advantage of the higher energy induced by the incorporation of positive pulsing and 3) promote the generation of $sp^3$ hybridized carbon by densification-subplantation effects. In addition, uniform coating of three-dimensional parts with small distances between parts requires a strong plasma distribution to improve the coating coverage on all surfaces.

In a magnetron, the shape of the magnetic field depends on the strength and position of the corresponding magnets. There are two main magnetic field modes: balanced mode (BM) and unbalanced mode (UBM). For magnetrons where the magnets strength is the same, the magnetic field configuration is balanced (Fig. 4a). In the case when either the central magnet or the outer magnets are stronger than the others, magnetic configuration is unbalanced. Electrons follow magnetic field lines, so in the case when the central magnet is stronger than the outer magnets (Fig. 4b, Type I), electrons get lost from the plasma radially. Usually, this magnetic configuration is not of interest because the plasma confinement is very limited and there is no improvement as compared to the balanced configuration. However, when the outer magnets are stronger than the central magnet, electrons are redirected towards the substrate, contributing to an enhanced ionization near the substrate area (Fig. 4c, Type II). In most industrial deposition conditions, as well as for the work in this thesis, planar magnetron cathodes are operated in unbalanced magnetic field conditions (Type II) in order to increase the ion bombardment over the growing film.

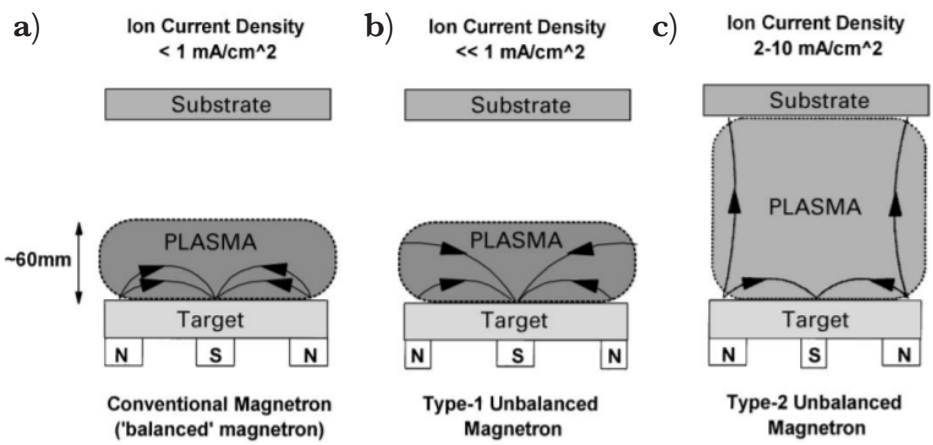


**Figure 4.** *a) Magnetic field lines for balanced configuration. b) Magnetic field lines for unbalanced configuration (Type 1) c) Magnetic field lines for unbalanced configuration (Type 2) used in most industrial magnetrons [5]*

Industrial systems are usually composed of several magnetrons working simultaneously during a process. In a multiple magnetron system, the magnetic arrays can be configured with either identical (mirrored) or opposite magnetic polarities (closed field), as shown in Fig. 5. Closed-field unbalanced magnetron configurations (CFUBM) are used in most industrial sputtering systems because of increasing ion bombardment over the substrate and higher deposition rates [5]. However, when using a fixed configuration, the ion to atom ratio can be varied only over a limited range.

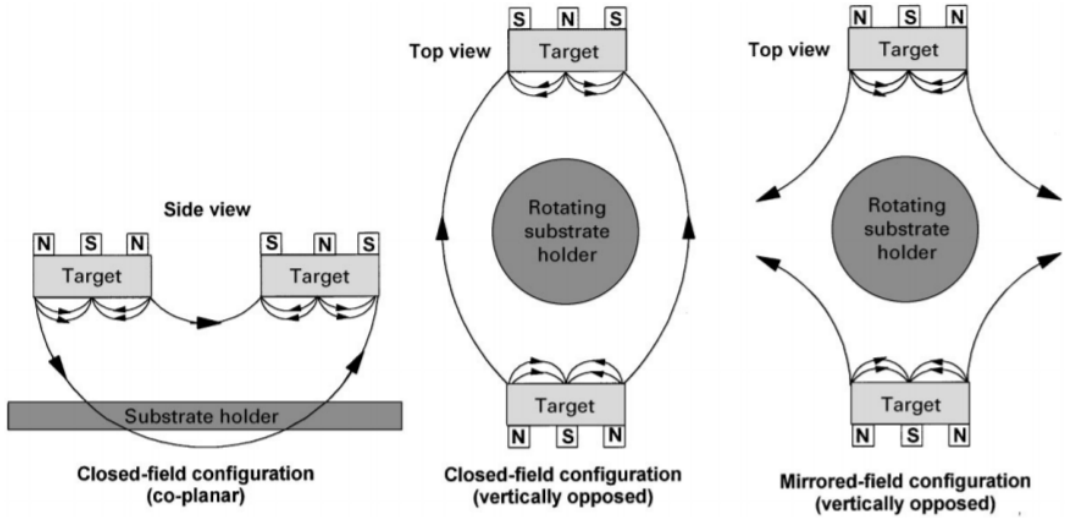


**Figure 5.** *Schematic representation of different plasma confinement strategies used with unbalanced magnetrons [5]*

For many industrial applications, it is of great interest to achieve flexible operating conditions in order to set different processes and work with different materials. More advanced adaptive magnetic field configuration (such as the VT-ER by Gencoa) can be used. In this technology, by rotating some magnetic elements on the external side of a flange mounted cathode, it is possible to move the relative position of the inner and outer set of magnets, thus controlling in-situ the degree of balance/unbalance at any stage of the deposition process.

Adjustable magnetic arrangement allows controlling the ion bombardment over the substrate and potentiate the optimization process carried out in this thesis. As an example of some of the available magnetic configurations, Fig. 6 illustrates: a) closed-field unbalanced configuration with plasma driven through substrate for the deposition of ta-C coatings and b) more balanced configuration with plasma exclusion zone to reduce bombardment over samples for the deposition of DLC coatings on temperature-sensitive substrates such as plastics.

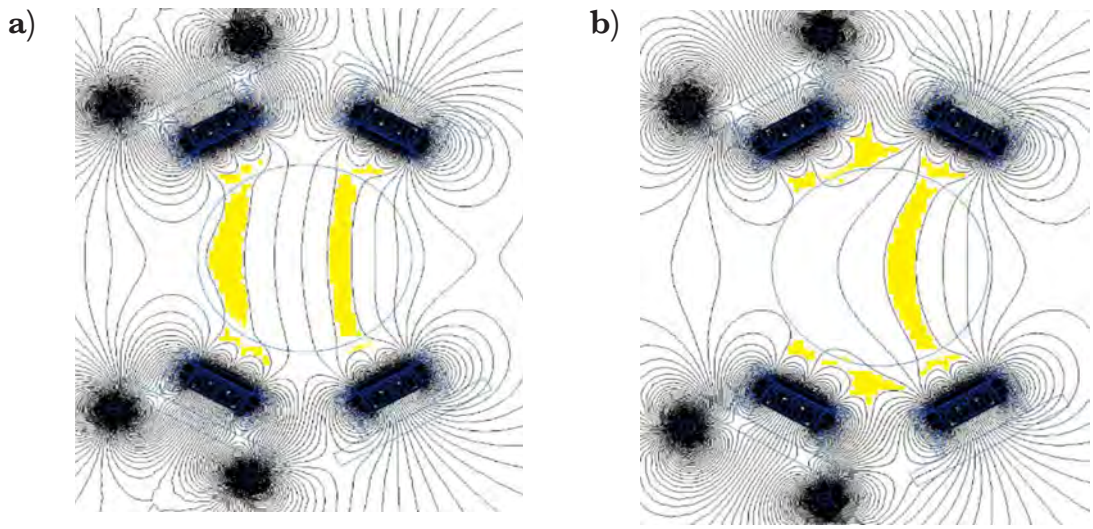


**Figure 6**. *a) Magnetic field lines in plasma-driven to substrate configuration. b) Magnetic field configuration to prevent excessive bombardment over samples*

## • Industrial application of HiPIMS with positive pulse technology (HiPIMS V+)

As explained in Chapter 4, the incorporation of positive pulses at the end of the regular HiPIMS negative pulse brings about great benefits to the DLC coatings deposition process. It has been demonstrated how the carbon and argon ion energies are directly related with the amplitude of the positive pulse. Therefore, it is possible to tailor the ion bombardment during deposition by adjusting the pulse parameters, shown in Fig. 7. HiPIMS power supplies by HiP-V have been developed to tune positive pulse's parameters for coatings' optimization.

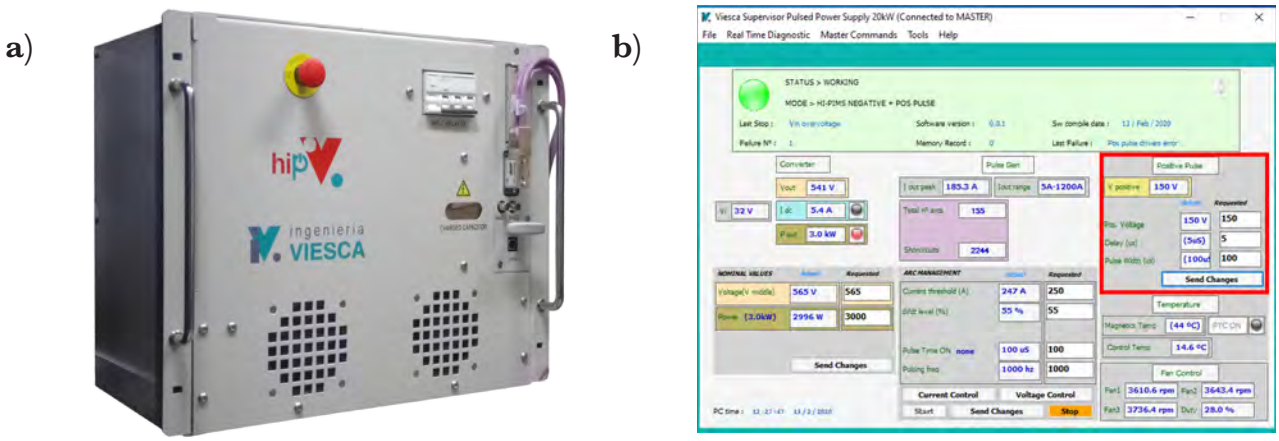


**Figure 7**. *a) HiP-V power supply used for HiPIMS processes in this thesis. b) New features(red tab) incorporated to positive pulsing technology in HiP-V power supplies*

New generation of HiP-V power supplies, like the one shown in Figure 7a, provide adjustable control in:

- Amplitude: +0 to +500V
- Time of delay
- Time of pulse: 200 µs

The increase in positive pulse amplitude allows reaching higher energetic ions, while increased time of pulses allows enhancing the efficiency for collecting energetic ions in industrial applications. This development also opens the possibility to apply hard coatings in applications where substrate bias is restricted, such as the deposition of protective coatings on insulating substrates.

## • Remote plasma analysis in industrial processes

In industrial applications, there is a need to introduce further process monitoring in order to control parameters such as hydrogen pick-up (discussed in Chapter 5) and to ensure low levels of impurities in advanced vacuum systems for adhesion enhancement (Chapter 3). These issues can be solved by the implementation of in-situ diagnostic techniques such as the Optix by Gencoa Ltd.

This device generates a remote plasma with the gas present inside the chamber and analyses the light emitted from the plasma with the method of OES, identifying the different reactant species.

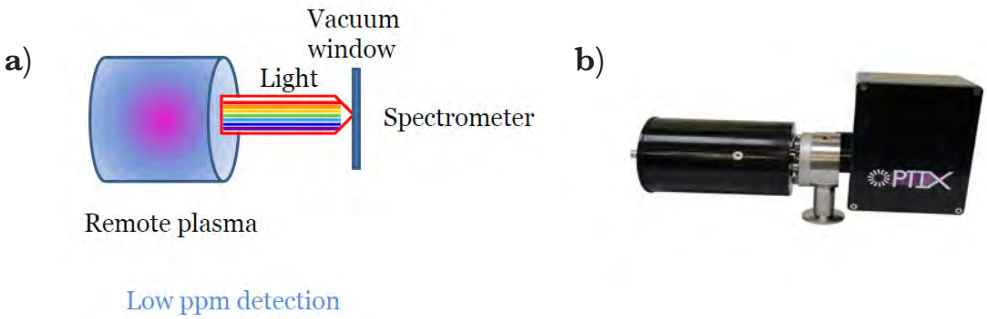


**Figure 8.** *a) Schematic principle of operation of Optix. b) Image of Optix by Gencoa Ltd*

Operating in the range of $10^{-2}$ to $10^{-6}$ mbar, Optix monitors the evolution of relevant species during DLC coatings deposition: $H^+$, $OH^-$, $O_2$, $N_2$, within the spectral range from 200 nm to 900 nm. The quantification of these species has been used as an indicator to monitor leakages (as shown in Fig. 9), to control the hydrogen pick-up during carbon deposition and to evaluate other potential factors that affect the reactive sputtering processes, such as the amount and energy of reactant ionic species.

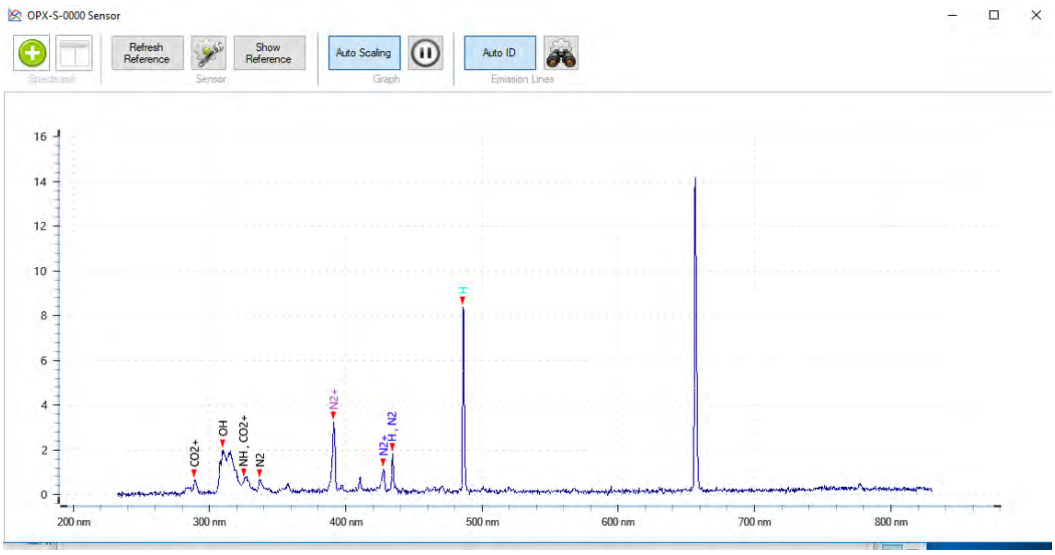


**Figure 9.** *a) Optical emission spectra obtained with Optix during pumping process. By monitoring the intensity of $N_2$+ emission line at 390 nm, it is possible to check the existence of a leakage in the system*

## • DLC coatings deposited in xPro4C industrial system

The properties of the DLC coatings deposited in xPro4C system are summarized in the following table:

**Table 1.** *Mechanical and tribological properties of DLC coatings deposited in xPro4C industrial system*

| Sample | Hardness (GPa) | Reduced elastic modulus (GPa) | COF | Max service Temperature (ºC) |
|---|---|---|---|---|
| ta-C | 37.4 ± 3.2 | 265 ± 24 | 0.12 | 450 |
| a-C:Cr | 31.2 ± 2.8 | 243 ± 18 | 0.10 | 450 |
| WC:C | 18.8 ± 2.4 | 175 ± 9 | 0.11 | 400 |

The xPro4C system allows depositing DLC coatings of several families: hydrogen-free amorphous carbon coatings (ta-C) by HiPIMS, metal-doped DLC with Cr (a-C:Cr) and W (WC:C) by HiPIMS. The industrial system incorporates updated technical developments which allowed enhancing the mechanical and tribological properties of DLC coatings. The hardness of a-C coatings improved from 29.1 GPa obtained in this thesis to current hardness values of 37.4 GPa deposited in an industrial system. Also, a-C:Cr and WC:C coatings have increased their tribomechanical performance between 10-20%.

These properties suit perfectly applications like threading or milling very abrasive materials. Machining carbon-fiber reinforced composites, graphitic materials and non-ferrous alloys, especially aluminum alloys with high Si contents are a big challenge in tools market because such "sticky" materials undergo the formation of built-up edges (BUE) during machining operations. When this happens the outcome is likely to be a poor surface finish. In order to overcome these issues, the deposition of hard and smooth DLC coatings must be realized in advanced microtools with different shapes and size, as shown in Fig. 10.

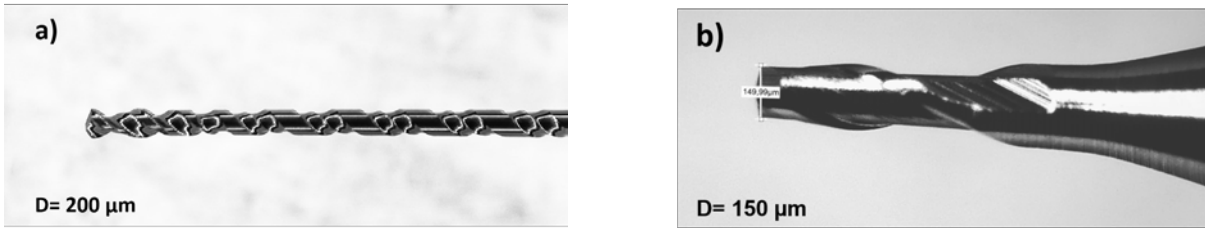


**Figure 10.** *DLC coatings deposited on tools for (a) micromachining aluminum alloys and (b) micromachining titanium alloys (Ti6Al4V)*

Besides, the xPro4C system fulfills the industrial requirement to coat large-area components with good adhesion and uniform coating thickness all over the material's surface area.

## • Conclusions

This appendix illustrates how technological aspects developed in this thesis can be transferred to an industrial DLC system successfully. The results obtained with xPro4C by PVT GmbH demonstrate clearly that superior hard DLC coatings, with low friction coefficient, high wear resistance and smooth surface finish can be manufactured in multitarget industrial batch type machines.

---

References

[1] Tribology of Diamond-Like Carbon films: Fundamentals and Applications, Springer, N. York, 2007

[2] Tetrahedrally bonded amorphous carbon films I: basics, structure and preparation, Springer series in Material science 263, 2018

[3] K. Bewilogua, D. Hofmann, Surface and Coatings Technology, 242 (2014) 214-224

[4] WD Münz et al, Surface and Coatings Technology, 387 (2020) 125485

[5] PJ Kelly, RD Arnell, Vacuum 56, Issue 3 (2000) 151-226

# *Appended papers*

## Thesis' publications:

1. Adhesion enhancement of DLC hard coatings by HiPIMS metal ion etching pretreatment.
**Surface and Coatings Technology 349 (2018) 787-796**

*J.A. Santiago, I. Fernandez-Martinez, A. Wennberg, J.M. Molina-Aldareguia, M. Castillo-Rodriguez, T.C. Rojas, J.C. Sánchez-López, M.U. González, J.M. Garcías-Martín, H. Li, V. Bellido-González, M.A. Monclús, R. González-Arrabal*

2. The influence of positive pulses on HiPIMS deposition of hard DLC coatings **Surface and Coatings Technology 358 (2019) 43-49**

*J.A. Santiago, I. Fernandez-Martinez, T. Kozak, J. Capek, A. Wennbegr, J.M. Molina-Aldareguia, V. Bellido-González, R. González-Arrabal, M.A. Monclús*

3. Tribomechanical properties of hard Cr-doped DLC coatings deposited by low-frequency HiPIMS.
**Surface and Coatings Technology 382 (2020) 124899**

*J.A. Santiago, I. Fernandez-Martinez, A. Wennberg, J.M. Molina-Aldareguia, T.C. Rojas, J.C. Sánchez-López, V. Bellido-González, M.A. Monclús, R. González-Arrabal*

## Other publications:

4. A comparative study in the tribological behaviour of DLC coatings deposited by HiPIMS technology with positive pulses. **Metals 10 (2020) 174**

*J.A. García, J. Rivero, E. Barba, I. Fernández-Martínez, J.A. Santiago, J.F. Palacio, G.G. Fuente, R.J. Rodríguez*

5. Individual and combined effects of introducing DLC coating and textured surfaces in lubricated contacts.
**Tribology International 151 (2020) 106440**

*I Bellon-Vallinot, E. Guerra-Ochoa, J. Echávarri, E. Chacón, I. Fernández-Martínez, J.A. Santiago*

6. Nanoindentation of Amorphous Carbon: a combined experimental and simulation approach

*F.J. Valencia, J.A. Santiago, R.I. González, R. González-Arrabal, C. Ruestes, M. Perez-Diaz, J.M. Molina-Aldareguia, P. Diaz-Nuñez, F. Muñoz, M. Kiwi, J.M. Perlado, E. Bringa*

## Congresses:

1. Temperature dependence of the tribomechanical properties of DLC coatings deposited by magnetron sputtering (Poster presentation)

**Plasma Surface Engineering (PSE 2016), Garmisch, Germany**

*J.A. Santiago, I. Fernandez, A. Wennberg, F. Papa, V. Bellido, A. Rivera, J. Molina, R. Gonzalez Arrabal, MA. Monclus*

2. Adhesion enhancement of DLC hard coatings by HiPIMS metal ion etching pretreatment and its tribological properties (Oral presentation)

**European Congress on NanoFilms (ECNF 2016), Bilbao, Spain**

*J.A. Santiago, I. Fernandez, A. Wennberg, F. Papa, V. Bellido, J.M. García Martín, D. Fuster, M. Castillo, J. Molina, MA. Monclus, R. Gonzalez Arrabal*

3. Adhesion enhancement of DLC hard coatings by HiPIMS metal ion etching pretreatment (Oral presentation)

**HiPIMS 2017, Braunschweig, Germany**

*J.A. Santiago, I. Fernandez, A. Wennberg, F. Papa, V. Bellido, J.M. García Martín, D. Fuster, M. Castillo, J. Molina, MA. Monclus, R. Gonzalez-Arrabal*

4. Hard Cr-doped DLC coatings deposited by low-frequency HiPIMS with enhanced tribomechanical behavior at high temperature (Oral presentation)

**Plasma Surface Engineering (PSE 2018), Garmisch, Germany**

*J.A. Santiago, I. Fernández-Martínez, A. Wennberg, J.M. Molina-Aldareguia, M.A. Monclús , V. Bellido-González, R. González-Arrabal, T.C. Rojas, J.C. Sánchez-López*

5. Hard Cr-doped DLC coatings deposited by low-frequency HiPIMS with enhanced tribomechanical behavior at high temperature (Oral presentation)

**International Conference on Metallurgical Coatings and Thin Films (ICMCTF 2019). San Diego, USA**

*J.A. Santiago, I. Fernández-Martínez , A. Wennberg , J.M. Molina-Aldareguia, M.A. Monclús , V. Bellido-González, R. González-Arrabal , T.C. Rojas, J.C. Sánchez-López*

6. Tribomechanical properties of doped DLC coatings deposited by HiPIMS

**Plasma Surface Engineering (PSE 2020), Erfurt, Germany**

*J.A. Santiago, I. Fernández-Martínez , A. Wennberg , J.M. Molina-Aldareguia, M.A. Monclús , V. Bellido-González, R. González-Arrabal , T.C. Rojas, J.C. Sánchez-López*

# Novel HiPIMS *processes for* DLC coatings

*José Antonio Santiago Varela*